Insights into the temporal evolution of magma plumbing systems from compositional zoning in clinopyroxene crystals: a case study from the Agnano-Monte Spina Plinian eruption (Campi Flegrei, Italy)

Pelullo C.[1,3], Chakraborty S.[2], Cambeses A.[2], Dohmen R.[2], Arienzo I.[3], D'Antonio M.[1], Pappalardo L.[3], Petrosino P.[1]

[1]*Università di Napoli Federico II, Dipartimento di Scienze della Terra, dell'Ambiente e delle Risorse, Cupa Nuova Cintia, 21 - 80126 – Napoli, Italy*

[2]*Institut für Geologie, Mineralogie und Geophysik, Ruhr Universität, Universitätsstraße 150 - 44801, Bochum, Germany*

[3]*Istituto Nazionale di Geofisica e Vulcanologia, Sezione di Napoli Osservatorio Vesuviano, Via Diocleziano, 328 - 80124, Napoli, Italy*

* Corresponding author: carlo.pelullo@unina.it

Abstract

The complex sequential compositional zoning of clinopyroxene crystals erupted < 5ka during the Agnano-Monte Spina (A-MS) eruption, which is considered to be the reference event for a future large-scale explosive eruption at Campi Flegrei caldera (Italy), has been characterized in detail. Concentration profiles (20–800 μm long, spacing 2.5–10μm) of major (Si, Ti, Al, Fe, Mg and Ca) and minor (Mn, Na, Ni and Cr) elements were measured along different directions in the clinopyroxene crystals. The zoning patterns of Fe–Mg and selected elements (e.g. Al, Ti) often consist of two or more compositional plateaus with both sharp and/or slightly diffuse boundaries between the plateaus. Each compositional population results from a growth stage in a distinct Magmatic Environment (ME), which is identified as a defined set of intensive thermodynamic variables (pressure, temperature, bulk composition and fugacity of fluids including oxygen). The large range of chemical compositions of clinopyroxenes reveals the existence of at least four MEs that are characterized by different compositional populations; two of these are dominant. The variation in zoning pattern from one plateau composition to another fingerprints the transfer of the crystal from one ME to another. In combination with Sr isotopic data and thermobarometric estimates, our systematic characterization of clinopyroxene zoning patterns suggests recharge by deep mafic magmas (ME0: Mg#=92–85) of an evolved shallow reservoir (ME2: Mg#=78–70). Such a process also led to the formation of a compositionally intermediate environment (ME1: Mg#=84–80), that is detected in the clinopyroxene zoning pattern.

A new method has been developed in this work to evaluate the effective diffusive modifications that affect the concentration profiles of zoned crystals. The application of different diffusion modeling methods indicates that deep and shallow reservoirs beneath the Campi Flegrei caldera were connected to each other over several tens of years until the amount of mafic recharge increased during the last 10–15 years before the A-MS eruption. This study highlights the complex relationships between events of magma recharge and the onset of eruption. Our results provide a

contribution to the knowledge of timescales of magmatic processes that have recently occurred beneath the Campi Flegrei caldera, which is useful for risk assessment.

Key words

Clinopyroxene zoning patterns – Plumbing system – Campi Flegrei caldera – Magma mixing – Diffusion chronometry

1 Introduction

Volcanic eruptions are triggered by magmatic processes that occur in subvolcanic plumbing systems and so a better understanding of magma evolution rates and processes has implications for volcanic hazard forecasting (Blundy and Cashman, 2008; Saunders et al., 2012; Kahl et al., 2013; Cashman and Giordano, 2014; Petrone et al., 2016; Sparks and Cashman, 2017; Cooper, 2019). High-precision, high spatial resolution analysis of major and trace elements of chemically zoned minerals represents a powerful tool for investigating nature and rates of the magma chamber processes that preceded explosive eruptions of variable energy. Since mineral compositions in a magma depend on crystallization conditions, crystals preserve evidence of parameters (e.g. pressure, temperature, oxygen fugacity and volatile content) that characterize the environments where they were formed.

Compositional data on various portions of chemically heterogeneous minerals have provided information both on pre-eruptive processes such as magma ascent, recharge of a reservoir, differentiation and mingling/mixing as well as their timescales (e.g. Zellmer et al., 1999, 2003; Costa and Chakraborty, 2004; Humphreys et al., 2006; Turner and Costa, 2007; Alves et al., 2009; Kahl et al., 2011, 2013, 2015, 2017; Chamberlain et al., 2014; Ubide et al., 2015, 2019; Ubide and Kamber, 2018; Astbury et al., 2018, Cooper, 2019).

In spite of this large body of work, diffusion modeling of volcanic clinopyroxene crystals using compositional profiles measured through microanalysis and recently obtained experimental diffusion coefficient data (e.g. Müller et al., 2013) are rare, exceptions being the recent study of Mangler et al. (2020) or that of Chowdhury and Chakraborty (2019) on metamorphic clinopyroxenes. One earlier study used BSE contrast imaging and older diffusion data to obtain timescales of magmatic processes that preceded the 1944 AD eruption of the nearby Vesuvius volcanic complex (Morgan et al., 2004).

In this paper we develop a tool to use compositional zoning in clinopyroxene crystals to infer the nature and timescales of magmatic processes in volcanic plumbing systems. To develop the tool, we use detailed chemical characterization of clinopyroxene crystals from the products of Agnano-Monte Spina (A-MS), a Plinian eruption that occurred at Campi Flegrei caldera at 2604–2461 BCE (Smith et al., 2011). For a dormant, though active and restless volcano, an estimate of the time required for magma to become eruptible, either by coalescence of separate shallow batches or by deeper magma recharge, is of paramount importance. The expected resumption of explosive activity and the high population density in the region makes the Campi Flegrei caldera one of the most hazardous and vulnerable volcanic areas on Earth (Orsi et al., 2004, 2009; Bevilacqua et al., 2015; Mastrolorenzo et al., 2017). These aspects, combined with the fact that a variety of clinopyroxene compositional patterns are found in the rocks, make the A-MS eruption an ideal target for developing the tool. Moreover, there have already been several attempts at assessing timescales of pre-eruptive processes for Campi Flegrei volcanic activity using different approaches. Estimates of timescales of magma differentiation, transfer, recharge, accumulation and mixing have been obtained through isotope analyses (e.g. Arienzo et al., 2011), zircon geochronology (e.g. Gebauer et al., 2014; Wu et al., 2015), diffusion chronometry (e.g. Iovine et al., 2017a) and experimental petrology (e.g. Perugini et al., 2015). Timescale information based on textural analysis (e.g. Crystal Size Distribution – CSD; Piochi et al., 2005; Mastrolorenzo and Pappalardo, 2006; Pappalardo and Mastrolorenzo, 2012; Arzilli et al., 2016), historical, archaeological, geological and long-term geodetic record (e.g. Di Vito et al., 2016 and reference therein), numerical simulations (e.g. Montagna et al., 2015) and crystals growth rates (e.g. Astbury et al., 2018) has also been acquired. All of these provide a framework within which to evaluate the results of the current study.

We have carried out quantitative analyses along core to rim transects of clinopyroxene crystals belonging to different eruptive units of the A-MS deposits. The zoning patterns in the crystals are characterized by zones with constant compositions that have been interpreted to represent changes in magmatic environments in which the crystals resided (Kahl et al., 2013, 2015, 2017; Solaro et al.,

2020). After systematizing the connectivity between different magmatic environments, we have attempted to reconstruct the pre-eruptive processes, and then applied the newly developed diffusion modeling tools to constrain the timescales of these processes.

2 Volcanological and petrological background

2.1 The Campi Flegrei caldera

The volcanic history of the Campi Flegrei caldera (CFc) has been extensively investigated in the past decades (e.g. Orsi et al., 1996; Di Vito et al., 1999, 2016; Isaia et al., 2004, 2009; Scarpati et al., 2013). Continental Campi Flegrei together with the islands of Ischia and Procida, constitute the Phlegraean Volcanic District (PVD; Fig. 1a-b; Orsi et al., 1996). The PVD formed in response to the Pliocene-Quaternary extensional processes that generated the Campania Plain graben, along the Tyrrhenian margin of the Apennine thrust belt (Fig. 1a; Acocella and Funiciello, 2006). The NW–SE normal and NE–SW normal to strike-slip transfer fault systems separated the graben into blocks and allowed magmas to rise to the surface (Acocella et al., 1999; Brocchini et al., 2001; Piochi et al., 2005; Acocella and Funiciello, 2006 and reference therein). Except for Procida, whose activity ended *c.* 22 ka (Morabito et al., 2014), Ischia island and CFc are still active and pose a high volcanic hazard.

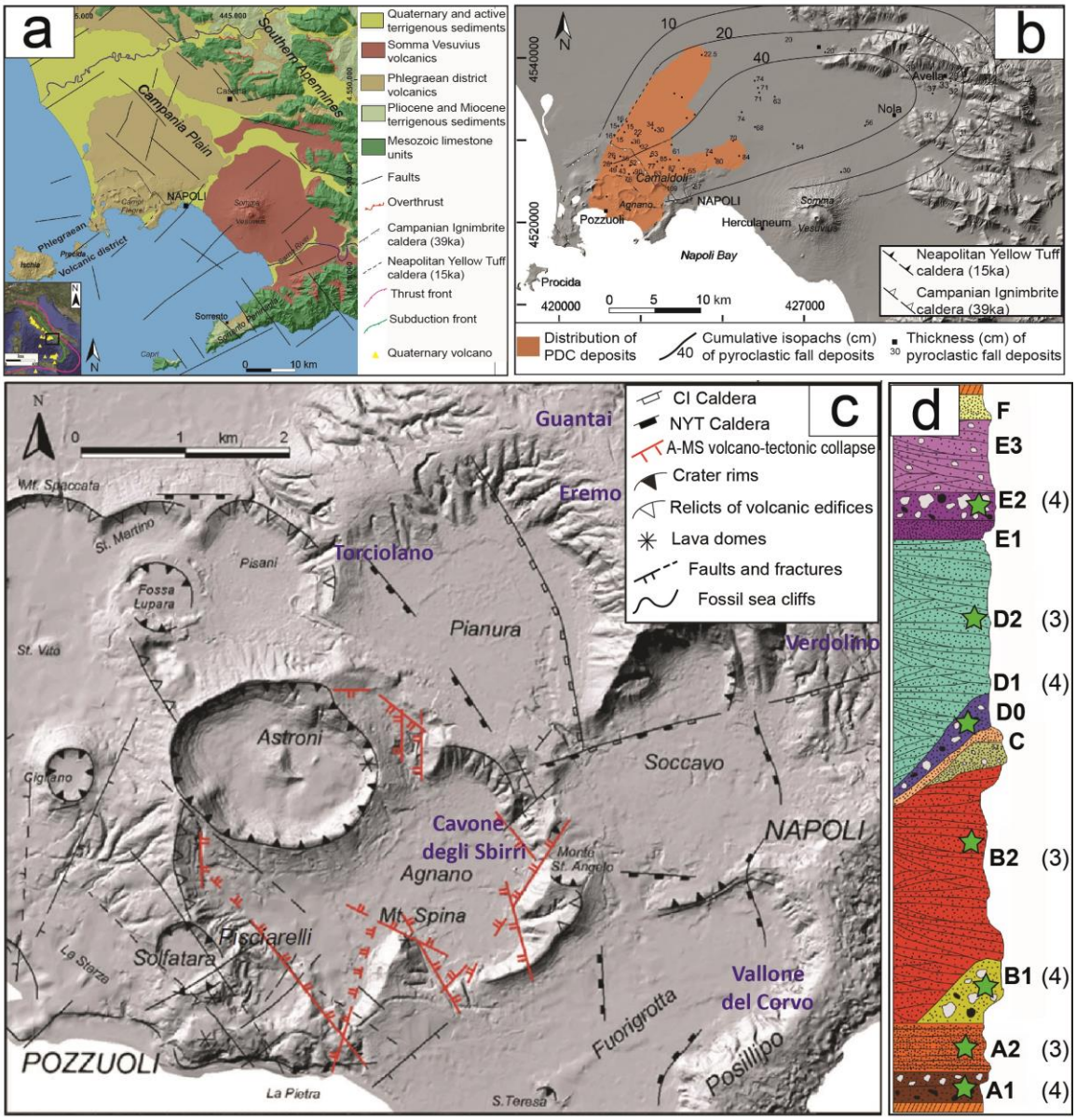

Fig. 1 a) Geological and structural sketch map of the Southern Campania Plain (modified after Orsi et al., 2003). b) Areal distribution of the A-MS volcanic deposits (redrawn after de Vita et al., 1999. c) Detail of the Agnano-San Vito area (modified after Iovine et al., 2017a) d) Schematic stratigraphic column of the A-MS erupted products, subdivided into various members (modified after Iovine et al., 2017a).; in brackets we reported the number of samples collected from each sub-member.

The volcanic activity at Campi Flegrei started at least *c.* 80 ka (Scarpati et al., 2013). The CFc is the result of multiple collapses that occurred during two big-size explosive eruptions: the Campanian Ignimbrite dated to *c.* 40 ka (Gebauer et al., 2014; Giaccio et al., 2017 and references therein) and the Neapolitan Yellow Tuff (NYT) dated to *c.* 15 ka (Deino et al., 2004). Volcanic activity has been

dominantly explosive through time, with several minor volcano-tectonic collapse episodes, hence volcanic products of the CFc are mostly pyroclastic rocks and subordinate lava flows and domes. During the last 15 ka, the caldera has been the site of intense volcanism and deformation, characterized by ~ 70 eruptions grouped into three epochs of activity: epoch 1 *c*. 15–10.6 ka; epoch 2 *c*. 9.6–9.1 ka; and epoch 3 *c*. 5.5–3.5 ka (Di Vito et al., 1999; Smith et al., 2011). The last event, possibly marking the beginning of a new epoch (e.g. Bevilacqua et al., 2017) occurred in 1538 AD (Monte Nuovo eruption; Piochi et al., 2005; Guidoboni and Ciuccarelli, 2011; Di Vito et al., 2016; Liedl et al., 2019). During the past *c.* 5 ka, 28 low-to medium-magnitude eruptions occurred from vents mostly located in the NE part of the NYT caldera in the 12 km^2 Agnano-San Vito area (Smith et al., 2011; Bevilacqua et al., 2017; Fig. 1c). This area includes the Astroni, Solfatara, and Agnano craters, and is considered as one of the sites of highest probability of future resumption of volcanic activity (Orsi et al., 2004; Selva et al., 2012; Bevilacqua et al., 2016, 2017). This portion of the NYT caldera has been subjected to extensional tectonics since at least *c*. 5 ka (Capuano et al., 2013) through NW–SE- and NE–SW-trending regional faults, favoring the ascent of trachytic and latitic magmas which fed the eruptions, and it is currently affected by voluminous hydrothermal emissions (Chiodini et al. 2015 and references therein). The intense fumarolic activity and the unrest episodes that occurred in recent decades (Del Gaudio et al., 2010) testify to the persistent activity of the CFc system. The presence of 350,000 inhabitants in the central part of the caldera raises the risk level to very high (Selva et al., 2012).

The Campi Flegrei volcanic rocks range in composition from potassic shoshonite to trachyte and phonolite and appear to be the products of magmas originated in a mantle modified by fluids/melts from the subducting Ionian slab (e.g. Tonarini et al., 2004, D'Antonio et al., 2007; Mazzeo et al., 2014). They exhibit a wide range of $^{87}Sr/^{86}Sr$ (07086–0.7068), but limited ranges of $^{143}Nd/^{144}Nd$ (0.51266–0.51240) and Pb-isotope ratios (e.g. $^{206}Pb/^{204}Pb$: 19.25–18.85; D'Antonio et al., 2007; Pappalardo et al., 2002). The geochemical variability of Campi Flegrei magmas results from a variety of petrogenetic processes (e.g. partial melting of the mantle source, fractional crystallization,

crustal assimilation, magma mixing; D'Antonio et al. 1999, 2007; Pappalardo et al., 1999, 2002; 2008; Fedele et al. 2008; Mangiacapra et al., 2008; Arienzo et al. 2009, 2015, 2016; D'Antonio, 2011; Di Renzo et al., 2011; Melluso et al., 2012; Pappalardo and Mastrolorenzo, 2012; Belkin et al., 2016; Forni et al., 2018; Pappalardo and Buono, 2021). Minor, poorly differentiated trachybasaltic and latitic magmas erupted at the end of the first epoch, along NE–SW trending regional tectonic structures (Orsi et al., 1996). Eruption of these magmas along the rim and differentiated magmas within the caldera testifies to the ascent of weakly differentiated, CO_2-rich magmas of deep provenance through regional faults (D'Antonio et al., 1999; Moretti et al., 2013; Arienzo et al., 2016) and to the occurrence of a shallow storage region beneath the caldera, within which the magmas evolve to trachyte and phonolite. Melt inclusion data indicate crystallization between ~ 9 and ~ 4 km (e.g., Marianelli et al., 2006; Mangiacapra et al. 2008; Arienzo et al. 2010, 2016). The trachyte and phonolite storage region is relatively shallow with respect to the reservoir from which the shoshonitic-latitic magmas rise (Pappalardo and Mastrolorenzo, 2012; Moretti et al., 2013; Fedi et al., 2018).

2.2 The Agnano-Monte Spina eruption

The A-MS eruption was the only high-magnitude event of the past *c.* 5 ka at CFc (Orsi et al. 2004, 2009) and it is considered the reference event for a future medium-size explosive eruption (Mele et al., 2015). The eruption was characterized by magmatic/phreatomagmatic activity (de Vita et al., 1999; Dellino et al., 2001) that led to the emplacement of alternating fallout and pyroclastic density current (PDC) deposits, distributed over an area of ~ 1000 km^2. The thick sequence of deposits was subdivided into various members and sub-members, named A through F from the base upwards (Fig. 1d; de Vita et al., 1999). The fallout deposits are dispersed towards the north-east. High particle concentration PDC were confined within the Agnano depression, while more dilute PDC overtopped the morphological boundary of the caldera and ran at least 20 km NE (Fig. 1b; de Vita et al., 1999). The thickness of the tephra varies from a maximum estimated value of ~ 70 m in the

Agnano plain, the inferred vent area for the eruption, to a few centimeters over a distance of ~ 50 km. Estimations based on distribution and thickness of A-MS products yield a volume of ejected magma of ~ 0.9 km^3 (dense rock equivalent; Orsi et al., 2009).

The A-MS juvenile fragments are potassic alkaline rocks, ranging in composition from trachyte to phonolite. De Vita et al. (1999) reported a general decreasing differentiation degree from bottom to top of the A-MS sequence. They also noticed that the total range of variation for several trace elements is large despite the limited variation of major oxide contents and found evidence for Sr-isotopic disequilibria among whole rocks and minerals. The authors concluded that the A-MS eruption was fed by two isotopically and chemically distinct trachytic and phonolitic magma batches that mixed during the eruption. Moreover, Arienzo et al. (2010), Moretti et al. (2019) and Romano et al. (2020) supported the mixing hypothesis of the previous authors and investigated the role of the H_2O, CO_2 volatile phases involved prior to/during the eruption, linking them to the magmatic components and to the eruption dynamics.

3 Samples and methods

The analyzed A-MS rocks are pumice fragments extracted from different deposits outcropping in the Agnano plain (Fig. 1c). Pumice fragments from the A-MS eruption are porphyritic, with phenocrysts of plagioclase and alkali–feldspar, clinopyroxene, phlogopite, apatite and Ti-magnetite in order of decreasing abundance (Fig. 1 in Supplementary Material 1). Feldspar, clinopyroxene and phlogopite phenocrysts occur as single crystals or sometimes as aggregates. The groundmass is glassy and contains rare microlites of clinopyroxene, K-feldspar, plagioclase and phlogopite.

In the present work, we sampled the A-MS sequence in the representative localities of Cavone degli Sbirri, Guantai, Torciolano, Vallone del Corvo, Verdolino and Eremo (Fig. 1c) within and nearby the Agnano plain. We collected 25 samples, which correspond to different sub-members (Fig. 1d). The samples are pumice fragments collected from both fall and PDC deposits of all localities and sub-members (Fig. 1d).

The selected pumice samples were gently crushed to lapilli-size grains through a jaw crusher. About 500 g of crushed sample was sieved using a stack of sieves with meshes ranging from 1ϕ to -1ϕ. From the sieved aliquots, clinopyroxene, K-feldspar, phlogopite phenocrysts and pumice glass fragments were hand-picked under a binocular microscope. These grains were loaded in sample holders with epoxy resin and suitably polished with decreasing grain-size diamond paste. The crystals were oriented in order to cut the crystals along the elongated axis, presumably the c-axis. The glass fragments and clinopyroxene crystals were carefully observed in reflected and transmitted light at optical microscope and in polished thin section under a binocular polarized light microscope before obtaining compositional data.

3.1 Analytical techniques

An overall chemical characterization of glass and clinopyroxene crystals (Supplementary Material 2) from all the aforementioned A-MS eruptive members was performed at DiSTAR - University of Napoli Federico II, by a JEOL-JSM 5310 electronic scanning microscope (SEM) equipped with an INCA X-Act detector using energy dispersive X-ray spectroscopy (EDS) microanalysis technique. Measurements were performed at a 15 kV primary beam voltage, 50–100 μA filament current, variable spot size and 50 s net acquisition time. The following standards were used for calibration: diopside (Mg), wollastonite (Ca), anorthoclase (Al, Si), albite (Na), rutile (Ti), almandine (Fe), Cr_2O_3 (Cr), rhodonite (Mn), orthoclase (K), apatite (P), fluorite (F) and sodium chloride (Cl). Relative analytical uncertainty is typically ~1% for major elements, ~3–5% for minor elements.

Detailed mineral composition (Supplementary Material 2) were obtained along transects of length varying from 20 μm to 800 μm on zoned clinopyroxene crystals. The data were collected at the HP-HT Laboratory of Experimental Volcanology and Geophysics of the Istituto Nazionale di Geofisica e Vulcanologia in Rome (Italy), using a Jeol-JXA8200 electron microprobe equipped with five wavelength dispersive spectrometers. This kind of specific analysis was performed on selected samples belonging to A1, B1 and D1 members, which are the main fallout deposits representative

229 of the entire compositional range of the A-MS deposits. Crystals in carbon-coated resin mounts
230 were analyzed under high vacuum conditions, using an accelerating voltage of 15 kV. Crystals were
231 traversed using spots with separation of 2.5, 3.5, 5, 7 and 10 μm and variable beam diameter of 2.5,
232 3.5 and 5 μm, both depending on the transect length. The electron beam current was set at 7.5 nA.
233 Elemental counting times were 10 s on the peak and 5 s on each of two background positions.
234 Corrections for inter-elemental effects were made using a ZAF (Z: atomic number; A: absorption;
235 F: fluorescence) routine. The range of standards for calibration was taken from Micro-Analysis
236 Consultants (MAC; http://www.macstandards.co.uk) and variable diffraction devices: albite (Si-
237 PET, Al-TAP, Na-TAP), forsterite (Mg-TAP), augite (Fe-LIF), apatite (Ca-PET), orthoclase (K-
238 PET), rutile (Ti-PET), and rhodonite (Mn-LIF). Smithsonian augite (Jarosewich et al., 1980) and
239 MAC augite were used as quality monitor standards and for the calculation of accuracy and
240 precision. Accuracy was better than 1–5% except for elements with abundances below 1 wt%, for
241 which it was better than 5–10%. Precision was typically better than 1–5% for all analyzed elements.
242 We also analyzed Sr isotopes on 5 whole-rock samples and mineral concentrates of K-feldspar,
243 clinopyroxene and phlogopite, belonging to sub-members A1, A2, B2, D2 and E2. The Sr isotopic
244 ratios were determined at the Radiogenic Isotope Laboratory of the Istituto Nazionale di Geofisica e
245 Vulcanologia, sezione di Napoli-Osservatorio Vesuviano. Powdered whole rocks samples (~ 0.1 g)
246 were leached with warm HCl for 10 min before dissolution. Sr was separated after HF-HNO_3-HCl
247 suprapur acid dissolution using standard column chromatographic methods, through Dowex
248 AG50WX-8 (200-400 mesh) cation exchange resins (Arienzo et al., 2013), and measured in static
249 mode by thermal ionization mass spectrometry (TIMS) using a Thermo Finnigan Triton TI.
250 Average $2\sigma_{mean}$, i.e., the standard error with N = 175, was better than ±0.000009. During the time of
251 isotopic data acquisition, NIST-SRM 987 standard gave a mean value of $^{87}Sr/^{86}Sr$ = 0.710231 ±
252 0.000019 (2σ, N = 169). External reproducibility (2σ) during the period of measurements was
253 calculated according to Goldstein et al. (2003). During acquisition, Sr isotopic ratios were

normalized for within-run isotopic fractionation to $^{86}Sr/^{88}Sr$ = 0.1194. The measured Sr isotopic ratios were normalized to the accepted value of NIST-SRM 987 ($^{87}Sr/^{86}Sr$ = 0.71025) standard.

3.2 Systems connectivity diagrams

The chemical variations recorded in compositional zoning patterns can be used to track the evolution of different populations of crystals through distinct magmatic environments in which they grew. Following Kahl et al. (2011, 2015), we used a population-based approach to investigate the different magmatic environments. The method was developed using olivines and has recently been applied to orthopyroxenes (Solaro et al., 2020), but has not been applied to clinopyroxenes yet to the best of our knowledge, although Mangler et al (2020) interpreted compositional zoning in a similar manner.

Minerals can be characterized by zones having constant composition for several microns along a direction: if a zone has a constant composition that differs from the constant compositions in surrounding zones, then a plot of such a concentration distribution as a profile along one direction has the shape of a plateau. Irrespective of whether the composition of the zone is higher or lower with respect to the surrounding zones, all of these flat regions in concentration profiles are referred to as “plateaus” in this work. The occurrence of plateaus in the zoning patterns of minerals, such as clinopyroxene, indicates that compositional zoning is not produced by pure fractionation, but that growth occurred for certain periods of time under stable conditions in response to fast changes of thermodynamic variables (pressure, temperature, oxygen fugacity or water fugacity). Consequently, plateaus with different composition represent several episodes of overgrowth of the crystals under different sets of P-T-X conditions. Each set of such thermodynamic variables characterizes a single magmatic environment. It is therefore possible to associate each compositional population, detected in the whole set of crystals, to a specific magmatic environment. As explained by Kahl et al. (2015), a magmatic environment does not necessarily represent a physical magmatic reservoir. Two magmatic environments could be parts of a single physical reservoir. For example, portion of a

zoned magma reservoir can differ from other parts of the same reservoir only because, for instance, the temperature is different while other variables remain fixed.

The approach uses connectivity diagrams, made up of boxes joined by lines, to systematically organize the chemical information and identify the number of magmatic environments recorded in such zoning patterns (e.g. Kahl et al., 2011 and reference therein). In the Systems connectivity diagrams, each box represents a distinct magmatic environment and each connection line indicates the composition of a crystal from core to rim, that is equivalent to the zoning type; a single arrow represents the passageway of a crystal (or a magma in which the crystal was forming), from one magmatic environments to another with different conditions. The density of the connection lines can be used to infer the dominant passageways of crystals in different environments. Such a schematic data representation immediately provides a whole picture of the zoning patterns. It is therefore possible to quantify the connections among the various magmatic environments (henceforth, ME), through the entire set of zoning pattern, in order to reconstruct the evolutionary history of crystals. Here we applied this approach to A-MS clinopyroxenes, in order to investigate growth of crystals in the different MEs that possibly characterized the A-MS plumbing system.

4 Results

4.1 Matrix-Glass

Matrix-glass analytical data (119 spots; Supplementary Material 2) have been acquired on representative samples of the A-MS eruption products. Matrix-glass shows an alkaline affinity (Na_2O+K_2O = 13.6–10.5 wt% and SiO_2 = 60.0–55.7 wt%) and mostly classifies as trachyte and subordinately as phonolite (Fig. 2a). The agpaitic index [A.I. molar $(Na^+ + K^+)/ Al^{3+}$] of A-MS glasses ranges from 0.97 to 0.75. Na_2O and K_2O contents range from 5.55 to 3.24 wt% and from 9.99 to 7.50 wt%, respectively. The Na_2O/K_2O ratio ranges from 0.70 to 0.33 while the CaO/Al_2O_3 ratio ranges from 0.19 to 0.09. TiO_2 and Al_2O_3 contents range from 0.75 to 0.17 wt% and from 19.8

to 18.1 wt%, respectively. $FeO_{(tot)}$ and MgO contents range from 4.27 to 2.58 wt% and from 1.12 to 0.33 wt%, respectively (Fig. 2 in Supplementary Material 1).

The analyzed A-MS matrix-glasses are Ne-normative and their Mg# [molar $Mg^{2+}/(Mg^{2+}+Fe^{2+})*100$] varies from 43 to 24. The Mg# of the whole-rocks, taken from literature (de Vita et al., 1999) for comparison, ranges from 45 to 31, thus slightly shifted toward less evolved compositions. SiO_2 and Na_2O contents show positive correlation with the degree of chemical evolution (decreasing Mg#; Fig. 2 in Supplementary Material 1), whereas CaO, MgO and $FeO_{(tot)}$ contents show negative correlation. K_2O content increases with Mg# decreasing from 43 to 30 and then decreases with Mg# decreasing from 30 to 24; Al_2O_3, and MnO contents are constant, although scattered. The degree of differentiation generally decreases from bottom to top of A-MS deposits. In fact, even if partially overlapped, there is a remarkable difference in the major oxide contents of the A-MS volcanic products sampled in the different members (from A to F). In particular, glass from members A to B show on average a slightly more differentiated composition than those from members D to F (Fig. 2a; Fig. 2 in Supplementary Material 1).

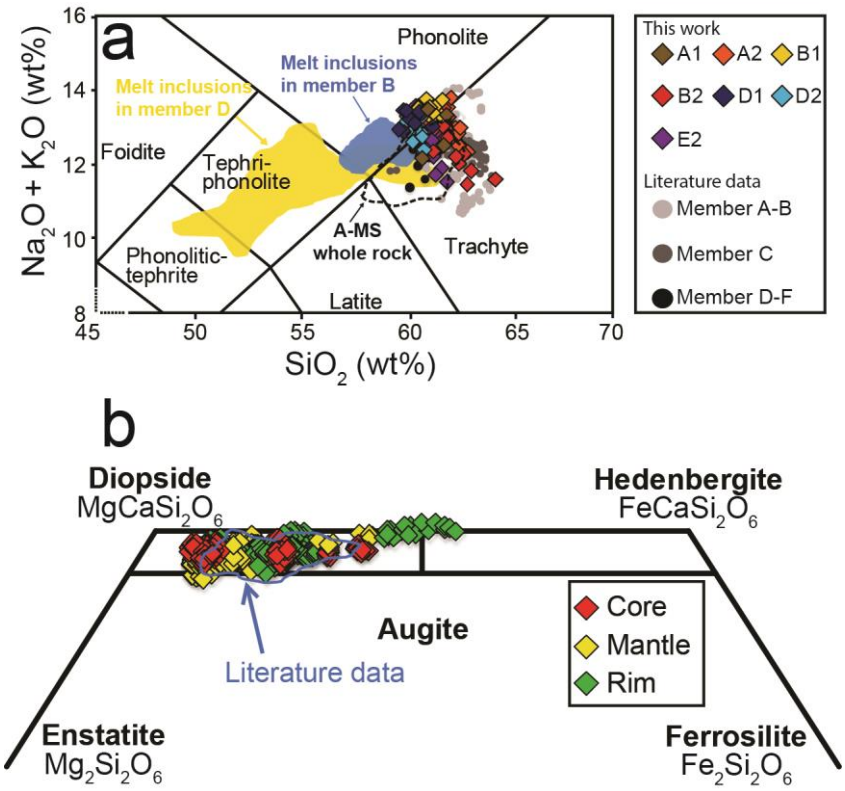

Fig. 2 a) Glass compositions of A-MS products plotted in the Total Alkali vs. Silica diagram; melt inclusion data are from Arienzo et al. (2010); whole rock and matrix-glass compositions are from de Vita et al. (1999). b) Di-Hd-En-Fs classification diagram of clinopyroxenes found in A1, B1 and D1 members of the A-MS deposits; literature data refer to clinopyroxene from A-MS products (de Vita et al., 1999; Arienzo et al., 2010); mantle refers to the zones/sectors of the crystals between the core and the most external rim.

.

4.2 Clinopyroxene

Clinopyroxene from A-MS deposit occurs as euhedral to anhedral dark green phenocrysts and microcrysts in the groundmass. Both kinds of clinopyroxene have a diopsidic composition (Wo_{51-54}-En_{49-30}-Fs_{27-4}; Fig. 2b). On the other hand, clinopyroxene shows a significant compositional heterogeneity that is well reflected in the Mg# [molar $Mg^{2+}/(Mg^{2+} + Fe_{tot})$ *100] which ranges from 92 to 45 (Fig. 3a). Na_2O, Al_2O_3 (Fig. 3d), TiO_2 (Fig. 3e) and FeO contents increase with decreasing Mg#. TiO_2 and Al_2O_3 contents range from 1.29 to 0.27 wt% and from 7.17 to 1.39 wt%, respectively (Fig. 3d-e). Na_2O content ranges from 0.87 to 0.10 wt% (Fig. 3b). The whole set of acquired data allowed to enlarge the already known compositional range of clinopyroxene from A-MS (cyan bordered field in Fig. 2b; de Vita et al., 1999; Arienzo et al., 2010).

About 300 separated clinopyroxene crystals have been selected and then observed under a polarizing microscope. However, quantitative compositional zoning profiles have been only measured on the 41 crystals showing optical evidence of compositional variations. These make up a minor percentage (~15%) of the overall population. On 46 of the remaining optically unzoned clinopyroxenes, single spots major and minor element concentrations have been acquired. The optically unzoned clinopyroxene crystals show a quite homogeneous composition (Supplementary Material 2): 40 out of 46 analyzed crystals have Mg#= 75±5 (Fig. 3a). Only four out of the 46 analyzed homogeneous clinopyroxene crystals show higher (Mg# = 87±5) values. Two other crystals exhibit lower (Mg# = 60±5) values.

346 4.2.1 Compositional populations

347 As for the zoned crystals, we refer mantle to define the optically discriminable zones between the
348 core and the rim. Frequency histograms (Fig. 3a-c) of core, mantle and rim compositions show that
349 there are different compositional populations. In particular, through the Mg# parameter (Fig. 3a;
350 Table 1), it is possible to clearly distinguish: 1) a population of compositions, hereafter referred to
351 as ME0, characterized by high Mg# (92-85), occurring in 70% of the analyzed zoned crystals, in
352 most cases represented by crystal cores; 2) a population, hereafter referred to as ME1, with Mg#
353 between 84 and 80, occurring in 34% of the analyzed zoned clinopyroxenes and that mostly
354 constitutes the mantles of the crystals; 3) a population of compositions, hereafter referred to as
355 ME2, with Mg# between 78 and 70 and with an average value of 75, occurring in all the analyzed
356 zoned clinopyroxenes and, in particular, in almost all their rims. Notably, this is also the
357 composition of the unzoned crystals, which make up 85% of the overall population. 4) a further
358 population is represented by few cores and mantles with low Mg# (69–60) found in 7% of the
359 zoned analyzed crystals, hereafter referred to as ME3. Moreover, the rim of a single crystal showing
360 very low Mg# (55–45) is also referred to as ME3 in Fig. 4. In summary, ME0 and ME2 make up
361 most of the zoned clinopyroxene population, with the most mafic compositions (ME0) generally
362 recorded in the cores. Although there are subtle variations in the distribution patterns of Al_2O_3 and
363 Na_2O contents of the pyroxene crystals that are discussed below in detail, the classification into
364 different groups is largely corroborated by these compositional parameters as well (e.g. Fig. 3).

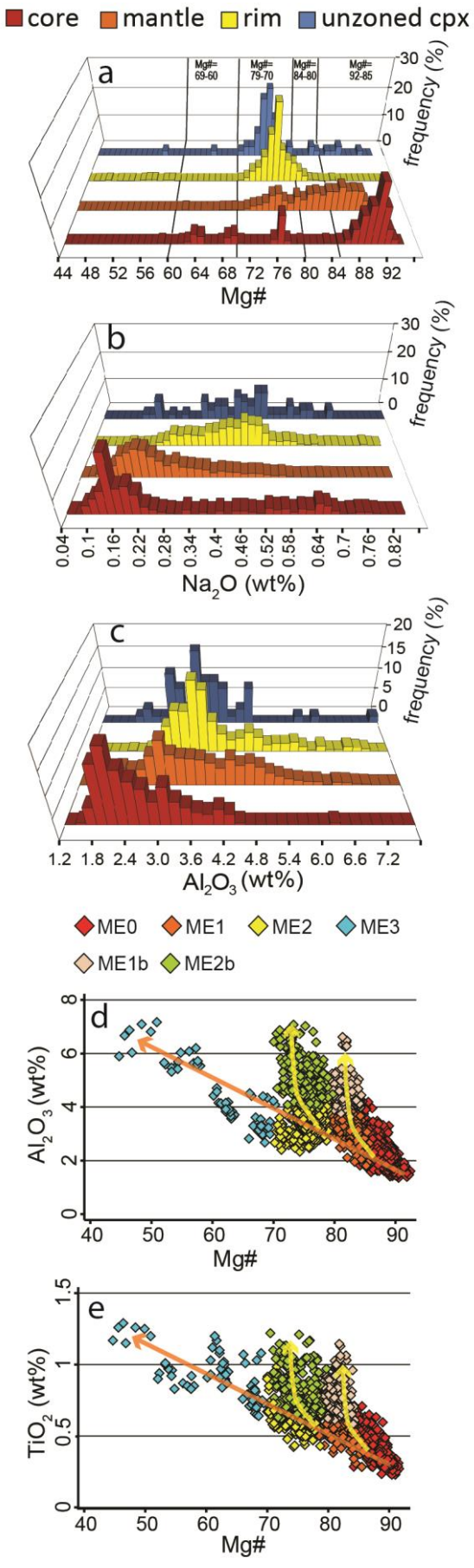
core
mantle
rim
unzoned cpx
a
Mg#= 69-60
Mg#= 79-70
Mg#= 84-80
Mg#= 92-85
frequency (%)
Mg#
b
Na2O (wt%)
c
Al2O3 (wt%)
ME0
ME1
ME2
ME3
ME1b
ME2b
d
e
TiO2 (wt%)

365

Fig. 3 a) Mg#, b) Na_2O and c) Al_2O_3 frequency histograms of core, mantle and rim of the zoned A-MS clinopyroxenes. These allow different populations to be identified. d) Al_2O_3 vs Mg# and e) TiO_2 vs Mg# variation diagrams of the analyzed zoned A-MS clinopyroxenes showing a wide compositional range and different populations and sub-populations. Note that all clinopyroxenes of different compositions lie on a trend defined by the orange arrow, with the exception of the ME1b and ME2b trends, which are shown in yellow. The significance of these trends is discussed in section 4.6.

The main difference between the three analyzed members is that only member B1 has a significant number (9 out of 15 analyzed crystals) of zoned clinopyroxene crystals with cores showing ME2 and ME3 compositions; in zoned clinopyroxene from the member A1, cores have only ME0 composition. Only 4 out of 20 cores of the crystals from member D1 show a ME2 composition. Indeed, member D1 has a large proportion of zoned clinopyroxenes (15 out of 20 analyzed crystals) with ME1 and ME0 composition; this is consistent with the composition of its matrix-glass, which is less differentiated with respect to the composition of A-B members. An important observation is that despite the wide compositional variability of cores and mantles, crystal rims show a homogeneous composition: except the crystal rim with very low Mg#, all crystal rims show Mg# between 78 and 70, thus pertaining to ME2. Nevertheless, Al_2O_3 and TiO_2 show an overlap in the compositional populations that are distinguishable based on their Mg# (Fig. 3). In particular, these elements show a wider compositional range in the populations of rims (ME2) and mantles (ME1), so it is possible to discriminate two other subpopulations (ME1b and ME2b), which, at similar Mg# values, are characterized by higher contents of Al_2O_3 and TiO_2 (Fig. 3d-e). Thus, in terms of Al_2O_3 and TiO_2, mantles and rims show a compositional heterogeneity, despite they have homogeneous MgO, FeO and Na_2O contents. This aspect will become relevant in the construction of diffusion models.

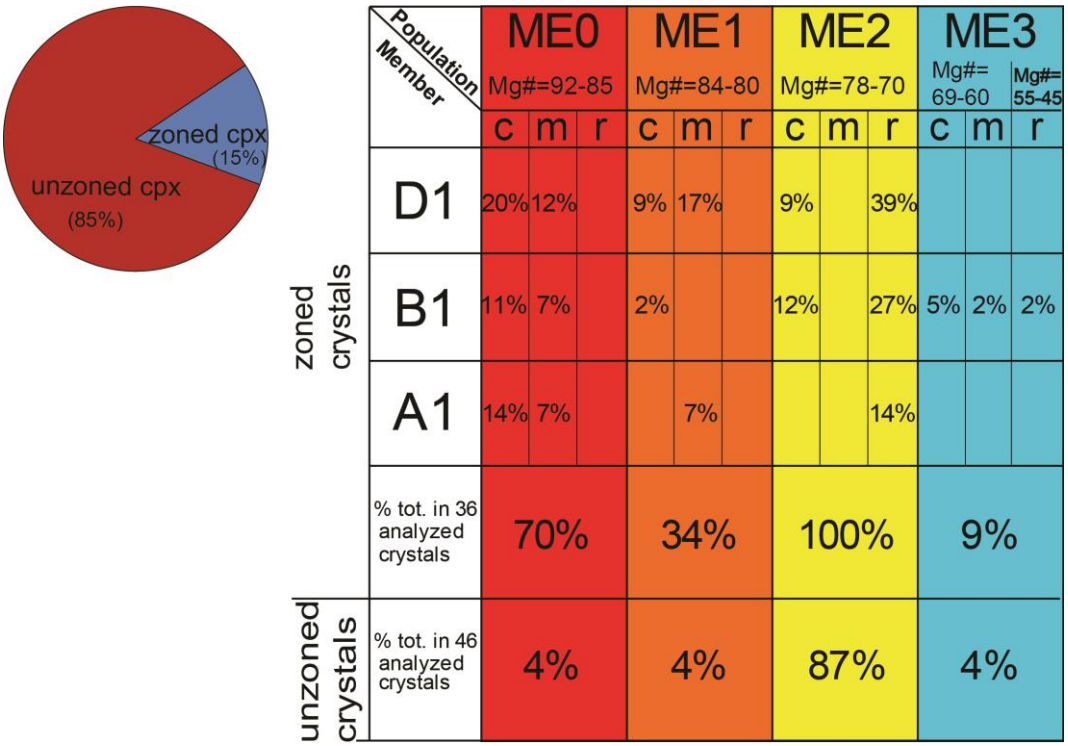

Fig. 4 The colored table reports, for each sub-member, the frequency of occurrence of a compositional population in a zoning sector (core, mantle or rim) in a total of 36 (out of 41) analyzed clinopyroxene crystals of the A-MS deposit; c=core; m=mantle; r=rim. Percentages have been calculated considering clinopyroxenes with plateaus (36 out of 41). Percentage of compositional populations occurring in the homogeneous clinopyroxene crystals is also reported. % tot.in rows at the bottom express the abundance of a compositional population in all the analyzed crystals (36 for the zoned and 46 for the unzoned crystals, respectively).

4.2.2 Compositional Zoning

The concentration profiles measured along core-to-rim traverses in zoned clinopyroxenes allowed to characterize their zoning patterns. In 36 out of 41 crystals, the zoning pattern of the main elements consists of two or more plateaus with a constant composition separated by either sharp or gradual boundaries (Fig. 5). Based on the chemical composition and the type of variation shown by plateaus, various types of zoning patterns have been identified, i.e. normal, reverse or complex. Normal zoning is defined by decreasing Mg# from core to rim while reverse zoning is characterized by increasing Mg# from core to rim of the clinopyroxene. Complex zoning refers to crystals

405 characterized by more than two plateaus, i.e. crystals showing normal-to-reverse zoning, in which
406 Mg# decreases from core to mantle and increases from mantle to rim.
407 The most common pattern (44%) is normal zoning (type I; Fig. 5a), consisting of cores with high
408 Mg# (92–80; ME0-ME1) and rims with intermediate composition (Mg# = 78–70; ME2) showing
409 sharp variation between these. Another type of zoning is type II (5%), that is similar to the normal
410 zoning type I, but differs in that the variation is gradual (Fig. 5b). Only one normally zoned crystal
411 (type III; Fig. 5c) shows a core with intermediate composition (Mg# = 75–73; ME2) and a rim with
412 low Mg# (55–45; ME3). Another less common zoning type (type IV; Fig. 5d; ~ 5%) is represented
413 by reversely zoned crystals in which cores with Mg# of 68–63 (ME3) are surrounded by rims with
414 less differentiated composition (Mg# = 75–73; ME2). Several types of complex zoning patterns are
415 also common. Most crystals have a reverse to normal zoning (type V; Fig. 5e; ~ 22%), with a core
416 characterized by intermediate composition (Mg# = 81–72; ME1 or ME2), a mantle with higher Mg#
417 (82–92; ME0 or ME1) and a rim with Mg# of 75–72 (ME2). An individual (type VI; Fig. 5f) from
418 member B1 shows a variation from Mg# = 75 (ME2) in the core, through Mg# = 63 (ME3) in the
419 mantle, to Mg# = 75 (ME2) in the rim. Finally, oscillatory zoned (type VII; Fig. 5g; ~ 7%) crystals
420 are also present, showing an alternation of zones consisting of several plateaus with composition
421 ranging from Mg# = 92–88 (ME0) to 84–82 (ME1) and a rim with Mg# = 75 (ME2). Moreover, a
422 few crystals (type VIII; Fig. 5h; ~ 12%) show normal or oscillatory zoning with gradual variation
423 (Mg# from 81 to 71) without plateaus.

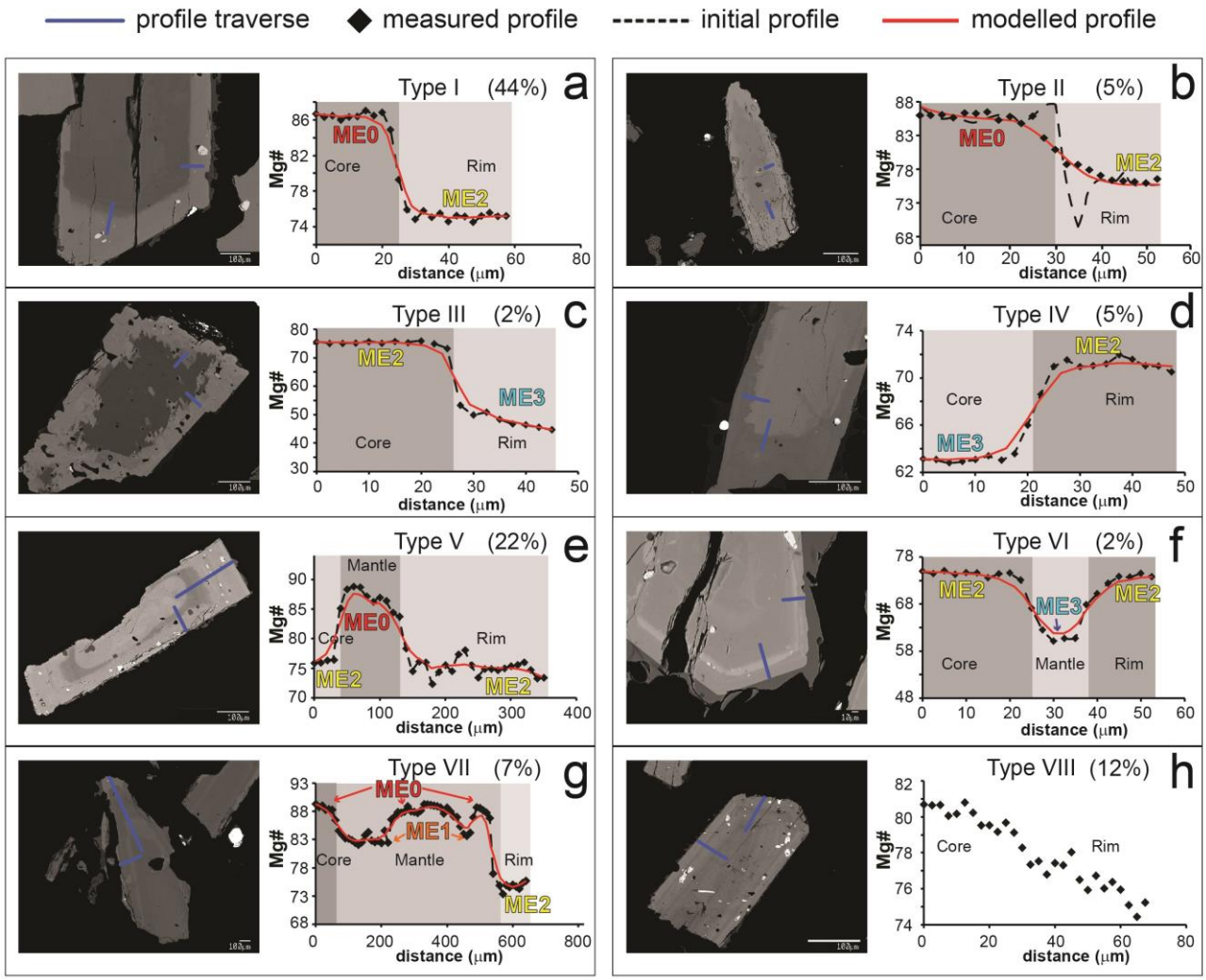

Fig. 5 Types of zonation of the A-MS clinopyroxenes. Black diamonds are measured analysis along the crystal traverses showing concentration profiles from core to rim [Mg# = molar $Mg^{2+}/(Mg^{2+} + Fe_{tot})$]. In the BSE images, the blue lines are the traverses along which the chemical composition has been acquired. Black dashed lines indicate the initial profile shapes: these are different depending on the two methods applied for diffusion modeling and have been inferred through the relationships between Al_2O_3 (wt%) and Mg# in the profiles Red lines indicate modelled profiles. A complete description of the diffusion modeling methods is provided in section 4.6. The numbers in brackets indicate the percentage of zoned clinopyroxenes exhibiting such a pattern.

4.3 Sr isotope composition of whole rocks and minerals

The whole-rock samples from the sub-members A1 and A2 show $^{87}Sr/^{86}Sr$ isotopic ratios = 0.70747. Whole rocks from sub-member B2 have a $^{87}Sr/^{86}Sr$ isotopic ratio = 0.70749, whereas samples from sub- members D2 and E2 show higher $^{87}Sr/^{86}Sr$ isotopic ratios that are 0.70753 and 0.70750, respectively (Fig. 6a). Feldspars from all the A-MS members show a Sr-isotopic signature in the

range 0.70750–0.70748 (Fig. 6b). The Sr-isotopic signature of clinopyroxenes shows a significant range of variation, increasing from 0.70745 in member A1 to 0.70756 in member D2 and then slightly decreasing to 0.70755 in member E2 (Fig. 6c). Only phlogopite crystals from member E2 have been analyzed and they show a $^{87}Sr/^{86}Sr$ value of 0.70753 (Supplementary Material 2). Notably, on average, the Sr isotopic ratios increase with stratigraphic height: this is particularly evident in whole rocks and clinopyroxenes (Fig. 6a, c). The new isotopic data acquired on whole rocks and mineral phases of the analyzed samples are reported in Supplementary Material 2 and are consistent with the range reported in literature (Fig. 6).

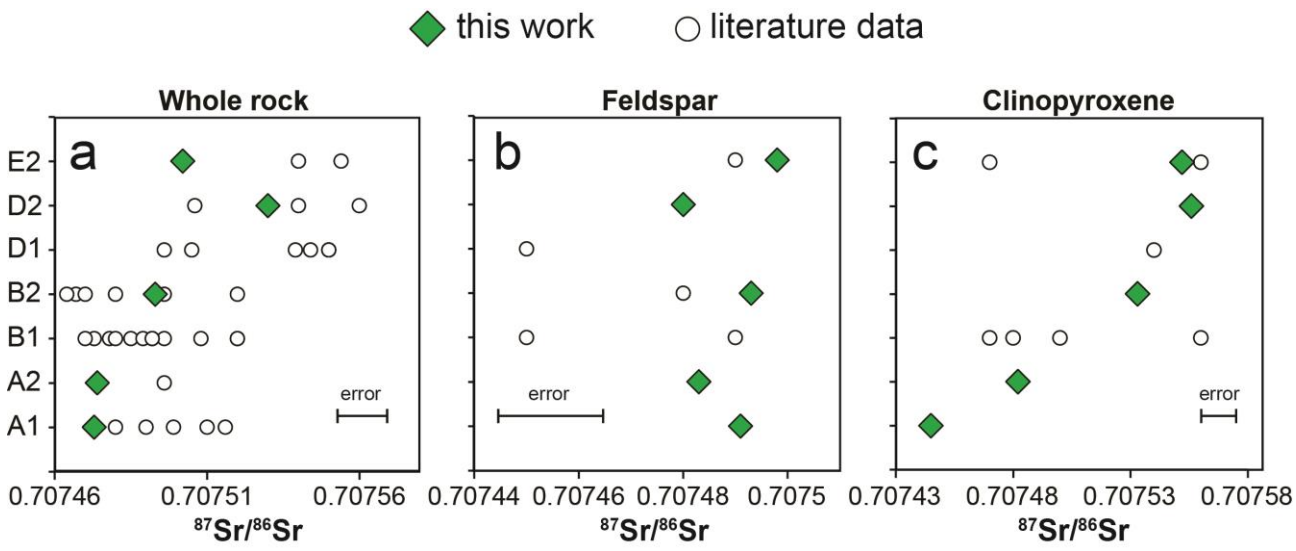

Fig. 6 Stratigraphic height vs Sr-isotopic composition of A-MS whole rocks and minerals. Literature data are from de Vita et al. (1999) and Arienzo et al. (2010).

4.4 P-T conditions of clinopyroxene crystallization

Clinopyroxene-liquid thermometers and barometers specific for alkaline magmas (Masotta et al., 2013) have been used in order to investigate the crystallization conditions of the A-MS clinopyroxenes. However, only few clinopyroxenes have passed the compositional test for equilibrium (Fig. 7a), implying that the majority of the crystals, mostly those belonging to ME0 and ME1, grew in a more mafic melt and were subsequently trapped in the A-MS trachytic magma. Nevertheless, we noted that some of these clinopyroxenes are in equilibrium with whole rocks

and/or melt inclusions representative of poorly evolved trachybasaltic to latitic Campi Flegrei magmas (Beccaluva et al., 1991; Civetta et al., 1991a; D'Antonio et al., 1999; Lustrino et al., 2002; Mastrolorenzo and Pappalardo, 2006; Cannatelli et al., 2007).

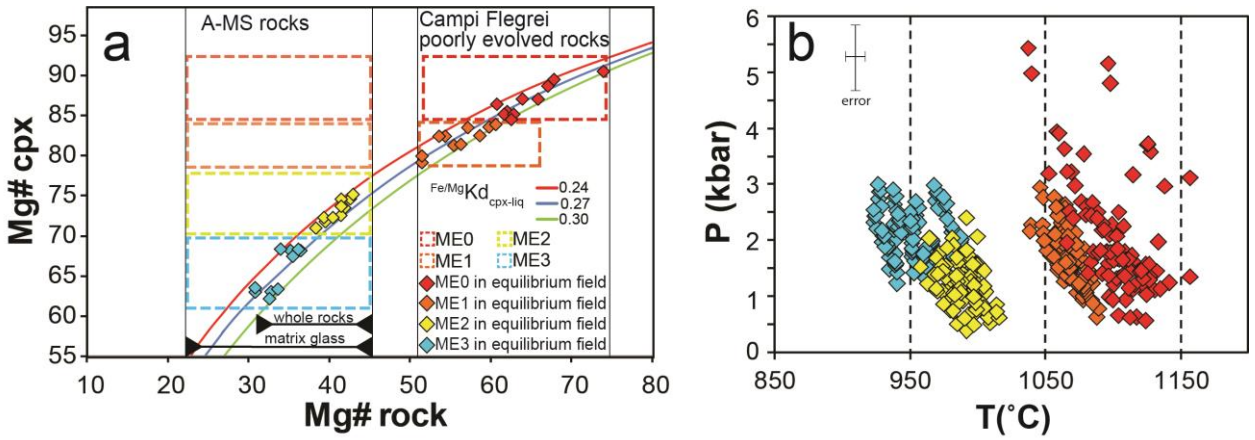

Fig. 7 a) Fe-Mg partitioning between clinopyroxene and host rock ($^{Fe/Mg}Kd_{Cpx\text{-}liq}$ = 0.27±0.03; Grove and Bryan, 1983; Putirka et al., 2003); fields demarcated by colored dotted lines represent the whole set of A-MS clinopyroxenes, belonging to different magmatic environments, compared to host rocks; the transparent colored dotted lines refer to clinopyroxenes with high Mg# (ME0 and ME1) compared to A-MS whole rocks and matrix glass compositions: these clinopyroxenes are out of equilibrium with respect to their host rocks; some of these clinopyroxenes are in equilibrium with more mafic rocks; diamond symbols refers to some clinopyroxenes which passed the compositional test for equilibrium and have been used for geothermobarometry. b) Output pressures and temperatures estimates for the different magmatic environments of the A-MS clinopyroxenes obtained by the clinopyroxene-liquid thermometers (equation Talk2012) and barometers (equation Palk2012) specific for alkaline magmas (Masotta et al., 2013); error bars refer to SEE.

We consider only clinopyroxene crystals in equilibrium with hypothetical melts, i.e. crystals from the ME0 and ME1 in equilibrium with Campi Flegrei poorly evolved volcanic products, and crystals from ME2 and ME3 in equilibrium with A-MS matrix-glass compositions (Fig. 7a). Different ranges of temperature have been obtained for the variable clinopyroxene populations (Fig. 7b; Supplementary Material 3). The most mafic compositions yield the highest temperatures, with averages of 1104±24 °C for ME0 and 1066±11 °C for ME1. Average temperatures for ME2 and ME3 are 990±13 °C and 952±18 °C, respectively. The standard error of estimate (SEE) of the used geothermometer (Masotta et al., 2013) is 18.2°C and hence, in the case of ME1 and ME2, it is

slightly higher than the standard deviation calculated from the output values. The estimated pressure is similar for all the populations ranging between 3.0 and 0.5 kbar, with an average value of ~ 1.7 kbar. Only a few output data show pressures >3 kbar. With the exception of a few clinopyroxenes from ME0 and by considering that the SEE of the geobarometer is 1.15 kbar, the obtained pressure range is the same for the different magmatic environments, which likely indicates that the resolution in pressure is not good enough to discriminate reservoirs at different depths.

4.5 Magmatic environments recorded in A-MS clinopyroxenes

In Fig. 8, the Systems connectivity diagram schematically shows the A-MS clinopyroxene zoning pattern.

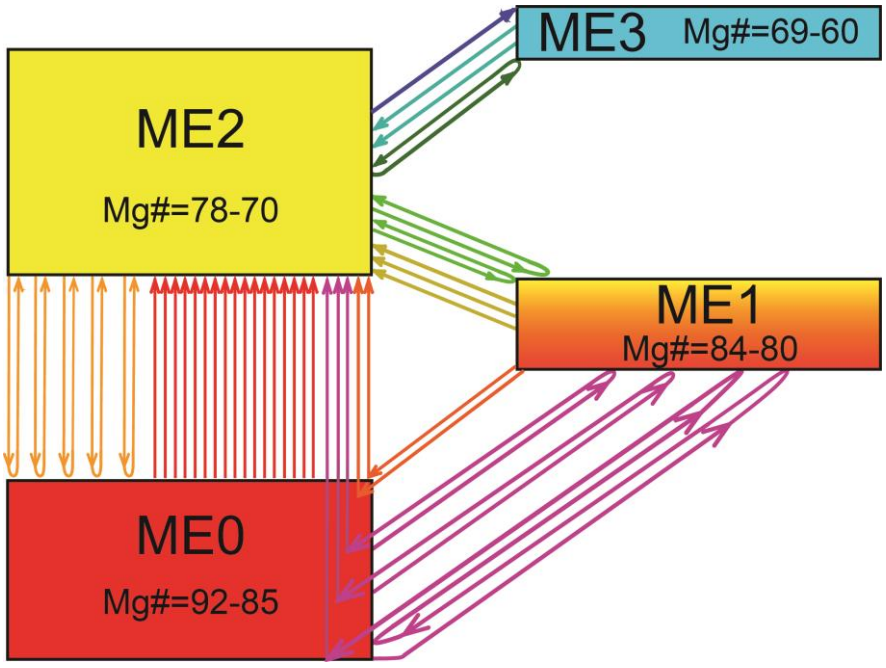

Fig. 8 Systems connectivity diagrams of the zoning patterns of A-MS clinopyroxene crystals. Since each compositional population can be associated to a specific magmatic environment (see section 3.2), the different magmatic environments are characterized by different ranges in the Mg#. Different zoning types are depicted by different connection lines represented by different color (e.g. the orange routes represent clinopyroxene crystals with core formed in ME2, mantle formed in ME0 and the rim formed in ME2). The height of the boxes is proportional to the frequency of occurrence of the magmatic environments. The A-MS clinopyroxene zoning patter is characterized by most of the connection lines linking ME0 and ME2, also passing through ME1, and a few connections linking ME2 and ME3.

Such an analysis reveals that, despite the complex diversity of zoning patterns, certain evolutionary tracks are recurrent in the history recorded by the clinopyroxene populations. It can be noted that there are many connections, depicted as arrows in Fig. 8, between the ME0 and ME2 environments. The connections often pass also through ME1 that represents an environment compositionally intermediate between ME0 and ME2. Finally, there is a much smaller number of connections between ME2 and ME3. Based on the available data, there are no connections between either ME0 or ME1 and ME3; this allows us to divide the evolutionary history of A-MS clinopyroxene phenocrysts into two steps: one involves the interaction among the magmatic environments ME0, ME1 and ME2, the other involves ME2 and ME3. Moreover, as also visible in the frequency histograms (Fig. 3), it is worth noting that both crystal cores with high Mg# (ME0) and crystal cores with low Mg# (ME3) converge toward an intermediate composition (ME2) at the rim. At this point it is necessary to recall that this distinction in different magmatic environments is supported by other compositional variables such as Na_2O, Al_2O_3 and TiO_2 contents, with the exception of the ME1b and ME2b groups of Al_2O_3 and TiO_2 contents that occur in the rim and mantle regions of the zoned clinopyroxenes. These will be discussed in detail in the following section on diffusion modeling.

4.6 Diffusion modeling

Kinetic modeling of the zoning patterns in clinopyroxene, which record fluctuations through the different magmatic environments, can yield information on the timescales over which the processes that created the different types of zoning took place. The well preserved plateaus found in most profiles can be used to infer the initial profile shapes before diffusion occurred. Given the different kinds of zoning profiles, two different methods for modeling have been used here. I. Most of the profiles, characterized by compositional plateaus and sharp gradients show little evidence of diffusive modification of growth zoning. In these cases, it is possible to calculate the relaxation of growth zoning timescales (e.g. see Chakraborty and Ganguly, 1991; Trepmann et al., 2004) to infer

maximum possible durations that the crystals may have spent in a magmatic reservoir at a given temperature without perceptible, within the analytical resolution of this study, diffusive modification of the profiles. II. In a small subset of profiles (e.g. Type II) diffusive gradients are observed and these can be modelled to fit the observed profiles and yield durations of residence of the crystals in a magmatic environment. In both cases, solutions to the diffusion equation

$$\frac{dC}{dt} = \frac{d}{dx}\left(D(t)\frac{d}{dx}\right) \qquad (1)$$

are sought with an appropriate choice of initial and boundary conditions. The equation describes how concentration gradients (i.e., concentration profiles: dC/dx), evolve as a function of time and this aspect is utilized to obtain information on timescales from measured concentration profiles (e.g. Chakraborty et al., 2008). We have carried out the diffusion modeling at temperatures corresponding to that of the ME2 environment (990 °C) because, in most cases, this is the final temperature at which clinopyroxenes grew and resided before eruption, at least for ~ 98% of the zoned crystals, as well as the homogeneous crystals, which make up 85% of the clinopyroxene population. We have used diffusion coefficients calculated using the expression provided by Müller et al. (2013):

$$D^{\mathrm{Fe-Mg}} = 2.77 \pm 4.27 * 10^{-7} \exp\left(\frac{-320.7 \pm \frac{16\mathrm{kJ}}{\mathrm{mol}}}{RT}\right) \mathrm{m}^2/\mathrm{s} \qquad (2)$$

where *R* is the gas constant and *T* is the temperature in Kelvin.

In the method I, the measured profiles are taken as the initial profiles and equation (1) and (2) are used to numerically calculate evolution of the profile shapes as a function of time. The boundary conditions for these calculations may be either constant composition or no flux at the rims of crystals, with little difference in the results. Timescales on which the calculated profiles deviate measurably from the initial profiles are considered to be upper limits of residence times of crystals in a particular magmatic environment. Fig. 5 (except Fig. 5b: Type II) shows examples of different kinds of profiles modeled through method I. The upper limit residence times for different plateau

compositions in the various types of zoning profiles are listed in Table 1. These are found to be < 25 years, with durations < 15 years being the most common.

Table1

Member	cpx n°-traverse n°	Method I	Method II
A1	cpx1-1	14.3	
	cpx1-2	15.5	
	cpx2-1	6.7	
	cpx2-2	6.7	
	cpx3-1		48.2
	cpx3-2		37.8
	cpx5-1		68.2
	cpx5-2		61.0
B1	cpx1-1	8.9	
	cpx1-2	8.9	
	cpx2-1	8.9	
	cpx2-2	7.1	
	cpx4-1		48.3
	cpx4-2		52.6
	cpx5-1	12.7	
	cpx5-2	9.5	
	cpx6-1	4.8	
	cpx6-2	4.8	
	cpx7-1	14.3	
	cpx7-2	4.8	
	cpx8-1	9.5	
	cpx8-2	12.7	
	cpx9-1	20.9	
	cpx9-2	7.6	
	cpx10-1	11.4	
	cpx10-2	8.6	
	cpx11-1		47.2
	cpx11-2		52.5
D1	cpx2-1	14.3	
	cpx2-2	6.8	
	cpx5-1		43.8
	cpx5-2		50.6
	cpx7-1	10.5	
	cpx7-2	11.1	
	cpx8-1	14.3	
	cpx8-2	9.5	
	cpx9-1	6.1	
	cpx9-2	8.6	
	cpx10-1	20.3	
	cpx10-2	6.7	
	cpx11-1	18.0	
	cpx11-2	6.7	
	cpx13-1	24.7	
	cpx13-2	7.9	
	cpx14-1	8.6	
	cpx14-2	5.2	
	cpx18-1	9.4	
	cpx18-2	7.9	
	cpx19-1	12.9	
	cpx19-2	5.3	

Table 1 Timescale (in years) estimates for Agnano-Monte Spina clinopyroxene crystals derived from Fe-Mg diffusion modeling across selected transects, calculated at T = 990 °C. In method I, the measured profile has been used as initial profile and the time term of the equation (1) has been varied until the modeled profile slightly oversteps the initial profile: the maximum diffusive smoothing

557 that a concentration (Mg#) profile has undergone has been modeled, thus yielding maximum times of residence. In method II, the
558 shape of the initial profile has been inferred from the relationship between Al_2O_3 and Mg# (Fig. 8); the residence times have been
559 modeled by obtaining the fit with the measured profile.
560
561 In the method II, on the other hand, it is necessary to define the shapes of the initial profiles and
562 then model their diffusive modification. To do that, element concentrations that are correlated with
563 each other through petrogenetic processes but diffusing at different rates are useful. Here we make
564 use of Mg# and Al_2O_3 concentration in the clinopyroxene crystals, which are anti-correlated with
565 each other (e.g. see Fig. 3) because Mg-content decreases as Al-content increases during fractional
566 crystallization as well as partial melting processes (e.g. Jagoutz et al., 1979). As discussed above
567 (see caption of Fig. 3), there are two groups of compositions, ME1b and ME2b, that deviate from
568 this trend. It is possible to reliably infer the initial profile shapes of crystals which exhibit this
569 characteristic: by plotting Al_2O contents vs Mg# in a profile, it is possible to obtain a linear
570 correlation. Most of crystals show a good correlation, as shown by the fit of the data by a linear
571 trend-line (in Fig. 9a, R^2=0.94). This correlation can be then used to infer the hypothetical initial
572 Mg# profile, plotted in figure 9b. Within the accuracy of the data, it is hardly possible to see the
573 difference between the measured profile and the theoretical profile, in particular, in the region with
574 the sharp compositional gradient. This implies that the Mg# profile was little or even not at all
575 affected by Fe-Mg interdiffusion. For these crystals, it has been possible to estimate a maximum
576 timescale using method I: in this case, since the inferred profile is very similar to the measured
577 profile, the latter has been used as initial profile in the modeling. It is then possible to deduce that
578 where Mg# and Al_2O_3 are correlated according to the overall general trend, the profiles of Mg# and
579 Al_2O_3 track each other completely and the shapes overlap with each other. Conversely, when Al_2O_3
580 content is higher at a given Mg# compared to the value expected from the overall correlation trend,
581 such as for crystals showing ME1b and ME2b trends (Fig. 3e-f), the Al_2O_3 preserves a sharper
582 gradient whereas the Mg# shows more smoothed concentration patterns (e.g. zoning Type II). In

583 this case, the correlation between Mg# and Al_2O_3 content is not good (in Fig. 9c, R^2=0.74),
584 indicating that the original trend was overprinted by Fe-Mg interdiffusion. It is possible to estimate
585 an original trend by taking the Mg# and Al_2O_3 contents of the two plateau regions, which is plotted
586 as blue line in Fig. 9c. This original correlation has been used to estimate a growth zoning of Mg#,
587 which is the initial profile in Fig. 9d. We observe that the Mg# theoretical initial profile noticeably
588 deviates from the measured profile and the strongest difference is in the region with the large
589 compositional gradient of Al_2O_3. An example of such a profile, with the initial and the final
590 modelled profile shapes is shown in Fig. 5b and Fig. 9c-d. This indicates that Mg has diffused to
591 some extent and Al has not and this is consistent with the known experimentally measured diffusion
592 behavior of these elements (Mg vs. Al) in clinopyroxenes (e.g. Fe-Mg: Müller et al., 2013; Al:
593 Sautter et al., 1988). Thus, the shape of the Al_2O_3 profile can be taken as the initial profile shape for
594 Mg# (i.e. as a grown profile) and diffusion modeling may be used to try to reproduce the measured,
595 diffused concentration profile shape of Mg#. We have modelled the system as an infinite diffusion
596 couple, i.e. boundary conditions are $C = C_{initial}$ at $\pm\infty$ (i.e. the two ends of a profile). Two
597 compositional traverses were acquired across each clinopyroxene crystal. If modeling of both
598 profiles did not yield the same time estimates the values were not used because the concentration
599 profiles were considered to be affected by processes other than diffusion or artefacts such as oblique
600 sectioning effects (Costa et al., 2008). On the other hand, the fact that in many cases the same
601 timescales were obtained from profiles that are oriented in mutually perpendicular directions may
602 point to a limited anisotropy of Fe-Mg diffusion in clinopyroxene; that indeed has not been
603 measured experimentally yet.

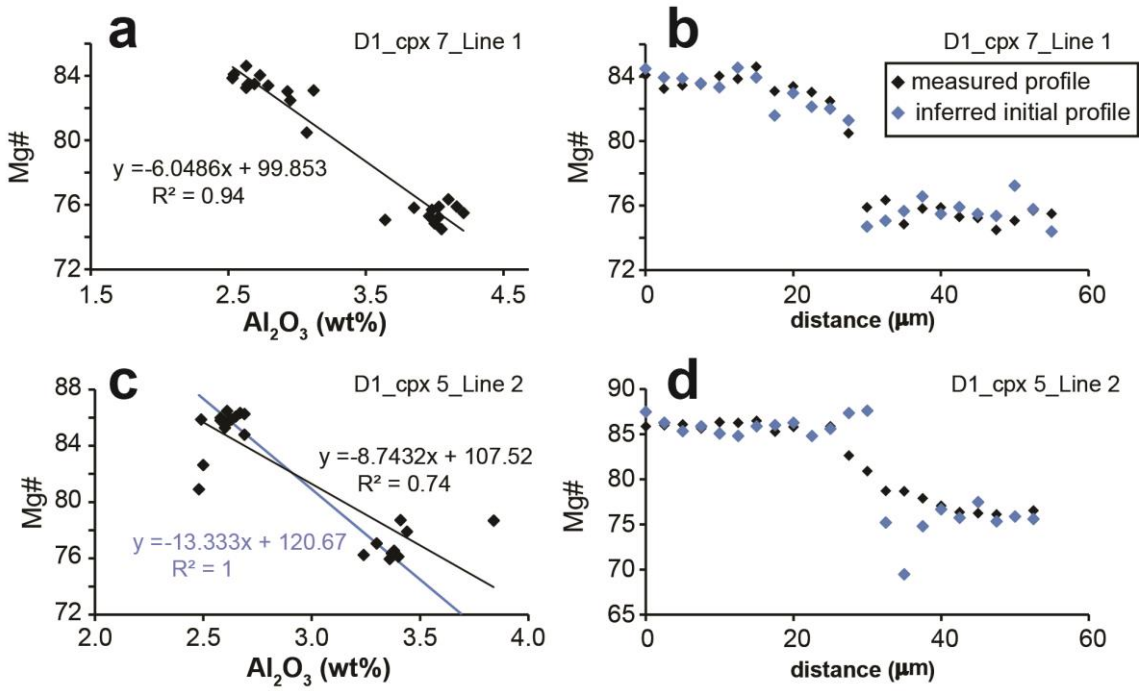

Fig. 9 a,c) Mg# vs Al_2O_3 (wt%) relations of two selected crystal profiles. b,d) measured and inferred initial Mg# profiles. In Fig. 9a, the profile show a good correlation (R^2=0.94; black trend-line) between Mg# and Al_2O_3 (wt%). In Fig. 9b, the inferred initial profile is calculated based on the relations assessed by best fit of the linear trend-line of Fig. 8a. In Fig. 9c, the profile does not show a good correlation (R^2=0.74; black trend-line) between Mg# and Al_2O_3 (wt%). By taking into account the Mg# and Al_2O_3 (wt%) contents of the two plateaus (without the points in the boundary region between the plateaus), a new best fit (R^2=1; blue trend-line) has been estimated. In Fig. 9d, the inferred initial profile is calculated based on the best fit shown by the blue trend-line. Since Mg# And Al_2O_3 are correlated, the inferred profiles (blue diamonds in Fig. 9b,d) can be taken as growth profiles. Such an analysis implies that crystal profiles showing a good match between measured and inferred profiles (e.g. Fig. 9b) have been little, or not at all, affected by diffusion. On the other hand, crystal profiles showing differences between measured and inferred profiles (e.g. Fig. 9d) have been affected by diffusion.

Timescale information has been extracted only from crystals showing concentration profiles suitable for diffusion modeling using one of the two methods described above: for example, crystals with profiles belonging to zoning type VIII (Fig. 5h) have not been used for the modeling. Altogether, we applied diffusion modelling to 25 crystals with 50 measured profiles of different Types (Table 1). All calculated timescales are shown in Fig. 10 where it should be borne in mind that timescales obtained using method I are upper limits of residence times in the magmatic

environment ME2, while those obtained using method II are residence times themselves. As seen in the figure, most crystals were amenable to modeling the relaxation of growth zoning using method I, while 10 profiles from 5 crystals, i.e. 2 profiles in mutually perpendicular directions, were suitable for modeling using method II. All of the profiles modelled using method II yielded timescales that were consistent with each other from the mutually perpendicular profiles. These timescales range between 38 and 68 years. Stratigraphically, two of these crystals come from members A1 and B1 and one from member D1. We discuss the implications of these results for the nature of the plumbing system in the following section.

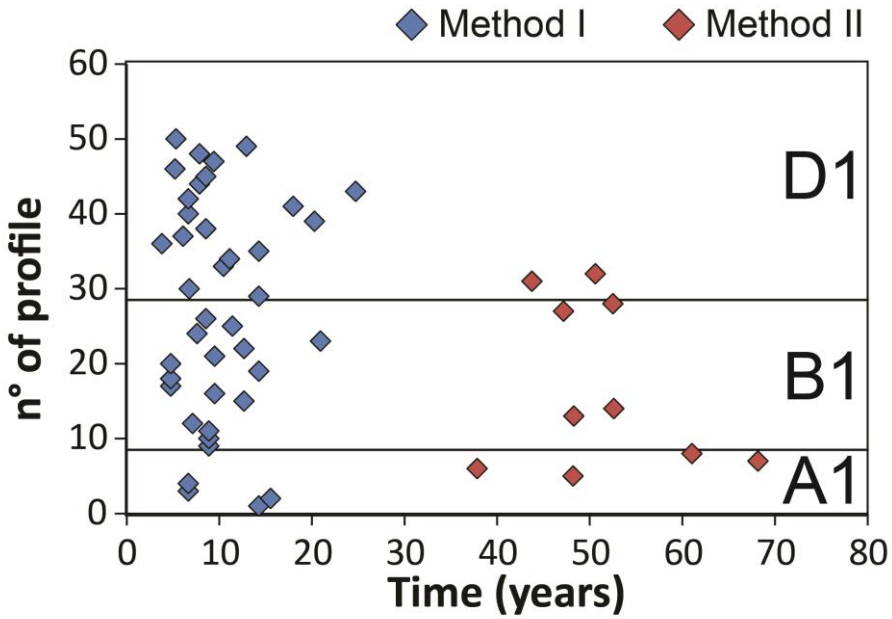

Fig. 10 Output values of times obtained by diffusion modeling on 50 out of 82 analyzed profiles on clinopyroxene crystals. Method I yields the upper limits of residence times of crystals in a magmatic environment; method II yields the residence times of crystals in a magmatic environment.

5 Discussion

5.1 The magmatic plumbing system of Agnano-Monte Spina eruption

Taking into account the composition and temperature, the magmatic environment ME0 can be associated with primitive magmas, especially for the high Mg# (> 91). The ME2 composition (Mg# 78–72) is the most widespread in the volcanic products erupted during all epochs of the Campi

641 Flegrei activity (e.g. de Vita et al., 1999; Munno and Petrosino, 2004; Marianelli et al., 2006; Piochi
642 et al., 2005; Cannatelli et al., 2007; Fedele et al., 2008; Mangiacapra et al., 2008; Arienzo et al.,
643 2010, 2015, 2016; Melluso et al., 2012; Belkin et al., 2016; Forni et al., 2018). This suggests a
644 common magmatic environment for most of the Campi Flegrei clinopyroxenes. Hence, taking into
645 account the estimated T-P, ME2 is ascribable to a crustal reservoir of the Campi Flegrei magmatic
646 system, in which clinopyroxenes with Mg# 78–72 formed. The composition of the ME2 population
647 is the most widespread in the A-MS clinopyroxene crystals, making up 87 % of the homogeneous
648 clinopyroxenes as well as the final, rim compositions of almost all (98 %) zoned crystals (Fig. 3a;
649 Fig. 4). On this basis it is reasonable to interpret the ME2 environment as the physical reservoir in
650 which most of the magmatic interaction(s) took place. In fact, mixing of the ME0 and ME2 melts
651 would produce a magma with intermediate composition, from which clinopyroxenes of composition
652 ME1 (Mg# 84–80) might have grown. The chemical composition of environment ME3 has been
653 found in only 3 out of the total 41 analyzed crystals; being ME3 a different environment, it is
654 characterized by a different set of thermodynamic variables with respect to those of ME2, i.e. it can
655 be characterized by lower temperature (Fig. 7b); since the ME3 composition is more evolved with
656 respect to those of ME2, thus ME3 could represent the most evolved, less-abundant portion of the
657 ME2 magmatic reservoir. Alternatively, the ME3 composition could have been produced by
658 degassing of the ME2 melt, during the stages of magma ascent. Therefore, we can hypothesize that
659 the history recorded in the A-MS clinopyroxene chemical compositions and the behavior of such a
660 plumbing system may be read as illustrated by the schematic diagram shown in Fig. 11: one or more
661 inputs of mafic magma(s) (ME0), originating from partial melting of the mantle, refilled a crustal
662 reservoir already hosting a more evolved resident magma (dominantly ME2, minor ME3), with
663 consequent formation of intermediate compositions (ME1). The isotopic disequilibrium between
664 several A-MS mineral phases and their host rocks (Fig. 5), as already reported in the literature (de
665 Vita et al., 1999; Arienzo et al., 2010), supports such a mixing/mingling process.

Since the whole rock and glass composition of A-MS products ranges from trachyte to phonolite, the amount of mafic magma that might have interacted with the evolved resident magma(s) must have been limited. This is in good agreement with what has been already suggested by Arienzo et al. (2010), who modeled the mixing process and proved that less than 10% of a mafic magma with average $^{87}Sr/^{86}Sr \approx 0.70754$ mixed with an evolved one with an average $^{87}Sr/^{86}Sr \approx 0.70749$. This would explain the occurrence of melt inclusions with less differentiated composition in the A-MS clinopyroxenes (Fig. 2a). Such a hypothesis also explains the Sr-isotopic signature of the analyzed A-MS rocks and minerals: both matrix-glass and clinopyroxene crystals from the D-E members, which show a less evolved composition with respect to those from A-B members (Fig. 2a, Fig. 4), are characterized on average by $^{87}Sr/^{86}Sr$ values higher than those of whole rocks and clinopyroxenes from A-B members (Fig. 6). Moreover, the $^{87}Sr/^{86}Sr$ values of feldspars from all the A-MS members are in the range of that of whole rocks from members A-B (Fig. 6a-b); such a Sr-isotopic ratio is the typical Sr-signature of the evolved Campi Flegrei magma component identified by Arienzo et al. (2016). Since this is the most evolved magma component, it can be associated with our ME2 and ME3, while the more mafic magma could be represented by our ME0.

The hypothesized recharge scenario (Fig. 11) is also supported by the texture of some crystals, which show resorbed cores (Fig. 5), which is often indicative of disequilibrium due to incorporation within a new host magma (e.g. Ubide et al., 2015, 2019; Astbury et al., 2018; Ubide et Kamber, 2018).

This kind of mixing behavior is consistent with the nature of the clinopyroxene population as well, where ME0 and ME1, that represent the mafic magma, are statistically far less abundant than clinopyroxenes with ME2 composition.

The hypothesized mixing process is also consistent with the observed chemical zoning patterns in the clinopyroxenes. Injection of ME0 mafic magma into the ME2 environment/physical reservoir would produce crystals with cores of ME0 composition (Mg# 92–85) and rims of ME2 composition (Mg# 78–70) and vice versa, as shown by the most common zoning types: Type I and Type V,

692 respectively. Mingling of ME0 and ME2 have probably caused the growth of ME1 composition in
693 the A-MS clinopyroxene, as testified by the somewhat less common Type VII and Type VIII zoning
694 patterns. Oscillations between these compositions (e.g. Type VII) would suggest long lasting
695 connectivity between the reservoirs such that crystals could be transferred from one environment to
696 another, sometimes back and forth. Type III, type IV and type VI zoning pattern (Fig. 5 c, d, f)
697 suggest that crystals can be transferred from ME2 to ME3 environment and vice-versa, i.e. due to
698 partial overturn caused by input of the ME0 melt.
699 Based on the above, we therefore hypothesize that batches of high temperature (~ 1100 °C) mafic
700 magma (ME0) with primitive composition, i.e. very high Mg#, low Ti, Al and Na contents, arrived
701 in a magma reservoir (Fig. 11a) where they partially mixed with a pre-existing more evolved
702 magma (ME2), leading to the formation of intermediate compositions (ME1; Fig. 11b). The mafic
703 input could have caused perturbation in a zoned reservoir and promoted interaction between the
704 chemically different magmatic portions (ME2-ME3; Fig. 11c).
705 Since ME3 has been found only in member B1, it probably represents the most evolved least-
706 abundant portion of the A-MS magmas erupted during the first Plinian phase of the eruption.
707 Furthermore, as a greater number of high Mg# core crystals are present in D1 compared to A1 and
708 B1 members, we hypothesize that the magma which led to the eruption of the second main fallout
709 deposit (D1), may have resided near the floor of the ME2 reservoir and may have been more
710 affected by the ME0 batches of mafic magmas, likely deeper, although good barometric constraints
711 are not available. However, few barometric estimates show pressures >3 kbar (Fig. 7b), implying
712 that some clinopyroxenes from ME0 could have started crystallizing at higher pressures. Moreover,
713 some crystal cores have higher Na_2O and Al_2O_3 contents (Fig. 3b-c), which could reflect
714 crystallization under higher pressure (e.g. Nimis, 1995; Putirka, 2008).These pressure values also
715 agree with estimates obtained from previous studies on the A-MS (Roach, 2005; Arienzo et al.,
716 2010; Iovine et al., 2017a) and the PVD crystallization pressures (Perinelli et al., 2019; Bonechi et
717 al., 2020).

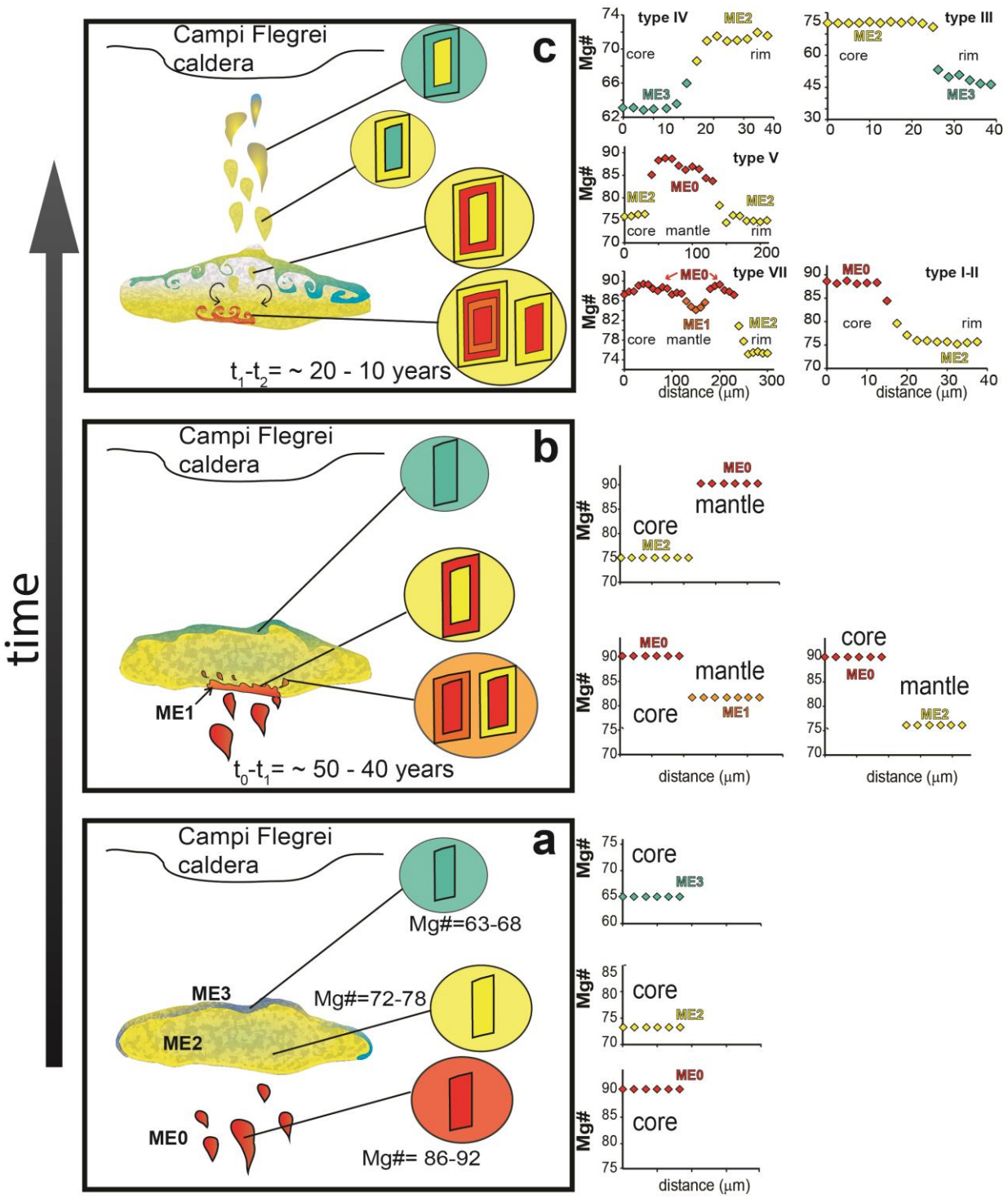

Fig. 11 Schematic sketch illustrating the magmatic processes occurred in the A-MS plumbing system. a) three distinct magmatic environments at a t = 0: one (ME0), in red, in which core of clinopyroxenes with high Mg# (92–85) were formed, is associated with primitive magmas; an environment (ME2), in yellow, ascribable to a crustal reservoir of the Phlegraean magmatic system, in which core of clinopyroxenes with Mg#78–70 were formed and an environment (ME3), in blue, identifiable with a less abundant, most differentiated magma portion of the ME2 reservoir. b) The interaction between ME0 and ME2 explains the normal zoning for clinopyroxenes of ME0 and, conversely, the reverse zoning for clinopyroxenes of ME2, also leading to the formation of intermediate compositions (ME1). c) The interaction between ME2 and ME3 justifies the whole set of observed zoning patterns in the A-MS

clinopyroxene; t_2-t_1 represents the time span of the mixing events recorded by crystals modeled through method II; t_1-t_0 represents the time span of the recharge events possibly due to increase of mafic magma input recorded by crystals modeled through method I; t_0= time of the eruption.

5.2 Timescales of processes in the Agnano-Monte Spina plumbing system

Diffusion modeling of the chemical zoning profiles provides us temporal constraints on pre-eruptive processes. Overall, the plumbing system that led to the A-MS eruption appears to have been active on decadal timescales. Most types of zoning patterns observed in the clinopyroxene crystals, showing little or no evidence of diffusive modification at the spatial resolution at which the compositions were studied in this work, have presumably recorded the latest phases of the pre-eruptive processes. This allows an upper limit to the duration of their residence in the ME2 magmatic reservoir to be placed and it is on the order of 10–15 years for the majority of the crystals. More specific constraints are provided by a small subset (5) of crystals having high Al-Ti compositions, represented by sub-environments ME1b and ME2b, that record diffusive modification. Al- and Ti- contents tend to show disequilibrium distributions due to their slow diffusivity in the crystals as well as in the melts, and such evolutionary trends as those shown by yellow arrows in Fig. 3d-e have been shown experimentally and empirically to be related to such disequilibrium (e.g. due to high cooling rates; Mollo et al., 2010, 2013; Ubide and Kamber, 2018). Crystals recording such disequilibrium between Al and Mg contents can be used for diffusion modeling. These crystals indicate that a timescale of ~ 40–70 years elapsed between the entrapment of the ME0 crystals into the ME2 reservoir and the eruption. These results explain why diffusive modification can be seen in some crystals and not in others even though they are compositionally almost identical: some of these crystals have resided longer in the crustal reservoir (ME2 environment). The rarity of such crystals, and the fact that back-and-forth transmission between ME0 and ME2 is recorded (e.g. Fig. 8), suggest the following scenario: a long lived connectivity existed between the ME0 and ME2 environments over several decades such that crystals could be

752 transferred back and forth. Only a few crystals resided in the ME2 reservoir for several decades.
753 These were erupted when the extent of ME0 magma input considerably increased, as recorded by
754 the major population of zoned crystals, within 10–15 years before the eruption.
755 Fig. 11 also explains the systematics of zoning pattern shown in Fig. 4 and Fig. 8. At the start of the
756 eruption (member A), likely triggered by increased input of mafic magma, crystals from the main
757 ME2 reservoir with cores of ME0 and rims of ME2 are erupted. Subsequently, as the reservoir is
758 gradually emptied, more and more crystals with cores of ME2, mantles of ME0-ME1 and rims of
759 ME2 are erupted (member B). At this stage, increased degassing may have produced more ME3
760 crystals as well. With progressive eruption, magma from the deeper, less evolved reservoir made its
761 way directly to the surface, with an increased contribution of less evolved melts as well as
762 clinopyroxene crystals (member D). In the course of the eruption then the ME2 reservoir was
763 partially or completely emptied, establishing a direct link between the more primitive environment
764 and the eruptive conduit during the later stages of the eruption (i.e. D1).
765
766
767 **5.3 Comparison with results of other timescale calculations for the Campi Flegrei caldera**
768 Although constraints on depths of the magmatic environments that were identified based on the
769 systems analysis of compositional zoning in clinopyroxenes are poor, we can use results from other
770 studies (e.g. Zollo et al., 2008; Arienzo et al., 2010; Pappalardo and Mastrolorenzo, 2012; Arzilli et
771 al., 2016; Di Vito et al., 2016; Zdanowic et al., 2016; Fedi et al., 2018; Voloschina et al., 2018) that
772 used different geological, geochemical or geophysical information to tentatively associate the
773 magmatic environments to reservoirs at different depths. It is possible that the deeper reservoir at
774 >10 km depth inferred in those studies is primarily associated with the less evolved ME0
775 environment while the shallower reservoir at < 8 km is primarily associated with the dominant ME2
776 reservoir. The overall assembly of eruptible magma which fed large eruptions occurs over relatively
777 long timescales (e.g. ~ 6.4 kyr in the case of the Campanian Ignimbrite eruption; Arienzo et al.,

778 2011) but processes within magmatic plumbing systems occur on a hierarchy of shorter timescales.
779 The timescales of different processes that occurred in the plumbing system of Campi Flegrei have
780 been determined using a variety of methods (e.g. Arienzo et al., 2011; Pappalardo and
781 Mastrolorenzo, 2012; Montagna et al., 2015; Perugini et al., 2015; Wu et al., 2015; Arzilli et al.,
782 2016; Di Vito et al., 2016; Iovine et al., 2017; Astbury et al., 2018). Various lines of evidence point
783 to the fact that degassing of rising magma plays an important role in the system (Mastrolorenzo and
784 Pappalardo, 2006; Montagna et al., 2015; Chiodini et al., 2016; Astbury et al., 2018; Forni et al.,
785 2018) and that a short-lived episode of enhanced degassing occurs over hours to days before an
786 eruption (e.g. Arzilli et al., 2016; Astbury et al., 2018; Pappalardo and Mastrolorenzo, 2012;
787 Montagna et al., 2015). Such a transient (and hence less frequently recorded), degassed magmatic
788 environment could be represented by ME3, for example. Note that such degassing promotes
789 crystallinity (e.g. Moretti et al., 2014; Arzilli et al., 2016), which may have produced the ME3
790 composition clinopyroxenes as well as the microlites that record a history of a few hours to days.
791 Comparable or even more rapid timescales have been obtained for magma mingling processes in the
792 Campi Flegrei magmatic system (e.g. tens of minutes; Perugini et al., 2015). As melts move
793 between these reservoirs, they adapt to the local magmatic environment (i.e. new P, T oxygen
794 fugacity, partial pressure of fluids) almost instantaneously. However, the crystal cargo of such melts
795 would require much longer to adapt to the new conditions, and the residence times of crystals of
796 different minerals have been consistently found to be on the order of decades or even longer using a
797 variety of minerals and methods, e.g. < 60 years based on Ba-zoning in sanidine (Iovine et al.,
798 2017); few centuries for the coarsest feldspar crystals based on CSD (Pappalardo and
799 Mastrolorenzo, 2012); few years to decades based on CSD of some microlites (Wu et al., 2015) and
800 zoning in clinopyroxene (this study).
801 These may be considered in the context of the plumbing system connectivity and timescales
802 inferred above to develop an integrated picture. Taken together, this information would be
803 consistent with a system where a long-lived magma reservoir at depths of >10 km containing a

shoshonitic-latitic magma, corresponding to ME0 of this study, is connected to a shallower (< 8 km) reservoir containing a more evolved magma (e.g. trachyte), corresponding to ME2 of this study, over decadal, or even century, timescales. Entry of the more mafic magma in the more evolved reservoir/mush zone could lead to melting/assimilation and mixing, leading to the formation of a reservoir such as ME1 (Fig. 11). Melts transported from one environment to another mingle rapidly on timescales of minutes (Perugini et al., 2015) while their crystal cargoes retain their identities in the form of compositional zoning. Progressive degassing, whose rate increases a few hours to days before eruption, may lead to the formation of a transient environment ME3 (Fig. 11). Such a scenario could be consistent, for example, with the record of unrest from 1251 AD – 1538 AD before the 1538 AD eruption at Campi Flegrei (Di Vito et al., 2016). Before that eruption, the system evolved over ~ 300 years and major changes occurred a couple of years before the eruption.

6 Conclusions

In this work, the complex zoning patterns shown by clinopyroxene crystals from the A-MS eruption have been characterized. Despite the complex sequential zoning testified by the wide chemical variation and the great variability of zoning types, some transitions inside the zoning pattern are prevalent suggesting a common late evolutionary history. A population-based approach allows us to identify several magmatic environments in which clinopyroxenes sequentially grew. Quantification of connectivity and their frequencies allow us to infer the pattern of magma movement among the different magmatic environments. The timescales of such movement have been constrained by diffusion modeling.

The textural features and the chemical composition of the A-MS clinopyroxenes record the existence of at least two main, likely physically separated, magmatic environments that make up the A-MS plumbing system: the first of these (ME0), identified in clinopyroxene crystals with very high Mg# (>91), is representative of mafic magma that presumably directly originated from partial melting of the local mantle source; the second, dominant magmatic environment is represented by

clinopyroxene crystals showing more evolved compositions (ME2: Mg# = 78–70) associated with trachytic and phonolitic magmas that were likely stationed in a shallower crustal reservoir. Mingling of magma from these two environments could have produced an intermediate environment (ME1; Mg#= 84–80). These magmatic environments were connected with each other with transfer of magma between them over decadal, and perhaps even centennial, timescales. More evolved environments (e.g. ME3: Mg#= 69–60) could have appeared as a result of degassing-induced crystallization shortly (e.g. days to hours) before eruption.

The proposed scenario provides guidance for evaluating future volcanic hazards. Our results suggest that mafic recharge of an evolved shallow reservoir can last for decades. During the latest phase, enhanced input of mafic magma could have destabilized the magmatic system and, combined with the associated degassing, could have favored the trigger of the eruption. In other words, input of mafic magma by itself does not trigger eruptions; eruptions are triggered only when a threshold is exceeded such that degassing and related events are set in motion. This study highlights the complex relationships between events of magma recharge/mixing and onset of the eruption. This knowledge, when integrated with information provided by other case-studies worldwide to build a behavioral model of similar active volcanoes, is useful for risk assessment.

Acknowledgments

The method for the evaluation of the effective occurrence of diffusion has been developed by Dr. Ralf Dohmen. The authors are grateful to Dr. Manuela Nazzari (INGV-Roma1) for her availability and help in the acquisition of microanalytical data. The authors gratefully acknowledge Hélène Balcone-Boissard, Teresa Ubide and an anonymous reviewer, as well as the Executive Editor of Geochimica et Cosmochimica Acta, who provided constructive suggestions and comments that substantially improved the manuscript. Aitor Cambeses acknowledges the research grant provided by the Alexander von Humboldt Foundation for a post-doctoral fellowship at Bochum. The INGV-OV laboratories have been financially supported by the EPOS Research Infrastructure through the

contribution of the Italian Ministry of University and Research (MUR). This work has been partially developed during the "Timescales of magmatic processes", a project involving collaboration between INGV (Istituto Nazionale di Geofisica e Vulcanologia), the Department of Earth, Environment and Resources Sciences of the University of Naples Federico II and the Institute of Geology, Mineralogy und Geophysics of the Ruhr-Universität (Bochum, Germany).

Funding: This work was supported by the Research Grants - Short-Term Grants, 2019 (57442045) scholarship provided by the DAAD (Deutscher Akademischer Austauschdienst) organization.

References

Acocella V., Salvini F., Funiciello R., and Faccenna C. (1999) The role of transfer structures on volcanic activity at Campi Flegrei (southern Italy). J. Volcanol. Geotherm. Res. 91, 123 – 139.

Acocella V. and Funiciello R. (2006) Transverse systems along the extensional Tyrrhenian margin of central Italy and their influence on volcanism. Tectonics. 25, 1-24. TC2003. doi:10.1029/2005TC001845

Alves A., Janasi V.D., Simonetti A. and Heaman L. (2009) Microgranitic enclaves as products of self-mixing events: a study of open-systemprocesses in the Mauà granite, São Paulo, Brazil, based on in situ isotopic and trace elements in plagioclase. J Petrol. 50, 2221-2247. doi:10.1093/petrology/egp074.

Arienzo I., Civetta L., Heumann A., Wörner G. and Orsi G. (2009) Isotopic evidence for open system processes within the Campanian Ignimbrite magma chamber. Bull. Volcanol. 71, 285–300.

878 Arienzo I. Moretti R. Civetta L. Orsi G. and Papale P. (2010) The feeding system of Agnano-
879 Monte Spina eruption (Campi Flegrei, Italy): dragging the past into the present
880 activity and future scenarios. Chem. Geol. 270, 135–147
881 Arienzo I., Neumann A., Wörner G., Civetta L. and Orsi G. (2011) Processes and timescales of
882 magma evolution prior to the Campanian ignimbrite eruption (Campi Flegrei, Italy).
883 Earth Planet. Sci. Lett. 306 (3–4), 217–228.
884 Arienzo I., Carandente A., Di Renzo V., Belviso P., Civetta L., D'Antonio M. and Orsi G.,
885 (2013) Sr and Nd isotope analysis at the Radiogenic Isotope Laboratory of the
886 Istituto Nazionale di Geofisica e Vulcanologia Sezione di Napoli - Osservatorio
887 Vesuviano. Rapporti Tecnici INGV. 260, 1–18. (available online at
888 http://istituto.ingv.it/lingv/produzionescientifica/rapporti-tecnici-
889 ingv/archivio/rapporti-tecnici-2013/).
890 Arienzo I., D'Antonio M., Di Renzo V., Tonarini S., Minolfi G., Orsi G., Carandente A., Belviso
891 P. and Civetta L. (2015) Isotopic microanalysis sheds light on the magmatic
892 endmembers feeding volcanic eruptions: the Astroni 6 case study (Campi Flegrei
893 Italy). J. Volcanol. Geotherm. Res. 304, 24–37.
894 Arienzo I., Mazzeo FC., Moretti R., Cavallo A. and D'Antonio M. (2016) Open-system magma
895 evolution and fluid transfer at Campi Flegrei caldera (Southern Italy) during the past
896 5 ka as revealed by geochemical and isotopic data. The example of the Nisida
897 eruption. Chem. Geol. 427, 109–124.
898 Arzilli F., Piochi M., Mormone A., Agostini C. and Carroll M.R. (2016) Constraining pre-
899 eruptive magma conditions and unrest timescales during the Monte Nuovo eruption
900 (1538 AD; Campi Flegrei Southern Italy): integrating textural and CSD results from
901 experimental and natural trachy-phonolites. Bull. Volcanol. 78 doi:101007/s00445-
902 016-1062-z

903 Astbury R.L., Petrelli M., Ubide T., Stock M.J., Arienzo I., D'Antonio M. and Perugini D. (2018)
904 Tracking plumbing system dynamics at the Campi Flegrei caldera Italy: high-
905 resolution trace element mapping of the Astroni crystal cargo. Lithos. 318–319, 464–
906 477.
907 Beccaluva L., Di Girolamo P. and Serri G., (1991) Petrogenesis and tectonic setting of the
908 Roman volcanic province Italy. Lithos. 26, 191–221. doi:101016/0024-
909 4937(91)90029-K
910 Belkin H.E., Rolandi G., Jackson J.C., Cannatelli C., Doherty A.L., Petrosino P. and De Vivo B.
911 (2016) Mineralogy and geochemistry of the older (> 40ka) ignimbrites on the
912 Campanian Plain, southern Italy. J. Volcanol. Geotherm. Res. 323, 1-18.
913 Bevilacqua A., Isaia R., Neri A., Vitale S., Aspinall W.P., Bisson M., Flandoli F., Baxter P.J.,
914 Bertagnini A., Esposti Ongaro T., Iannuzzi E., Pistolesi M. and Rosi M. (2015)
915 Quantifying volcanic hazard at Campi Flegrei caldera (Italy) with uncertainty
916 assessment: I Vent opening maps. J. Geophys. Res. 120, 2309– 2329.
917 doi:101002/2014JB011775
918 Bevilacqua A., Flandoli F., Neri A., Isaia R. and Vitale S. (2016) Temporal models for the
919 episodic volcanism of Campi Flegrei caldera (Italy) with uncertainty quantification.
920 J. Geophys. Res.. 121, 7821–7845. doi:101002/2016JB013171
921 Bevilacqua A., Neri A., Bisson M., Esposti Ongaro T., Flandoli F., Isaia R., Rosi M. and Vitale
922 S., (2017) The effects of vent location, event scale and time forecasts on pyroclastic
923 density current hazard maps at Campi Flegrei caldera (Italy). Front. Earth Sci. 5:72.
924 doi:103389/feart201700072
925 Blundy J. and Cashman K. (2008) Petrologic reconstruction of magmatic system variables and
926 processes. Rev. Mineral. Geochem. 69, 179–239. https://doiorg/102138/rmg2008696

927 Bonechi B., Perinelli C. and Gaeta M., (2020) Clinopyroxene growth rates at high-pressure:
928 Constraints on magma recharge of the deep reservoir of the Campi Flegrei Volcanic
929 District (south Italy). Bull. Volcanol. 82, 5. doi:10.1007/s00445-019-1342-5
930 Brocchini D., Principe C., Castratori D., Laurenzi M.A. and Gorla L. (2001) Quaternary
931 evolution of the southern sector of the Campanian Plain and early Somma-Vesuvius
932 activity: insights from Trecase 1 well. Mineral. Petrol. 73, 67–91.
933 Cannatelli C., Lima A., Bodnar R.J., De Vivo B., Webster J.D. and Fedele L. (2007).
934 Geochemistry of melt inclusions from the Fondo Riccio and Minopoli 1 eruptions at
935 Campi Flegrei (Italy). Chem. Geol. 237 (3–4), 418–432.
936 Capuano P., Russo G., Civetta L., Orsi G., D'Antonio M. and Moretti R. (2013) The active
937 portion of the Campi Flegrei caldera structure imaged by 3-D inversion of gravity
938 data. Geochem. Geophys. 14, 4681–4697. doi:101002/ggge20276
939 Cashman K.V and Giordano G. (2014) Calderas and magma reservoirs. J. Volcanol. Geotherm.
940 Res. 288, 28–45.
941 Chakraborty S. and Ganguly J. (1992) Cation diffusion in aluminosilicate garnets: experimental
942 determination in spessartine-almandine diffusion couples, evaluation of effective
943 binary diffusion coefficients, and applications. Contrib. Mineral. Petrol. 111, 74–86.
944 Chakraborty S. (2008) Diffusion in silicates: a tool to track timescales of processes comes of age
945 Ann. Rev. Earth Planet. Sci. 36, 153–190.
946 Chamberlain K.J., Morgan D.J. and Wilson C.J.N. (2014) Timescales of mixing and mobilisation
947 in the Bishop Tuff magma body: perspectives from diffusion chronometry.
948 Contrib. Mineral. Petrol. 167, 1034.
949 Chiodini G., Pappalardo L., Aiuppa A. and Caliro S. (2015) The geological CO_2 degassing
950 history of a long-lived caldera. Geology. 43, 767-770. doi:10.1130/G369051.
951 Chowdhury P. and Chakraborty S. (2019) Slow Cooling at Higher Temperatures Recorded
952 within High-P Mafic Granulites from the Southern Granulite Terrain, India:

953 Implications for the Presence and Style of Plate Tectonics near the Archean–
954 Proterozoic Boundary. J. Petrol. 60-3, 441–486, doi:10.1093/petrology/egz001
955 Civetta L., Carluccio E., Innocenti F., Sbrana A. and Taddeucci G. (1991a) Magma chamber
956 evolution at Phlegrean Fields during the last 10 ka, in the light of trace elements and
957 isotope composition. Eur. J. Mineral. 3, 415-428.
958 Cooper K.M. (2019) Time scales and temperatures of crystal storage in magma reservoirs:
959 implications for magma reservoir dynamics. Philos. Trans. Roy. Soc. 377:
960 20180009. doi:101098/rsta20180009
961 Costa F. and Chakraborty S. (2004) Decadal time gaps between mafic intrusion and silicic
962 eruption obtained from chemical zoning patterns in olivine. Earth Planet. Sci. Lett.
963 227, 517–530.
964 Costa F. Dohmen R. and Chakraborty S. (2008) Time scales of magmatic processes from
965 modeling the zoning patterns of crystals. Rev. Mineral. Geochem. 69, 545–594.
966 Crank J. (1975) The Mathematics of Diffusion, 2nd edition, 414 p. Oxford Science Publication,
967 Oxford.
968 D'Antonio M., Civetta L., Orsi G., Pappalardo L., Piochi M., Carandente A., de Vita S., Di Vito
969 M.A. and Isaia R. (1999) The present state of the magmatic system of the Campi
970 Flegrei caldera based on a reconstruction of its behavior in the past 12 ka. J.
971 Volcanol. Geotherm. Res. 91, 247–268. doi:101016/S0377-0273(99)00038-4
972 D'Antonio M., Tonarini S., Arienzo I., Civetta L. and Di Renzo V. (2007) Components and
973 processes in the magma genesis of the Phlegrean Volcanic District, southern Italy.
974 Geol. Soc. Am. 418, 203–220.
975 D'Antonio M. (2011) Lithology of the basement underlying the Campi Flegrei caldera:
976 volcanological and petrological constraints. J. Volcanol. Geotherm. Res. 200, 91–
977 98.

978 Deino A., Orsi G., de Vita S. and Piochi M. (2004) The age of the Neapolitan Yellow Tuff
979 caldera-forming eruption (Campi Flegrei caldera Italy) assessed by $^{40}Ar/^{39}Ar$ dating
980 method. J. Volcanol. Geotherm. Res. 133, 157–170.
981 Del Gaudio C, Aquino I., Ricciardi G.P., Ricco C. and Scandone R. (2010) Unrest episodes at
982 Campi Flegrei: A reconstruction of vertical ground movements during 1905–2009. J.
983 Volcanol. Geotherm. Res. 195, 48–56.
984 Dellino P., Isaia R., La Volpe L. and Orsi G. (2001) Statistical analysis of textural data from
985 complex pyroclastic sequences: implications for fragmentation processes of the
986 Agnano-Monte Spina Tephra (4.1 ka), Phlegraean Fields, southern Italy. Bull.
987 Volcanol. 63, 443–461. doi:101007/s004450100163
988 Dellino P., Isaia R., La Volpe L. and Orsi G. (2004a) Interaction between particles transported by
989 fallout and surge in the deposits of the Agnano–Monte Spina eruption (Campi
990 Flegrei Southern Italy). J. Volcanol. Geotherm. Res. 133, 193–210.
991 doi:101016/S0377-0273(03)00398-6
992 de Vita S., Orsi G., Civetta L., Carandente A., D'Antonio M., Deino A., di Cesare T., Di Vito
993 M.A., Fisher R.V., Isaia R., Marotta E., Necco A., Ort M., Pappalardo L., Piochi M.
994 and Southon J. (1999) The Agnano – Monte Spina eruption (4100 years BP) in the
995 restless Campi Flegrei caldera (Italy). J. Volcanol. Geotherm. Res. 91, 269–301.
996 Dimanov A. and Sautter V. (2000) "Average" interdiffusion of (Fe,Mn)–Mg in natural diopside.
997 Eur. J. Mineral. . 12, 749–760.
998 Di Renzo V., Arienzo I., Civetta L., D'Antonio M., Tonarini S., Di Vito M.A. and Orsi G. (2011)
999 The magmatic feeding system of the Campi Flegrei caldera: architecture and
1000 temporal evolution. Chem. Geol. 281, 227–241.
1001 Di Vito M.A., Isaia R., Orsi G., Southon J., de Vita S., D'antonio M., Pappalardo L. and Piochi
1002 M. (1999) Volcanism and deformation in the past 12 ka at the Campi Flegrei caldera
1003 (Italy). J. Volcanol. Geotherm. Res. 91, 221–246.

1004 Di Vito M.A., Acocella V., Aiello G., Barra D., Battaglia M., Carandente A., Del Gaudio C., de
1005 Vita S., Ricciardi G.P., Ricco C., Scandone R. and Terrasi F. (2016) Magma transfer
1006 at Campi Flegrei caldera (Italy) before the 1538 AD eruption. Sci. Rep. 6, 32245.
1007 Fedele L., Scarpati C., Lanphere M., Melluso L., Morra V., Perrotta A. and Ricci G. (2008) The
1008 Breccia Museo formation, Campi Flegrei southern Italy: geochronology,
1009 chemostratigraphy and relationship with the Campanian Ignimbrite eruption. Bull
1010 Volcanol. 70, 1189–1219.
1011 Fedi M., Cella F., D'Antonio M., Florio G., Paoletti V. and Morra V. (2018) Gravity modeling
1012 finds a large magma body in the deep crust below the Gulf of Naples, Italy. Sci. Rep.
1013 8, 8229. doi:10.1038/s41598-018-26346-z
1014 Forni F., Degruyter W., Bachmann O., De Astis G. and Mollo S. (2018) Long-term magmatic
1015 evolution reveals the beginning of a new caldera cycle at Campi Flegrei. Sci. Adv. 4.
1016 eaat9401. doi: 10.1126/sciadv.aat9401
1017 Gebauer S., Schmitt A.K., Pappalardo L., Stockli D.F. and Lovera O.M. (2014) Crystallization
1018 and eruption ages of Breccia Museo (Campi Flegrei caldera, Italy) plutonic clasts
1019 and their relation to the Campanian Ignimbrite. Contrib. Mineral. Petrol.
1020 doi:10.1007/s00410-013-0953- 7.
1021 Giaccio B., Hajdas I., Isaia R., Deino A. and Nomade S. (2017) High-precision ^{14}C and $^{40}Ar/^{39}Ar$
1022 dating of the Campanian Ignimbrite (Y-5) reconciles the time-scales of climatic-
1023 cultural processes at 40 ka. Sci. Rep. 7:45940. doi: 101038/srep45940
1024 Goldstein S.L, Deines P., Oelkers E.H, Rudnick R.L. and Walter L.M. (2003) Standards for
1025 publication of isotope ratio and chemical data in Chemical Geology. Chem. Geol.
1026 202, 1-4.
1027 Grove T.L. and Bryan W.B. (1983) Fractionation of pyroxene-phyric MORB at low pressure:
1028 and experimental study. Contrib. Mineral. Petrol. 84, 293-209.

1029 Guidoboni E. and Ciuccarelli C. (2011) The Campi Flegrei caldera: historical revision and new
1030 data on seismic crises, bradyseisms, the Monte Nuovo eruption and ensuing
1031 earthquakes (twelfth century 1582 ad). Bull. Volcanol. 73, 655–677.
1032 Humphreys M.C.S., Blundy J.D. and Sparks R.S.J. (2006) Magma evolution and open-system
1033 processes at Shiveluch volcano: insights from phenocryst zoning. J. Petrol. 47,
1034 2303–2334.
1035 Iovine R.S, Fedele L., Mazzeo F.C., Arienzo I., Cavallo A., Wörner G., Orsi G., Civetta L. and
1036 D'Antonio M. (2017a) Timescales of magmatic processes occurred prior to the ~4.7
1037 ka Agnano-Monte Spina eruption (Campi Flegrei caldera Southern Italy) based on
1038 diffusion chronometry on sanidine phenocrysts. Bull. Volcanol. 79,18.
1039 doi:101007/s00445-017-1101-4
1040 Isaia R., D'Antonio M., Dell'Erba F., Di Vito M. and Orsi G. (2004) The Astroni volcano: the
1041 only example of closely spaced eruptions in the same vent area during the recent
1042 history of Campi Flegrei caldera (Italy). J. Volcanol. Geotherm. Res. 133, 171–192.
1043 doi:10.1016/S0377-0273(03)00397-4
1044 Isaia R., Marianelli P. and Sbrana A. (2009) Caldera unrest prior to intense volcanism in Campi
1045 Flegrei (Italy) at 4.0 ka B.P.: implications for caldera dynamics and future eruptive
1046 scenarios. Geophys. Res. Lett. 36:L21303. doi:10.1029/2009GL040513
1047 Jagoutz E., Palme H., Baddenhausen H., Blum K., Cendales M., Dreibus G., Spettel B., Lorentz
1048 V. and Wllnke H., (1979) The abundances of major, minor and trace elements in the
1049 Earth's mantle as derived from primitive ultramafic nodules. Proceedings of the 10th
1050 Lunar and Planetary Science Conference. Geochim. Cosmochim. Acta. Supp. I. 11,
1051 2031-2050.
1052 Jarosewich E., Nelen J.A. and Norberg J.A. (1980) Reference samples for electron microprobe
1053 analysis. Geostandards Newsletter. 4, 43-47. https://doi.org/10.1111/j.1751-
1054 908X.1980.tb00273.x

1055 Kahl M., Chakraborty S., Costa F. and Pompilio M. (2011) Dynamic plumbing system beneath
1056 volcanoes revealed by kinetic modeling and the connection to monitoring data: an
1057 example from Mt Etna. Earth Planet. Sci. Lett. 308, 11–22.
1058 Kahl M., Chakraborty S., Costa F., Pompilio M., Liuzzo M. and Viccaro M. (2013)
1059 Compositionally zoned crystals and realtime degassing data reveal changes in
1060 magma transfer dynamics during the 2006 summit eruptive episodes of Mt. Etna.
1061 Bull. Volcanol. 75, 692. doi:10.1007/s00445-013-0692-7
1062 Kahl M., Chakraborty S., Pompolio M. and Costa F. (2015) Constraints on the nature and
1063 evolution of the magma plumbing system of Mt Etna volcano (1991–2008) from a
1064 combined thermodynamic and kinetic modeling of the compositional record of
1065 minerals. J. Petrol. 56, 2025–2068.
1066 Kahl M., Viccaro M., Ubide T., Morgan D.J. and Dingwell D.B. (2017) A branched magma
1067 feeder system during the 1669 eruption of Mt Etna: evidence from a time-integrated
1068 study of zoned olivine phenocryst populations. J. Petrol. 58, 443–472.
1069 Liedl A., Buono G., Lanzafame G., Dabagov S.B., Della Ventura G., Hampai D., Mancini L.,
1070 Marcelli A. and Pappalardo L. (2019) 3D imaging textural characterization of
1071 pyroclastic products from the 1538 AD Monte Nuovo eruption (Campi Flegrei,
1072 Italy). Lithos. 340–34.: 316-331. doi:10.1016/j.lithos.2019.05.010.
1073 Lustrino M., Marturano A., Morra V. and Ricci G. (2002) Volcanological and geochemical
1074 features of young pyroclstic levels (b12 ka) in the urban area of Naples (S Italy).
1075 Period. di Mineral. 71(3), 241–253.
1076 Mangiacapra A., Moretti R., Rutherford M., Civetta L., Orsi G. and Papale P. (2008) The deep
1077 magmatic system of the Campi Flegrei caldera (Italy). Geophys. Res. Lett. 35,
1078 L21304. doi:101029/2008GL035550

1079 Mangler M.F., Petrone C.M., Hill S., Delgado-Granados H. and Prytulak J. (2020) A pyroxenic
1080 view on magma hybridization and crystallization at Popocatepetl Volcano, Mexico.
1081 Front. Earth Sci. 8, 362. doi:10.3389/feart.2020.00362
1082 Marianelli P., Sbrana A. and Proto M. (2006) Magma chamber of the Campi Flegrei
1083 supervolcano at the time of eruption of the Campanian Ignimbrite. Geology. 34(11),
1084 937– 940. doi: 10.1130/G22807A.1
1085 Masotta M., Mollo S., Freda C., Gaeta M. and Moore G. (2013) Clinopyroxene–liquid
1086 thermometers and barometers specificto alkaline differentiated magmas. Contrib.
1087 Mineral. Petrol. 166, 1545–1561. doi:101007/s00410-013-0927-9
1088 Mastrolorenzo G. and Pappalardo L. (2006) Magma degassing and crystallization processes
1089 during eruptions of high-risk Neapolitan volcanoes. Evidence of common
1090 equilibrium rising processes in alkaline magmas. Earth Planet. Sci. Lett. 250, 164–
1091 181.
1092 Mastrolorenzo G., Palladino D.M., Pappalardo L. and Rossano S. (2017) Probabilistic-Numerical
1093 assessment of pyroclastic current hazard at Campi Flegrei and Naples city: Multi-
1094 VEI scenarios as a tool for “full-scale” risk management. PLoS One.
1095 doi.org/10.1371/journal.pone.0185756
1096 Mazzeo F.C., D'Antonio M., Arienzo I., Aulinas M., Di Renzo V. and Gimeno D. (2014)
1097 Subduction-related enrichment of the Neapolitan volcanoes (Southern Italy) mantle
1098 source: new constraints on the characteristics of the slab-derived components. Chem.
1099 Geol. 386, 165-183.
1100 Mele D., Dioguardi F., Dellino P., Isaia R., Sulpizio R. and Braia G. (2015) Hazard of
1101 pyroclastic density currents at the Campi Flegrei Caldera (Southern Italy) as deduced
1102 from the combined use of facies architecture physical modelingand statistics of the
1103 impact parameters. J. Volcanol. Geotherm. Res. 299, 35–53.
1104 doi:101016/jjvolgeores201504002

1105 Melluso L., de'Gennaro R., Fedele L., Franciosi L. and Morra V. (2012) Evidence of
1106 crystallization in residual, Cl–F-rich, agpaitic, trachyphonolitic magmas and
1107 primitive Mg-rich basalt–trachyphonolite interaction, in the lava domes of the
1108 Phlegrean Fields (Italy). Geol. Mag. 149, 532–550.
1109 Mollo S., Del Gaudio P., Ventura G., Iezzi G. and Scarlato P, (2010) Dependence of
1110 clinopyroxene composition on cooling rate in basaltic magmas: implications for
1111 thermobarometry. Lithos. 118, 302–312.
1112 Mollo S., Putirka K., Misiti V., Soligo M. and Scarlato P. (2013) A new test for equilibrium
1113 based on clinopyroxene-melt pairs: clues on the solidification temperatures of Etnean
1114 alkaline melts at post-eruptive conditions. Chem. Geol. 352, 92–100. https
1115 ://doi.org/10.1016/j.chemg eo.2013.05.026.
1116 Montagna C.P., Papale P. and Longo A. (2015) Timescales of mingling in shallow magmatic
1117 reservoirs. Geol. Soc. Spec. Publ. 422, 131-140. doi:10.1144/SP422.6.
1118 Morabito S., Petrosino P., Milia A., Sprovieri M. and Tamburrino S. (2014) A multidisciplinary
1119 approach for reconstructing the stratigraphic framework of the last 40 ka in a bathyal
1120 area of the eastern Tyrrhenian Sea. Glob. Planet. Change. 123, 121-138.
1121 Moretti R., Arienzo I., Orsi G., Civetta L. and D'Antonio M. (2013) The deep plumbing system
1122 of Ischia: a physico-chemical window on the fluid-saturated and CO_2-sustained
1123 Neapolitan volcanism (southern Italy). J. Petrol. 54, 951-984.
1124 Moretti R., Arienzo I., Civetta L., Orsi G. and Papale P. (2013) Multiple magma degassing
1125 sources at an explosive volcano. Earth Planet. Sci. Lett. 367, 95-104.
1126 doi:10.1016/j.epsl.2013.02.013; ISSN: 0012-821X
1127 Moretti R., Troise C., Sarno F. and De Natale G. (2018) Caldera unrest driven by CO2-induced
1128 drying of the deep hydrothermal system. Sci. Rep. 8 (1), 8309.
1129 Moretti R., Arienzo I., Di Renzo V., Orsi G., Arzilli F., Brune F., D'Antonio M., Mancini L. and
1130 Deloule E. (2019) Volatile segregation and generation of highly vesiculated

explosive magmas by volatile-melt fining processes: The case of the Campanian Ignimbrite eruption. Chem. Geol. 503, 1-14.

Morgan D.J., Blake S., Rogers N.W., De Vivo B., Rolandi G., Macdonald R. and Hawkesworth J. (2004) Timescales of crystal residence and magma chamber volume from modelingof diffusion profiles in phenocrysts: Vesuvius 1944. Earth Planet. Sci. Lett. 222, 933–946.

Müller T., Dohmen R., Becker H.W., ter Heege J. and Chakraborty S. (2013) Fe–Mg interdiffusion rates in clinopyroxene: experimental data and implications for Fe–Mg exchange geothermometers. Contrib. Mineral. Petrol. 166,1563–1576.

Munno R. and Petrosino P. (2004) New constraints on the occurrence of Y-3 upper Pleistocene tephra marker layer in the tyrrhenian sea. Il Quaternario, Italian Journal of Quaternary Sciences. 17, 11-20

Nimis P. (1995) A clinopyroxene geobarometer for basaltic systems based on crystal-structure modeling. Contrib. Mineral. Petrol. 121, 115-125.

Orsi G., de Vita S. and Di Vito M.A. (1996) The restless, resurgent Campi Flegrei nested caldera (Italy): constraints on its evolution and configuration. J. Volcanol. Geotherm. Res. 74, 179-214.

Orsi G., de Vita S., Di Vito M., Isaia R., Nave R. and Heiken G. (2003) Facing volcanic and related hazards in the Neapolitan Area. In: Heiken, G., Fakundiny, R. & Sutter, J. (eds). Earth Science in the Cities: a Reader. Washington, DC. AGU, 121-170.

Orsi G., Di Vito M.A. and Isaia R. (2004) Volcanic hazard assessment at the restless Campi Flegrei caldera. Bull. Volcanol. 66, 514–530.

Orsi G., Di Vito M.A., Selva J. and Marzocchi W. (2009) Long-term forecast of eruption style and size at Campi Flegrei caldera (Italy). Earth Planet. Sci. Lett.. 287, 265–276.

Pappalardo L., Civetta L., D'Antonio M., Deino A., Di Vito M., Orsi G., Carandente A., de Vita S., Isaia R. and Piochi M. (1999) Chemical and Sr- isotopical evolution of the

1157 Phlegrean magmatic system before the Campanian Ignimbrite and the Neapolitan
1158 Yellow Tuff eruptions. J. Volcanol. Geotherm. Res. 91, 141-166.
1159 Pappalardo L., Piochi M., D'Antonio M., Civetta L. and Petrini R. (2002) Evidence for
1160 multistage magmatic evolution during the past 60 kyr at Campi Flegrei (Italy)
1161 deduced from Sr, Nd and Pb isotope data. J. Petrol. 43, 1415-1434.
1162 Pappalardo L., Ottolini L. and Mastrolorenzo G. (2008) The Campanian Ignimbrite (Southern
1163 Italy) geochemical zoning, insight on the generation of a super-eruption from
1164 catastrophic differentiation and fast withdrawal. Contrib. Mineral. Petrol. 156, 1–26.
1165 Pappalardo L. and Mastrolorenzo G. (2012) Rapid differentiation in a sill-like magma reservoir:
1166 a case study from the campi flegrei caldera. Sci. Rep. 2:712. doi:101038/srep00712
1167 Pappalardo L. and Buono G. (2021) Insights into processes and timescales of magma storage and
1168 ascent from textural and geochemical investigations, in: Masotta, M., Beier, C.,
1169 Mollo, S. (Eds.), Crustal Magmatic System Evolution. AGU (American Geophysical
1170 Union) Monograph. 213-235. https://doi.org/10.1002/9781119564485.ch10.
1171 Perinelli C., Gaeta M., Bonechi B., Granati S.F., Freda C., D'Antonio M., Stagno V., Sicola S.
1172 and Romano C. (2019) Effect of water on the phase relations of primitive K-basalts:
1173 Implications for high-pressure differentiation in the Phlegraean Volcanic District
1174 magmatic system. Lithos .342, 530–541.
1175 Perugini D., De Campos C.P., Petrelli M. and Dingwell D.B. (2015) Concentration variance
1176 decay during magma mixing: a volcanic chronometer, Sci. Rep 5, 14225.
1177 doi:101038/srep14225
1178 Petrone C., Bugatti G., Braschi E. and Tommasini S.. (2016) Pre-eruptive magmatic processes
1179 re-timed using a non-isothermal approach to magma chamber dynamics. Nature
1180 Communication. 7, 12946. doi:10.1038/ncomms12946
1181 Piochi M., Bruno P.P. and De Astis G. (2005) Relative roles of rifting tectonics and magma
1182 ascent processes: inferences from geophysical, structural, volcanological, and

geochemical data for the Neapolitan volcanic region (southern Italy). Geochem. Geophys. 6, Q07005 doi:10,1029/2004GC000885

Putirka K., Ryerson F.J. and Mikaelian H. (2003) New igneous thermobarometers for mafic and evolved lava compositions, based on clinopyroxene+liquid equilibria. Am. Min. 88, 1542–1554.

Putirka K.D. (2008) Thermometers and barometers for volcanic systems. Rev. Mineral. Geochem. 69, 61–120.

Roach A.L. (2005) The Evolution of Silicic Magmatism in the Post-Caldera Volcanism of the Phlegrean Fields, Italy. PhD thesis. Brown University, Providence, USA.

Romano C., Vona A., Campagnola S., Giordano G., Arienzo I. and Isaia R. (2020) Modeling and physico-chemical constraints to the 4.5 ka Agnano-Monte Spina Plinian eruption (Campi Flegrei, Italy). Chem. Geol. 532. 119301.

Saunders K., Blundy J., Dohmen R. and Cashman K. (2012) Linking petrology and seismology at an active volcano. Science. 336, 1023–1027.

Sautter V., Jaoul O. and Abel F. (1988) Aluminum diffusion in diopside using the ^{27}Al (p, γ) ^{28}Si nuclear reaction: preliminary results. Earth Planet. Sci. Lett. 89, 109-114.

Scarpati C., Perrotta A., Lepore S. and Calvert A. (2013) Eruptive history of Neapolitan Volcanoes: Constrains from ^{40}Ar-^{39}Ar dating. Geol. Mag. 150(3), 412–425.

Selva J., Orsi G., Di Vito M.A., Marzocchi W. and Sandri L. (2012) Probability hazard map for future vent opening at the Campi Flegrei caldera (Italy), Bull Volcanol. 74, 497–510.

Smith V.C., Isaia R. and Pearce N.J.G. (2011) Tephrostratigraphy and glass compositions of post-15 ka Campi Flegrei eruptions: implications for eruption history and chronostratigraphic markers. Quat. Sci. Rev. 30, 3638–3660. doi:101016/jquascirev201107012.

Solaro C., Balcone-Boissard H., Morgan D.J., Boudon G., Martel C. and Ostorero L. (2020) A system dynamics approach to understanding the deep magma plumbing system

beneath Dominica (Lesser Antilles). Front. Earth Sci. 8:574032. doi: 10.3389/feart.2020.574032

Sparks R.S.J. and Cashman K.V. (2017) Dynamic magma systems: implications for forecasting volcanic activity. Elements. 13, 35–40. doi: 10.2113/gselements.13.1.35.

Tonarini S., Leeman W.P., Civetta L., D'Antonio M., Ferrara G. and Necco A. (2004) B/Nb and $\delta^{11}B$ systematics in the Phlegrean Volcanic District, Italy. J. Volcanol. Geotherm. Res. 133, 123–139.

Trepmann C.A., Stöckhert B. and Chakraborty S. (2004) Oligocene trondhjemitic dikes in the Austroalpine basement of the Pfunderer Berge Südtirol – level of emplacement and metamorphic overprint. Eur. J. Mineral. 16, 641–659. doi:101127/0935-1221/2004/0016-0641

Turner S. and Costa F. (2007) Measuring timescales of magmatic evolution. Elements. 3, 267-272.

Ubide T., McKenna C.A., Chew D.M. and Kamber B.S. (2015) High-resolution LA-ICP-MS trace element mapping of igneous minerals: in search of magma histories. Chem. Geol. 409, 157–168. doi:101016/jchemgeo201505020

Ubide T. and Kamber B. (2018) Volcanic crystals as time capsules of eruption history. Nat. Commun. 9, 326–326. doi:101038/s41467-017-02274-w.

Ubide T., Mollo S., Zhao J.X., Nazzari M. and Scarlato P. (2019) Sector zoned clinopyroxene as a recorder of magma history, eruption triggers, and ascent rates. eochim. Cosmochim. Acta. 251, 265–283. doi:101016/jgca201902021.

Voloschina M., Pistolesi M., Bertagnini A., Métrich N., Pompilio M, Di Roberto A., Di Salvo S., Francalanci L., Isaia R., Cioni R. and Romano C. (2018) Magmatic reactivation of the Campi Flegrei volcanic system: insights from the Baia–Fondi di Baia eruption. Bull. Volcanol. 80, 75. doi:10.1007/s00445-018-1247-8

Wu Wan N., Schmitt Axel K. and Pappalardo L., (2015) U-Th baddeleyite geochronology and its significance to date the emplacement of silica undersaturated magmas. Am. Mineral. 100, 2082–2090.

Zdanowicz G., Boudon G., Balcone-Boissard H., Cioni R., Mundula F., Orsi G., and Civetta L. (2016) The sub-Plinian Greenish Pumice eruption (19,065±105 yr cal BP) of Mount Somma – Vesuvius. Geochemical and textural constrains., EGU General Assembly 2016, 17 April–22 Apr 2016, EGU2016-6940, 2016

Zellmer G.F., Blake S., Vance D., Hawkesworth C. and Turner S., (1999) Plagioclase residence times at two island arc volcanoes (Kameni Islands, Santorini and Soufriere St Vincent) determined by Sr diffusion systematic. Contrib. Mineral. Petrol. 136, 345–357.

Zellmer G.F., Sparks R.S.J, Hawkesworth C. and Wiedenbeck M. (2003) Magma emplacement and remobilization timescales beneath Montserrat: insights from Sr and Ba zonation in plagioclase phenocrysts. J. Petrol. 44, 1413-1431.

Zollo A., Maercklin N., Vassallo M., Dello Iacono D., Virieux J. and Gasparini P. (2008) Seismic reflections reveal a massive melt layer feeding Campi Flegrei caldera. Geophys. Res. Lett. 35, L12306. doi:10.1029/2008GL034242

Figures

Fig. 1 a) Geological and structural sketch map of the Southern Campania Plain (modified after Orsi et al., 2003). b) Areal distribution of the A-MS volcanic deposits (redrawn after de Vita et al., 1999. c) Detail of the Agnano-San Vito area (modified after Iovine et al., 2017a) d) Schematic stratigraphic column of the A-MS erupted products, subdivided into various members (modified after Iovine et al., 2017a).; in brackets we reported the number of samples collected from each sub-member.

Fig. 2 a) Glass compositions of A-MS products plotted in the Total Alkali vs. Silica diagram; melt inclusion data are from Arienzo et al. (2010); whole rock and matrix-glass compositions are from de Vita et al. (1999). b) Di-Hd-En-Fs classification diagram of clinopyroxenes found in A1, B1 and D1 members of the A-MS deposits; literature data refer to clinopyroxene from A-MS products (de Vita et al., 1999; Arienzo et al., 2010); mantle refers to the zones/sectors of the crystals between the core and the most external rim.

Fig. 3 a) Mg#, b) Na_2O and c) Al_2O_3 frequency histograms of core, mantle and rim of the zoned A-MS clinopyroxenes. These allow different populations to be identified. d) Al_2O_3 vs Mg# and e) TiO_2 vs Mg# variation diagrams of the analyzed zoned A-MS clinopyroxenes showing a wide compositional range and different populations and sub-populations. Note that all clinopyroxenes of different compositions lie on a trend defined by the orange arrow, with the exception of the ME1b and ME2b trends, which are shown in yellow. The significance of these trends is discussed in section 4.6.

Fig. 4 The colored table reports, for each sub-member, the frequency of occurrence of a compositional population in a zoning sector (core, mantle or rim) in a total of 36 (out of 41) analyzed clinopyroxene crystals of the A-MS deposit; c=core; m=mantle; r=rim. Percentages have been calculated considering clinopyroxenes with plateaus (36 out of 41). Percentage of compositional populations occurring in the homogeneous clinopyroxene crystals is also reported. % tot.in rows at the bottom express the abundance of a compositional population in all the analyzed crystals (36 for the zoned and 46 for the unzoned crystals, respectively).

Fig. 5 Types of zonation of the A-MS clinopyroxenes. Black diamonds are measured analysis along the crystal traverses showing concentration profiles from core to rim [Mg# = molar $Mg^{2+}/(Mg^{2+}+Fe_{tot})$]. In the BSE images, the blue lines are the traverses along which the chemical composition has been acquired. Black dashed lines indicate the initial profile shapes: these are different depending on the two methods applied for diffusion modeling and have been inferred through the relationships between Al_2O_3 (wt%) and Mg# in the profiles Red lines indicate modelled profiles. A complete description of the diffusion modeling methods is provided in section 4.6. The numbers in brackets indicate the percentage of zoned clinopyroxenes exhibiting such a pattern.

Fig. 6 Stratigraphic height vs Sr-isotopic composition of A-MS whole rocks and minerals. Literature data are from de Vita et al. (1999) and Arienzo et al. (2010).

Fig. 7 a) Fe-Mg partitioning between clinopyroxene and host rock ($^{Fe/Mg}Kd_{Cpx\text{-}liq} = 0.27\pm0.03$; Grove and Bryan, 1983; Putirka et al., 2003); fields demarcated by colored dotted lines represent the whole set of A-MS clinopyroxenes, belonging to different magmatic environments, compared to host rocks; the transparent colored dotted lines refer to clinopyroxenes with high Mg# (ME0 and ME1) compared to A-MS whole rocks and matrix glass compositions: these clinopyroxenes are out of equilibrium with respect to their host rocks; some of these clinopyroxenes are in equilibrium with more mafic rocks; diamond symbols refers to some clinopyroxenes which passed the compositional test for equilibrium and have been used for geothermobarometry. b) Output pressures and temperatures estimates for the different magmatic environments of the A-MS clinopyroxenes obtained by the clinopyroxene-liquid thermometers (equation Talk2012) and barometers (equation Palk2012) specific for alkaline magmas (Masotta et al., 2013); error bars refer to SEE.

Fig. 8 Systems connectivity diagrams of the zoning patterns of A-MS clinopyroxene crystals. Since each compositional population can be associated to a specific magmatic environment (see section 3.2), the different magmatic environments are characterized by different ranges in the Mg#. Different zoning types are depicted by different connection lines represented by different color (e.g. the orange routes represent clinopyroxene crystals with core formed in ME2, mantle formed in ME0 and the rim formed in ME2). The height of the boxes is proportional to the frequency of occurrence of the magmatic environments. The A-MS clinopyroxene zoning patter is characterized by most of the connection lines linking ME0 and ME2, also passing through ME1, and a few connections linking ME2 and ME3.

Fig. 9 a,c) Mg# vs Al_2O_3 (wt%) relations of two selected crystal profiles. b,d) measured and inferred initial Mg# profiles. In Fig. 9a, the profile show a good correlation (R^2=0.94; black trend-line) between Mg# and Al_2O_3 (wt%). In Fig. 9b, the inferred initial profile is calculated based on the relations assessed by best fit of the linear trend-line of Fig. 8a. In Fig. 9c, the profile does not show a good correlation (R^2=0.74; black trend-line) between Mg# and Al_2O_3 (wt%). By taking into account the Mg# and Al_2O_3 (wt%) contents of the two plateaus (without the points in the boundary region between the plateaus), a new best fit (R^2=1; blue trend-line) has been estimated. In Fig. 9d, the inferred initial profile is calculated based on the best fit shown by the blue trend-line. Since Mg# And Al_2O_3 are correlated, the inferred profiles (blue diamonds in Fig. 9b,d) can be taken as growth profiles. Such an analysis implies that crystal profiles showing a good match between measured and inferred profiles (e.g. Fig. 9b) have been little, or not at all, affected by diffusion. On the other hand, crystal profiles showing differences between measured and inferred profiles (e.g. Fig. 9d) have been affected by diffusion.

Fig. 10 Output values of times obtained by diffusion modeling on 50 out of 82 analyzed profiles on clinopyroxene crystals. Method I yields the upper limits of residence times of crystals in a magmatic environment; method II yields the residence times of crystals in a magmatic environment.

Fig. 11 Schematic sketch illustrating the magmatic processes occurred in the A-MS plumbing system. a) three distinct magmatic environments at a t = 0: one (ME0), in red, in which core of clinopyroxenes with high Mg# (92–85) were formed, is associated with primitive magmas; an environment (ME2), in yellow, ascribable to a crustal reservoir of the Phlegraean magmatic system, in which core of clinopyroxenes with Mg#78–70 were formed and an environment (ME3), in blue, identifiable with a less abundant, most differentiated magma portion of the ME2 reservoir. b) The interaction between ME0 and ME2 explains the normal zoning for clinopyroxenes of ME0 and, conversely, the reverse zoning for clinopyroxenes of ME2, also leading to the formation of intermediate compositions (ME1). c) The interaction between ME2 and ME3 justifies the whole set of observed zoning patterns in the A-MS clinopyroxene; t_2-t_1 represents the time span of the mixing events recorded by crystals modeled through method II; t_1-t_0 represents the time span of the recharge events possibly due to increase of mafic magma input recorded by crystals modeled through method I; t_0= time of the eruption.

Fig. 1 in Supplementary Material 1 - Photomicrographs and BSE images of A-MS rocks showing the main textural and mineralogical features. a) microphotograph of a A-MS pumice from B1 sub-member showing a sanidine phenocryst; b) microphotograph showing a plagioclase and clinopyroxene aggregate in a pumice clast from the A1 sub-member; c) microphotograph showing phlogopite crystals in a pumice clast from the B2 sub-member; d) microphotograph showing clinopyroxene and opaque oxide crystals in a pumice clast from the A2 sub-member; e) microphotograph showing apatite crystals in the matrix-glass and in clinopyroxene of a pumice

clast from the D2 sub-member; f) BSE image of a pumiceous clast from D1 sub-member showing the network of vesicles. Abbreviations: cpx = clinopyroxene; pl = plagioclase; san =sanidine; phl = phlogopite; ap = apatite; ox = opaque oxide

Fig. 2 in Supplementary Material 1 Matrix-glass major and minor element variation diagrams of A-MS rocks; literature data on A-MS matrix-glasses and whole rocks composition are from de Vita et al. (1999).

Insights into the temporal evolution of magma plumbing systems from compositional zoning in clinopyroxene crystals: a case study from the Agnano-Monte Spina Plinian eruption (Campi Flegrei, Italy)

Pelullo C.[1,3], Chakraborty S.[2], Cambeses A.[2], Dohmen R.[2], Arienzo I.[3], D'Antonio M.[1], Pappalardo L.[3], Petrosino P.[1]

[1]*Università di Napoli Federico II, Dipartimento di Scienze della Terra, dell'Ambiente e delle Risorse, Cupa Nuova Cintia, 21 - 80126 – Napoli, Italy*

[2]*Institut für Geologie, Mineralogie und Geophysik, Ruhr Universität, Universitätsstraße 150 - 44801, Bochum, Germany*

[3]*Istituto Nazionale di Geofisica e Vulcanologia, Sezione di Napoli Osservatorio Vesuviano, Via Diocleziano, 328 - 80124, Napoli, Italy*

* Corresponding author: carlo.pelullo@unina.it

Abstract

The complex sequential compositional zoning of clinopyroxene crystals erupted < 5ka during the Agnano-Monte Spina (A-MS) eruption, which is considered to be the reference event for a future large-scale explosive eruption at Campi Flegrei caldera (Italy), has been characterized in detail. Concentration profiles (20–800 μm long, spacing 2.5–10μm) of major (Si, Ti, Al, Fe, Mg and Ca) and minor (Mn, Na, Ni and Cr) elements were measured along different directions in the clinopyroxene crystals. The zoning patterns of Fe–Mg and selected elements (e.g. Al, Ti) often consist of two or more compositional plateaus with both sharp and/or slightly diffuse boundaries between the plateaus. Each compositional population results from a growth stage in a distinct Magmatic Environment (ME), which is identified as a defined set of intensive thermodynamic variables (pressure, temperature, bulk composition and fugacity of fluids including oxygen). The large range of chemical compositions of clinopyroxenes reveals the existence of at least four MEs that are characterized by different compositional populations; two of these are dominant. The variation in zoning pattern from one plateau composition to another fingerprints the transfer of the crystal from one ME to another. In combination with Sr isotopic data and thermobarometric estimates, our systematic characterization of clinopyroxene zoning patterns suggests recharge by deep mafic magmas (ME0: Mg#=92–85) of an evolved shallow reservoir (ME2: Mg#=78–70). Such a process also led to the formation of a compositionally intermediate environment (ME1: Mg#=84–80), that is detected in the clinopyroxene zoning pattern.

A new method has been developed in this work to evaluate the effective diffusive modifications that affect the concentration profiles of zoned crystals. The application of different diffusion modeling methods indicates that deep and shallow reservoirs beneath the Campi Flegrei caldera were connected to each other over several tens of years until the amount of mafic recharge increased during the last 10–15 years before the A-MS eruption. This study highlights the complex relationships between events of magma recharge and the onset of eruption. Our results provide a

contribution to the knowledge of timescales of magmatic processes that have recently occurred beneath the Campi Flegrei caldera, which is useful for risk assessment.

Key words

Clinopyroxene zoning patterns – Plumbing system – Campi Flegrei caldera – Magma mixing – Diffusion chronometry

1 Introduction

Volcanic eruptions are triggered by magmatic processes that occur in subvolcanic plumbing systems and so a better understanding of magma evolution rates and processes has implications for volcanic hazard forecasting (Blundy and Cashman, 2008; Saunders et al., 2012; Kahl et al., 2013; Cashman and Giordano, 2014; Petrone et al., 2016; Sparks and Cashman, 2017; Cooper, 2019). High-precision, high spatial resolution analysis of major and trace elements of chemically zoned minerals represents a powerful tool for investigating nature and rates of the magma chamber processes that preceded explosive eruptions of variable energy. Since mineral compositions in a magma depend on crystallization conditions, crystals preserve evidence of parameters (e.g. pressure, temperature, oxygen fugacity and volatile content) that characterize the environments where they were formed.

Compositional data on various portions of chemically heterogeneous minerals have provided information both on pre-eruptive processes such as magma ascent, recharge of a reservoir, differentiation and mingling/mixing as well as their timescales (e.g. Zellmer et al., 1999, 2003; Costa and Chakraborty, 2004; Humphreys et al., 2006; Turner and Costa, 2007; Alves et al., 2009; Kahl et al., 2011, 2013, 2015, 2017; Chamberlain et al., 2014; Ubide et al., 2015, 2019; Ubide and Kamber, 2018; Astbury et al., 2018, Cooper, 2019).

In spite of this large body of work, diffusion modeling of volcanic clinopyroxene crystals using compositional profiles measured through microanalysis and recently obtained experimental diffusion coefficient data (e.g. Müller et al., 2013) are rare, exceptions being the recent study of Mangler et al. (2020) or that of Chowdhury and Chakraborty (2019) on metamorphic clinopyroxenes. One earlier study used BSE contrast imaging and older diffusion data to obtain timescales of magmatic processes that preceded the 1944 AD eruption of the nearby Vesuvius volcanic complex (Morgan et al., 2004).

In this paper we develop a tool to use compositional zoning in clinopyroxene crystals to infer the nature and timescales of magmatic processes in volcanic plumbing systems. To develop the tool, we use detailed chemical characterization of clinopyroxene crystals from the products of Agnano-Monte Spina (A-MS), a Plinian eruption that occurred at Campi Flegrei caldera at 2604–2461 BCE (Smith et al., 2011). For a dormant, though active and restless volcano, an estimate of the time required for magma to become eruptible, either by coalescence of separate shallow batches or by deeper magma recharge, is of paramount importance. The expected resumption of explosive activity and the high population density in the region makes the Campi Flegrei caldera one of the most hazardous and vulnerable volcanic areas on Earth (Orsi et al., 2004, 2009; Bevilacqua et al., 2015; Mastrolorenzo et al., 2017). These aspects, combined with the fact that a variety of clinopyroxene compositional patterns are found in the rocks, make the A-MS eruption an ideal target for developing the tool. Moreover, there have already been several attempts at assessing timescales of pre-eruptive processes for Campi Flegrei volcanic activity using different approaches. Estimates of timescales of magma differentiation, transfer, recharge, accumulation and mixing have been obtained through isotope analyses (e.g. Arienzo et al., 2011), zircon geochronology (e.g. Gebauer et al., 2014; Wu et al., 2015), diffusion chronometry (e.g. Iovine et al., 2017a) and experimental petrology (e.g. Perugini et al., 2015). Timescale information based on textural analysis (e.g. Crystal Size Distribution – CSD; Piochi et al., 2005; Mastrolorenzo and Pappalardo, 2006; Pappalardo and Mastrolorenzo, 2012; Arzilli et al., 2016), historical, archaeological, geological and long-term geodetic record (e.g. Di Vito et al., 2016 and reference therein), numerical simulations (e.g. Montagna et al., 2015) and crystals growth rates (e.g. Astbury et al., 2018) has also been acquired. All of these provide a framework within which to evaluate the results of the current study.

We have carried out quantitative analyses along core to rim transects of clinopyroxene crystals belonging to different eruptive units of the A-MS deposits. The zoning patterns in the crystals are characterized by zones with constant compositions that have been interpreted to represent changes in magmatic environments in which the crystals resided (Kahl et al., 2013, 2015, 2017; Solaro et al.,

2020). After systematizing the connectivity between different magmatic environments, we have attempted to reconstruct the pre-eruptive processes, and then applied the newly developed diffusion modeling tools to constrain the timescales of these processes.

2 Volcanological and petrological background

2.1 The Campi Flegrei caldera

The volcanic history of the Campi Flegrei caldera (CFc) has been extensively investigated in the past decades (e.g. Orsi et al., 1996; Di Vito et al., 1999, 2016; Isaia et al., 2004, 2009; Scarpati et al., 2013). Continental Campi Flegrei together with the islands of Ischia and Procida, constitute the Phlegraean Volcanic District (PVD; Fig. 1a-b; Orsi et al., 1996). The PVD formed in response to the Pliocene-Quaternary extensional processes that generated the Campania Plain graben, along the Tyrrhenian margin of the Apennine thrust belt (Fig. 1a; Acocella and Funiciello, 2006). The NW–SE normal and NE–SW normal to strike-slip transfer fault systems separated the graben into blocks and allowed magmas to rise to the surface (Acocella et al., 1999; Brocchini et al., 2001; Piochi et al., 2005; Acocella and Funiciello, 2006 and reference therein). Except for Procida, whose activity ended *c.* 22 ka (Morabito et al., 2014), Ischia island and CFc are still active and pose a high volcanic hazard.

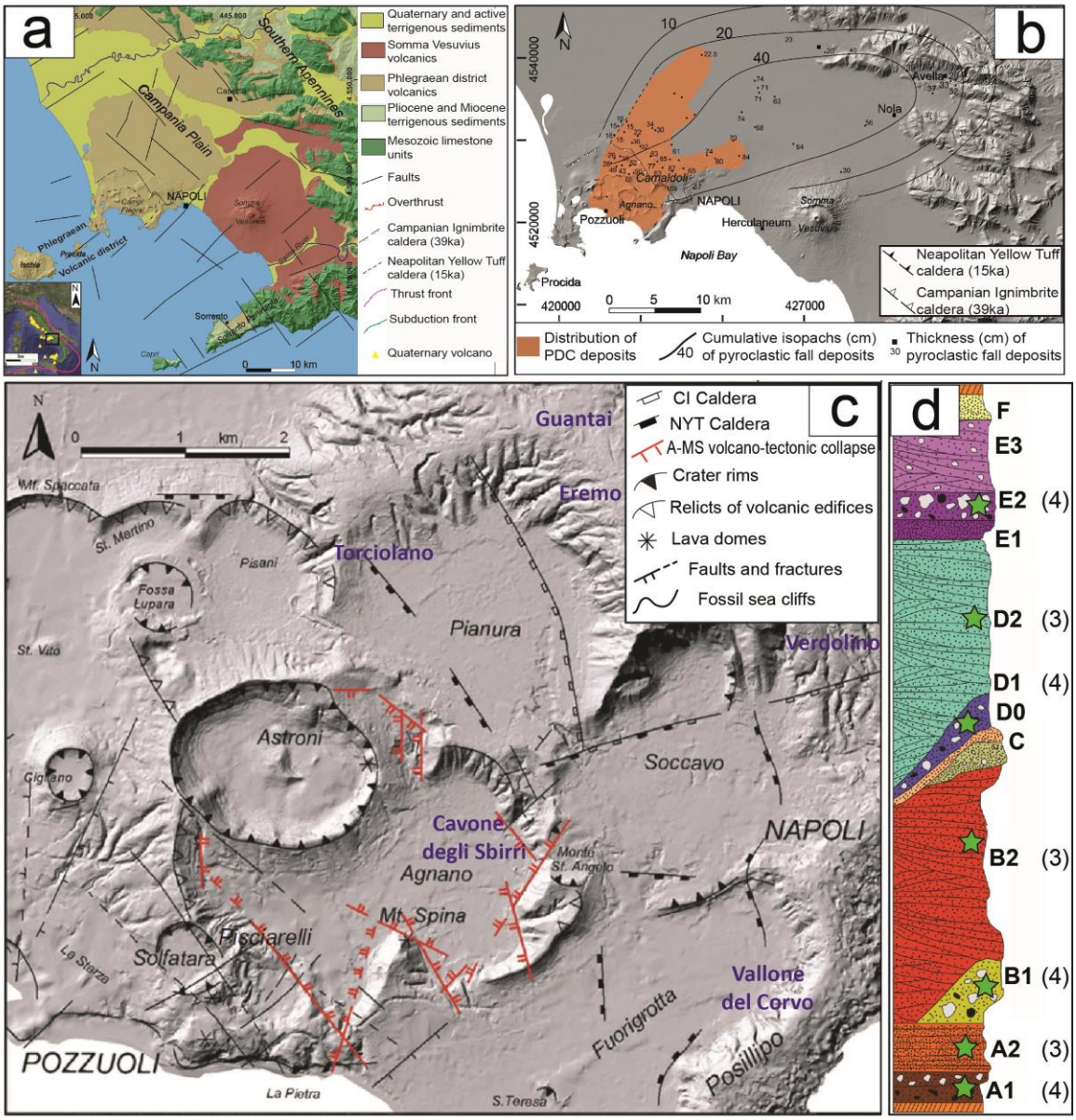

Fig. 1 a) Geological and structural sketch map of the Southern Campania Plain (modified after Orsi et al., 2003). b) Areal distribution of the A-MS volcanic deposits (redrawn after de Vita et al., 1999. c) Detail of the Agnano-San Vito area (modified after Iovine et al., 2017a) d) Schematic stratigraphic column of the A-MS erupted products, subdivided into various members (modified after Iovine et al., 2017a).; in brackets we reported the number of samples collected from each sub-member.

The volcanic activity at Campi Flegrei started at least *c.* 80 ka (Scarpati et al., 2013). The CFc is the result of multiple collapses that occurred during two big-size explosive eruptions: the Campanian Ignimbrite dated to *c.* 40 ka (Gebauer et al., 2014; Giaccio et al., 2017 and references therein) and the Neapolitan Yellow Tuff (NYT) dated to *c.* 15 ka (Deino et al., 2004). Volcanic activity has been

125 dominantly explosive through time, with several minor volcano-tectonic collapse episodes, hence
126 volcanic products of the CFc are mostly pyroclastic rocks and subordinate lava flows and domes.
127 During the last 15 ka, the caldera has been the site of intense volcanism and deformation,
128 characterized by ~ 70 eruptions grouped into three epochs of activity: epoch 1 *c*. 15–10.6 ka; epoch
129 2 *c*. 9.6–9.1 ka; and epoch 3 *c*. 5.5–3.5 ka (Di Vito et al., 1999; Smith et al., 2011). The last event,
130 possibly marking the beginning of a new epoch (e.g. Bevilacqua et al., 2017) occurred in 1538 AD
131 (Monte Nuovo eruption; Piochi et al., 2005; Guidoboni and Ciuccarelli, 2011; Di Vito et al., 2016;
132 Liedl et al., 2019). During the past *c.* 5 ka, 28 low-to medium-magnitude eruptions occurred from
133 vents mostly located in the NE part of the NYT caldera in the 12 km^2 Agnano-San Vito area (Smith
134 et al., 2011; Bevilacqua et al., 2017; Fig. 1c). This area includes the Astroni, Solfatara, and Agnano
135 craters, and is considered as one of the sites of highest probability of future resumption of volcanic
136 activity (Orsi et al., 2004; Selva et al., 2012; Bevilacqua et al., 2016, 2017). This portion of the
137 NYT caldera has been subjected to extensional tectonics since at least *c*. 5 ka (Capuano et al., 2013)
138 through NW–SE- and NE–SW-trending regional faults, favoring the ascent of trachytic and latitic
139 magmas which fed the eruptions, and it is currently affected by voluminous hydrothermal emissions
140 (Chiodini et al. 2015 and references therein). The intense fumarolic activity and the unrest episodes
141 that occurred in recent decades (Del Gaudio et al., 2010) testify to the persistent activity of the CFc
142 system. The presence of 350,000 inhabitants in the central part of the caldera raises the risk level to
143 very high (Selva et al., 2012).
144 The Campi Flegrei volcanic rocks range in composition from potassic shoshonite to trachyte and
145 phonolite and appear to be the products of magmas originated in a mantle modified by fluids/melts
146 from the subducting Ionian slab (e.g. Tonarini et al., 2004, D'Antonio et al., 2007; Mazzeo et al.,
147 2014). They exhibit a wide range of $^{87}Sr/^{86}Sr$ (07086–0.7068), but limited ranges of $^{143}Nd/^{144}Nd$
148 (0.51266–0.51240) and Pb-isotope ratios (e.g. $^{206}Pb/^{204}Pb$: 19.25–18.85; D'Antonio et al., 2007;
149 Pappalardo et al., 2002). The geochemical variability of Campi Flegrei magmas results from a
150 variety of petrogenetic processes (e.g. partial melting of the mantle source, fractional crystallization,

crustal assimilation, magma mixing; D'Antonio et al. 1999, 2007; Pappalardo et al., 1999, 2002; 2008; Fedele et al. 2008; Mangiacapra et al., 2008; Arienzo et al. 2009, 2015, 2016; D'Antonio, 2011; Di Renzo et al., 2011; Melluso et al., 2012; Pappalardo and Mastrolorenzo, 2012; Belkin et al., 2016; Forni et al., 2018; Pappalardo and Buono, 2021). Minor, poorly differentiated trachybasaltic and latitic magmas erupted at the end of the first epoch, along NE–SW trending regional tectonic structures (Orsi et al., 1996). Eruption of these magmas along the rim and differentiated magmas within the caldera testifies to the ascent of weakly differentiated, CO_2-rich magmas of deep provenance through regional faults (D'Antonio et al., 1999; Moretti et al., 2013; Arienzo et al., 2016) and to the occurrence of a shallow storage region beneath the caldera, within which the magmas evolve to trachyte and phonolite. Melt inclusion data indicate crystallization between ~ 9 and ~ 4 km (e.g., Marianelli et al., 2006; Mangiacapra et al. 2008; Arienzo et al. 2010, 2016). The trachyte and phonolite storage region is relatively shallow with respect to the reservoir from which the shoshonitic-latitic magmas rise (Pappalardo and Mastrolorenzo, 2012; Moretti et al., 2013; Fedi et al., 2018).

2.2 The Agnano-Monte Spina eruption

The A-MS eruption was the only high-magnitude event of the past *c.* 5 ka at CFc (Orsi et al. 2004, 2009) and it is considered the reference event for a future medium-size explosive eruption (Mele et al., 2015). The eruption was characterized by magmatic/phreatomagmatic activity (de Vita et al., 1999; Dellino et al., 2001) that led to the emplacement of alternating fallout and pyroclastic density current (PDC) deposits, distributed over an area of ~ 1000 km^2. The thick sequence of deposits was subdivided into various members and sub-members, named A through F from the base upwards (Fig. 1d; de Vita et al., 1999). The fallout deposits are dispersed towards the north-east. High particle concentration PDC were confined within the Agnano depression, while more dilute PDC overtopped the morphological boundary of the caldera and ran at least 20 km NE (Fig. 1b; de Vita et al., 1999). The thickness of the tephra varies from a maximum estimated value of ~ 70 m in the

177 Agnano plain, the inferred vent area for the eruption, to a few centimeters over a distance of ~ 50
178 km. Estimations based on distribution and thickness of A-MS products yield a volume of ejected
179 magma of ~ 0.9 km^3 (dense rock equivalent; Orsi et al., 2009).
180 The A-MS juvenile fragments are potassic alkaline rocks, ranging in composition from trachyte to
181 phonolite. De Vita et al. (1999) reported a general decreasing differentiation degree from bottom to
182 top of the A-MS sequence. They also noticed that the total range of variation for several trace
183 elements is large despite the limited variation of major oxide contents and found evidence for Sr-
184 isotopic disequilibria among whole rocks and minerals. The authors concluded that the A-MS
185 eruption was fed by two isotopically and chemically distinct trachytic and phonolitic magma
186 batches that mixed during the eruption. Moreover, Arienzo et al. (2010), Moretti et al. (2019) and
187 Romano et al. (2020) supported the mixing hypothesis of the previous authors and investigated the
188 role of the H_2O, CO_2 volatile phases involved prior to/during the eruption, linking them to the
189 magmatic components and to the eruption dynamics.
190

191 ## 3 Samples and methods

192 The analyzed A-MS rocks are pumice fragments extracted from different deposits outcropping in
193 the Agnano plain (Fig. 1c). Pumice fragments from the A-MS eruption are porphyritic, with
194 phenocrysts of plagioclase and alkali–feldspar, clinopyroxene, phlogopite, apatite and Ti-magnetite
195 in order of decreasing abundance (Fig. 1 in Supplementary Material 1). Feldspar, clinopyroxene and
196 phlogopite phenocrysts occur as single crystals or sometimes as aggregates. The groundmass is
197 glassy and contains rare microlites of clinopyroxene, K-feldspar, plagioclase and phlogopite.
198 In the present work, we sampled the A-MS sequence in the representative localities of Cavone degli
199 Sbirri, Guantai, Torciolano, Vallone del Corvo, Verdolino and Eremo (Fig. 1c) within and nearby
200 the Agnano plain. We collected 25 samples, which correspond to different sub-members (Fig. 1d).
201 The samples are pumice fragments collected from both fall and PDC deposits of all localities and
202 sub-members (Fig. 1d).

203 The selected pumice samples were gently crushed to lapilli-size grains through a jaw crusher. About
204 500 g of crushed sample was sieved using a stack of sieves with meshes ranging from 1ϕ to -1ϕ.
205 From the sieved aliquots, clinopyroxene, K-feldspar, phlogopite phenocrysts and pumice glass
206 fragments were hand-picked under a binocular microscope. These grains were loaded in sample
207 holders with epoxy resin and suitably polished with decreasing grain-size diamond paste. The
208 crystals were oriented in order to cut the crystals along the elongated axis, presumably the c-axis.
209 The glass fragments and clinopyroxene crystals were carefully observed in reflected and transmitted
210 light at optical microscope and in polished thin section under a binocular polarized light microscope
211 before obtaining compositional data.
212
213 **3.1 Analytical techniques**
214 An overall chemical characterization of glass and clinopyroxene crystals (Supplementary Material
215 2) from all the aforementioned A-MS eruptive members was performed at DiSTAR - University of
216 Napoli Federico II, by a JEOL-JSM 5310 electronic scanning microscope (SEM) equipped with an
217 INCA X-Act detector using energy dispersive X-ray spectroscopy (EDS) microanalysis technique.
218 Measurements were performed at a 15 kV primary beam voltage, 50–100 μA filament current,
219 variable spot size and 50 s net acquisition time. The following standards were used for calibration:
220 diopside (Mg), wollastonite (Ca), anorthoclase (Al, Si), albite (Na), rutile (Ti), almandine (Fe),
221 Cr_2O_3 (Cr), rhodonite (Mn), orthoclase (K), apatite (P), fluorite (F) and sodium chloride (Cl).
222 Relative analytical uncertainty is typically ~1% for major elements, ~3–5% for minor elements.
223 Detailed mineral composition (Supplementary Material 2) were obtained along transects of length
224 varying from 20 μm to 800 μm on zoned clinopyroxene crystals. The data were collected at the HP-
225 HT Laboratory of Experimental Volcanology and Geophysics of the Istituto Nazionale di Geofisica
226 e Vulcanologia in Rome (Italy), using a Jeol-JXA8200 electron microprobe equipped with five
227 wavelength dispersive spectrometers. This kind of specific analysis was performed on selected
228 samples belonging to A1, B1 and D1 members, which are the main fallout deposits representative

of the entire compositional range of the A-MS deposits. Crystals in carbon-coated resin mounts were analyzed under high vacuum conditions, using an accelerating voltage of 15 kV. Crystals were traversed using spots with separation of 2.5, 3.5, 5, 7 and 10 μm and variable beam diameter of 2.5, 3.5 and 5 μm, both depending on the transect length. The electron beam current was set at 7.5 nA. Elemental counting times were 10 s on the peak and 5 s on each of two background positions. Corrections for inter-elemental effects were made using a ZAF (Z: atomic number; A: absorption; F: fluorescence) routine. The range of standards for calibration was taken from Micro-Analysis Consultants (MAC; http://www.macstandards.co.uk) and variable diffraction devices: albite (Si-PET, Al-TAP, Na-TAP), forsterite (Mg-TAP), augite (Fe-LIF), apatite (Ca-PET), orthoclase (K-PET), rutile (Ti-PET), and rhodonite (Mn-LIF). Smithsonian augite (Jarosewich et al., 1980) and MAC augite were used as quality monitor standards and for the calculation of accuracy and precision. Accuracy was better than 1–5% except for elements with abundances below 1 wt%, for which it was better than 5–10%. Precision was typically better than 1–5% for all analyzed elements.

We also analyzed Sr isotopes on 5 whole-rock samples and mineral concentrates of K-feldspar, clinopyroxene and phlogopite, belonging to sub-members A1, A2, B2, D2 and E2. The Sr isotopic ratios were determined at the Radiogenic Isotope Laboratory of the Istituto Nazionale di Geofisica e Vulcanologia, sezione di Napoli-Osservatorio Vesuviano. Powdered whole rocks samples (~ 0.1 g) were leached with warm HCl for 10 min before dissolution. Sr was separated after HF-HNO_3-HCl suprapur acid dissolution using standard column chromatographic methods, through Dowex AG50WX-8 (200-400 mesh) cation exchange resins (Arienzo et al., 2013), and measured in static mode by thermal ionization mass spectrometry (TIMS) using a Thermo Finnigan Triton TI. Average $2\sigma_{mean}$, i.e., the standard error with N = 175, was better than ±0.000009. During the time of isotopic data acquisition, NIST-SRM 987 standard gave a mean value of $^{87}Sr/^{86}Sr$ = 0.710231 ± 0.000019 (2σ, N = 169). External reproducibility (2σ) during the period of measurements was calculated according to Goldstein et al. (2003). During acquisition, Sr isotopic ratios were

normalized for within-run isotopic fractionation to $^{86}Sr/^{88}Sr$ = 0.1194. The measured Sr isotopic ratios were normalized to the accepted value of NIST-SRM 987 ($^{87}Sr/^{86}Sr$ = 0.71025) standard.

3.2 Systems connectivity diagrams

The chemical variations recorded in compositional zoning patterns can be used to track the evolution of different populations of crystals through distinct magmatic environments in which they grew. Following Kahl et al. (2011, 2015), we used a population-based approach to investigate the different magmatic environments. The method was developed using olivines and has recently been applied to orthopyroxenes (Solaro et al., 2020), but has not been applied to clinopyroxenes yet to the best of our knowledge, although Mangler et al (2020) interpreted compositional zoning in a similar manner.

Minerals can be characterized by zones having constant composition for several microns along a direction: if a zone has a constant composition that differs from the constant compositions in surrounding zones, then a plot of such a concentration distribution as a profile along one direction has the shape of a plateau. Irrespective of whether the composition of the zone is higher or lower with respect to the surrounding zones, all of these flat regions in concentration profiles are referred to as "plateaus" in this work. The occurrence of plateaus in the zoning patterns of minerals, such as clinopyroxene, indicates that compositional zoning is not produced by pure fractionation, but that growth occurred for certain periods of time under stable conditions in response to fast changes of thermodynamic variables (pressure, temperature, oxygen fugacity or water fugacity). Consequently, plateaus with different composition represent several episodes of overgrowth of the crystals under different sets of P-T-X conditions. Each set of such thermodynamic variables characterizes a single magmatic environment. It is therefore possible to associate each compositional population, detected in the whole set of crystals, to a specific magmatic environment. As explained by Kahl et al. (2015), a magmatic environment does not necessarily represent a physical magmatic reservoir. Two magmatic environments could be parts of a single physical reservoir. For example, portion of a

zoned magma reservoir can differ from other parts of the same reservoir only because, for instance, the temperature is different while other variables remain fixed.

The approach uses connectivity diagrams, made up of boxes joined by lines, to systematically organize the chemical information and identify the number of magmatic environments recorded in such zoning patterns (e.g. Kahl et al., 2011 and reference therein). In the Systems connectivity diagrams, each box represents a distinct magmatic environment and each connection line indicates the composition of a crystal from core to rim, that is equivalent to the zoning type; a single arrow represents the passageway of a crystal (or a magma in which the crystal was forming), from one magmatic environments to another with different conditions. The density of the connection lines can be used to infer the dominant passageways of crystals in different environments. Such a schematic data representation immediately provides a whole picture of the zoning patterns. It is therefore possible to quantify the connections among the various magmatic environments (henceforth, ME), through the entire set of zoning pattern, in order to reconstruct the evolutionary history of crystals. Here we applied this approach to A-MS clinopyroxenes, in order to investigate growth of crystals in the different MEs that possibly characterized the A-MS plumbing system.

4 Results

4.1 Matrix-Glass

Matrix-glass analytical data (119 spots; Supplementary Material 2) have been acquired on representative samples of the A-MS eruption products. Matrix-glass shows an alkaline affinity (Na_2O+K_2O = 13.6–10.5 wt% and SiO_2 = 60.0–55.7 wt%) and mostly classifies as trachyte and subordinately as phonolite (Fig. 2a). The agpaitic index [A.I. molar $(Na^+ + K^+)/ Al^{3+}$] of A-MS glasses ranges from 0.97 to 0.75. Na_2O and K_2O contents range from 5.55 to 3.24 wt% and from 9.99 to 7.50 wt%, respectively. The Na_2O/K_2O ratio ranges from 0.70 to 0.33 while the CaO/Al_2O_3 ratio ranges from 0.19 to 0.09. TiO_2 and Al_2O_3 contents range from 0.75 to 0.17 wt% and from 19.8

to 18.1 wt%, respectively. $FeO_{(tot)}$ and MgO contents range from 4.27 to 2.58 wt% and from 1.12 to 0.33 wt%, respectively (Fig. 2 in Supplementary Material 1).

The analyzed A-MS matrix-glasses are Ne-normative and their Mg# [molar $Mg^{2+}/(Mg^{2+}+Fe^{2+})*100$] varies from 43 to 24. The Mg# of the whole-rocks, taken from literature (de Vita et al., 1999) for comparison, ranges from 45 to 31, thus slightly shifted toward less evolved compositions. SiO_2 and Na_2O contents show positive correlation with the degree of chemical evolution (decreasing Mg#; Fig. 2 in Supplementary Material 1), whereas CaO, MgO and $FeO_{(tot)}$ contents show negative correlation. K_2O content increases with Mg# decreasing from 43 to 30 and then decreases with Mg# decreasing from 30 to 24; Al_2O_3, and MnO contents are constant, although scattered. The degree of differentiation generally decreases from bottom to top of A-MS deposits. In fact, even if partially overlapped, there is a remarkable difference in the major oxide contents of the A-MS volcanic products sampled in the different members (from A to F). In particular, glass from members A to B show on average a slightly more differentiated composition than those from members D to F (Fig. 2a; Fig. 2 in Supplementary Material 1).

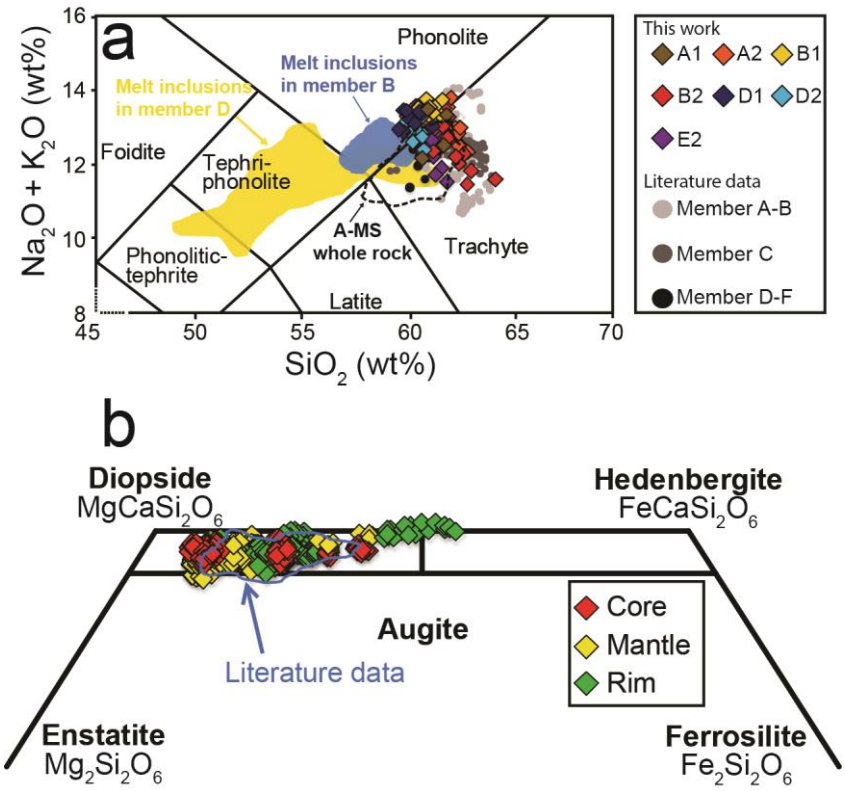

Fig. 2 a) Glass compositions of A-MS products plotted in the Total Alkali vs. Silica diagram; melt inclusion data are from Arienzo et al. (2010); whole rock and matrix-glass compositions are from de Vita et al. (1999). b) Di-Hd-En-Fs classification diagram of clinopyroxenes found in A1, B1 and D1 members of the A-MS deposits; literature data refer to clinopyroxene from A-MS products (de Vita et al., 1999; Arienzo et al., 2010); mantle refers to the zones/sectors of the crystals between the core and the most external rim.

.

4.2 Clinopyroxene

Clinopyroxene from A-MS deposit occurs as euhedral to anhedral dark green phenocrysts and microcrysts in the groundmass. Both kinds of clinopyroxene have a diopsidic composition (Wo_{51-54}-En_{49-30}-Fs_{27-4}; Fig. 2b). On the other hand, clinopyroxene shows a significant compositional heterogeneity that is well reflected in the Mg# [molar $Mg^{2+}/(Mg^{2+} + Fe_{tot})$ *100] which ranges from 92 to 45 (Fig. 3a). Na_2O, Al_2O_3 (Fig. 3d), TiO_2 (Fig. 3e) and FeO contents increase with decreasing Mg#. TiO_2 and Al_2O_3 contents range from 1.29 to 0.27 wt% and from 7.17 to 1.39 wt%, respectively (Fig. 3d-e). Na_2O content ranges from 0.87 to 0.10 wt% (Fig. 3b). The whole set of acquired data allowed to enlarge the already known compositional range of clinopyroxene from A-MS (cyan bordered field in Fig. 2b; de Vita et al., 1999; Arienzo et al., 2010).

About 300 separated clinopyroxene crystals have been selected and then observed under a polarizing microscope. However, quantitative compositional zoning profiles have been only measured on the 41 crystals showing optical evidence of compositional variations. These make up a minor percentage (~15%) of the overall population. On 46 of the remaining optically unzoned clinopyroxenes, single spots major and minor element concentrations have been acquired. The optically unzoned clinopyroxene crystals show a quite homogeneous composition (Supplementary Material 2): 40 out of 46 analyzed crystals have Mg#= 75±5 (Fig. 3a). Only four out of the 46 analyzed homogeneous clinopyroxene crystals show higher (Mg# = 87±5) values. Two other crystals exhibit lower (Mg# = 60±5) values.

346 4.2.1 Compositional populations

347 As for the zoned crystals, we refer mantle to define the optically discriminable zones between the
348 core and the rim. Frequency histograms (Fig. 3a-c) of core, mantle and rim compositions show that
349 there are different compositional populations. In particular, through the Mg# parameter (Fig. 3a;
350 Table 1), it is possible to clearly distinguish: 1) a population of compositions, hereafter referred to
351 as ME0, characterized by high Mg# (92-85), occurring in 70% of the analyzed zoned crystals, in
352 most cases represented by crystal cores; 2) a population, hereafter referred to as ME1, with Mg#
353 between 84 and 80, occurring in 34% of the analyzed zoned clinopyroxenes and that mostly
354 constitutes the mantles of the crystals; 3) a population of compositions, hereafter referred to as
355 ME2, with Mg# between 78 and 70 and with an average value of 75, occurring in all the analyzed
356 zoned clinopyroxenes and, in particular, in almost all their rims. Notably, this is also the
357 composition of the unzoned crystals, which make up 85% of the overall population. 4) a further
358 population is represented by few cores and mantles with low Mg# (69–60) found in 7% of the
359 zoned analyzed crystals, hereafter referred to as ME3. Moreover, the rim of a single crystal showing
360 very low Mg# (55–45) is also referred to as ME3 in Fig. 4. In summary, ME0 and ME2 make up
361 most of the zoned clinopyroxene population, with the most mafic compositions (ME0) generally
362 recorded in the cores. Although there are subtle variations in the distribution patterns of Al_2O_3 and
363 Na_2O contents of the pyroxene crystals that are discussed below in detail, the classification into
364 different groups is largely corroborated by these compositional parameters as well (e.g. Fig. 3).

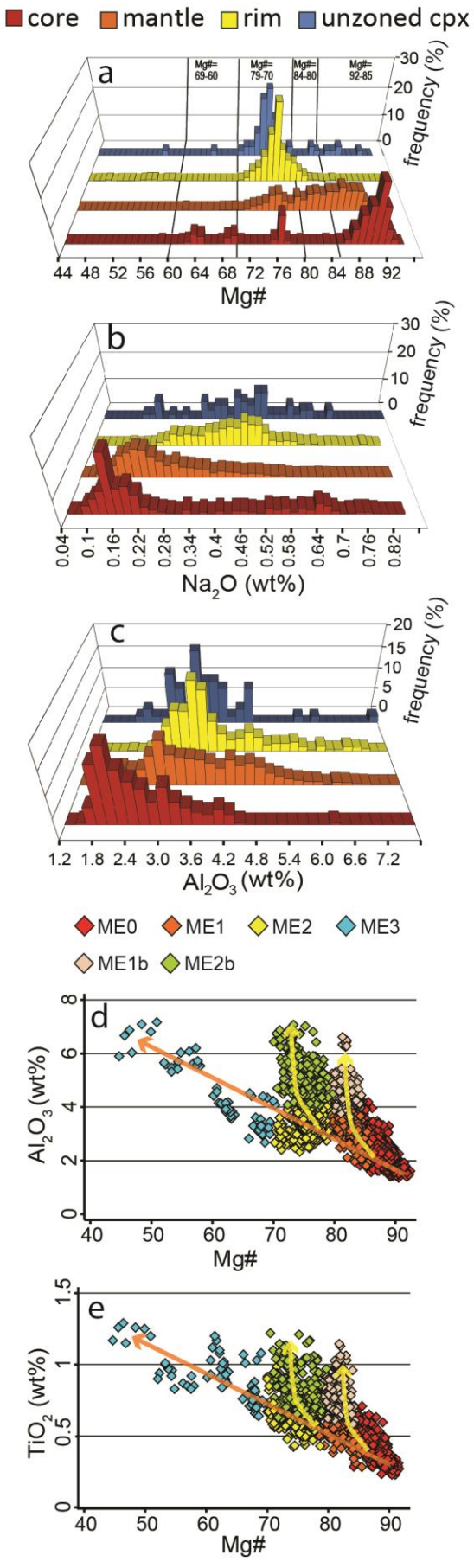
core
mantle
rim
unzoned cpx
a
Mg#= 69-60
Mg#= 79-70
Mg#= 84-80
Mg#= 92-85
frequency (%)
Mg#
b
Na2O (wt%)
c
Al2O3 (wt%)
ME0
ME1
ME2
ME3
ME1b
ME2b
d
e
TiO2 (wt%)

365

Fig. 3 a) Mg#, b) Na_2O and c) Al_2O_3 frequency histograms of core, mantle and rim of the zoned A-MS clinopyroxenes. These allow different populations to be identified. d) Al_2O_3 vs Mg# and e) TiO_2 vs Mg# variation diagrams of the analyzed zoned A-MS clinopyroxenes showing a wide compositional range and different populations and sub-populations. Note that all clinopyroxenes of different compositions lie on a trend defined by the orange arrow, with the exception of the ME1b and ME2b trends, which are shown in yellow. The significance of these trends is discussed in section 4.6.

The main difference between the three analyzed members is that only member B1 has a significant number (9 out of 15 analyzed crystals) of zoned clinopyroxene crystals with cores showing ME2 and ME3 compositions; in zoned clinopyroxene from the member A1, cores have only ME0 composition. Only 4 out of 20 cores of the crystals from member D1 show a ME2 composition. Indeed, member D1 has a large proportion of zoned clinopyroxenes (15 out of 20 analyzed crystals) with ME1 and ME0 composition; this is consistent with the composition of its matrix-glass, which is less differentiated with respect to the composition of A-B members. An important observation is that despite the wide compositional variability of cores and mantles, crystal rims show a homogeneous composition: except the crystal rim with very low Mg#, all crystal rims show Mg# between 78 and 70, thus pertaining to ME2. Nevertheless, Al_2O_3 and TiO_2 show an overlap in the compositional populations that are distinguishable based on their Mg# (Fig. 3). In particular, these elements show a wider compositional range in the populations of rims (ME2) and mantles (ME1), so it is possible to discriminate two other subpopulations (ME1b and ME2b), which, at similar Mg# values, are characterized by higher contents of Al_2O_3 and TiO_2 (Fig. 3d-e). Thus, in terms of Al_2O_3 and TiO_2, mantles and rims show a compositional heterogeneity, despite they have homogeneous MgO, FeO and Na_2O contents. This aspect will become relevant in the construction of diffusion models.

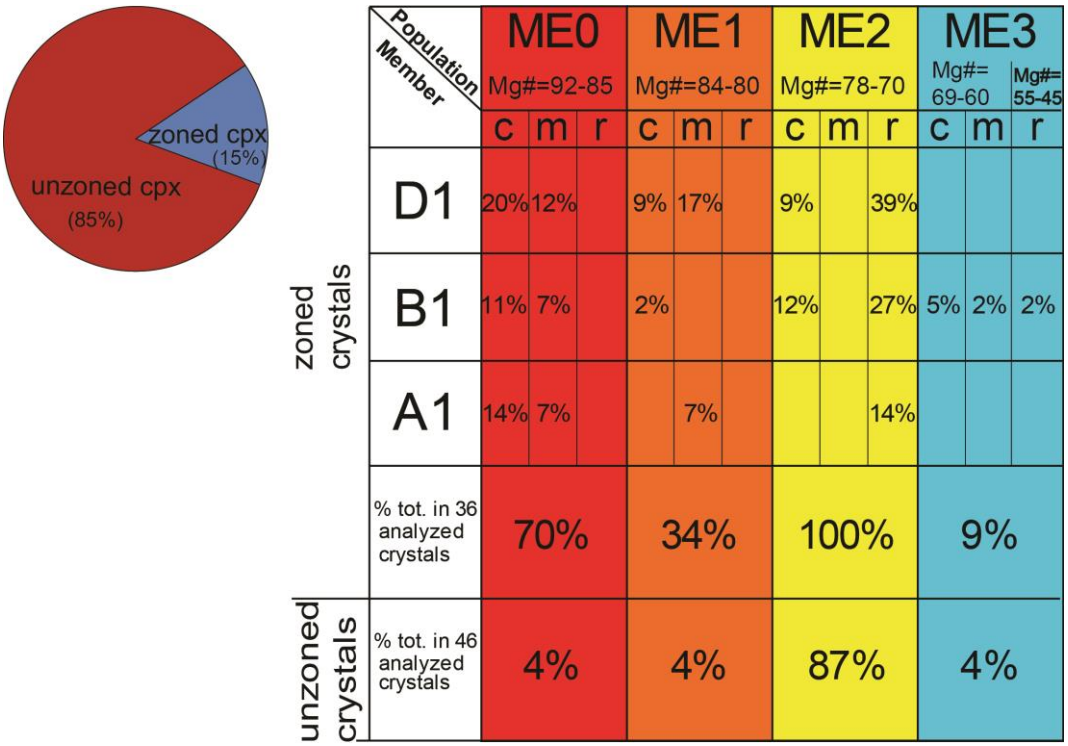

Fig. 4 The colored table reports, for each sub-member, the frequency of occurrence of a compositional population in a zoning sector (core, mantle or rim) in a total of 36 (out of 41) analyzed clinopyroxene crystals of the A-MS deposit; c=core; m=mantle; r=rim. Percentages have been calculated considering clinopyroxenes with plateaus (36 out of 41). Percentage of compositional populations occurring in the homogeneous clinopyroxene crystals is also reported. % tot.in rows at the bottom express the abundance of a compositional population in all the analyzed crystals (36 for the zoned and 46 for the unzoned crystals, respectively).

4.2.2 Compositional Zoning

The concentration profiles measured along core-to-rim traverses in zoned clinopyroxenes allowed to characterize their zoning patterns. In 36 out of 41 crystals, the zoning pattern of the main elements consists of two or more plateaus with a constant composition separated by either sharp or gradual boundaries (Fig. 5). Based on the chemical composition and the type of variation shown by plateaus, various types of zoning patterns have been identified, i.e. normal, reverse or complex. Normal zoning is defined by decreasing Mg# from core to rim while reverse zoning is characterized by increasing Mg# from core to rim of the clinopyroxene. Complex zoning refers to crystals

405 characterized by more than two plateaus, i.e. crystals showing normal-to-reverse zoning, in which
406 Mg# decreases from core to mantle and increases from mantle to rim.
407 The most common pattern (44%) is normal zoning (type I; Fig. 5a), consisting of cores with high
408 Mg# (92–80; ME0-ME1) and rims with intermediate composition (Mg# = 78–70; ME2) showing
409 sharp variation between these. Another type of zoning is type II (5%), that is similar to the normal
410 zoning type I, but differs in that the variation is gradual (Fig. 5b). Only one normally zoned crystal
411 (type III; Fig. 5c) shows a core with intermediate composition (Mg# = 75–73; ME2) and a rim with
412 low Mg# (55–45; ME3). Another less common zoning type (type IV; Fig. 5d; ~ 5%) is represented
413 by reversely zoned crystals in which cores with Mg# of 68–63 (ME3) are surrounded by rims with
414 less differentiated composition (Mg# = 75–73; ME2). Several types of complex zoning patterns are
415 also common. Most crystals have a reverse to normal zoning (type V; Fig. 5e; ~ 22%), with a core
416 characterized by intermediate composition (Mg# = 81–72; ME1 or ME2), a mantle with higher Mg#
417 (82–92; ME0 or ME1) and a rim with Mg# of 75–72 (ME2). An individual (type VI; Fig. 5f) from
418 member B1 shows a variation from Mg# = 75 (ME2) in the core, through Mg# = 63 (ME3) in the
419 mantle, to Mg# = 75 (ME2) in the rim. Finally, oscillatory zoned (type VII; Fig. 5g; ~ 7%) crystals
420 are also present, showing an alternation of zones consisting of several plateaus with composition
421 ranging from Mg# = 92–88 (ME0) to 84–82 (ME1) and a rim with Mg# = 75 (ME2). Moreover, a
422 few crystals (type VIII; Fig. 5h; ~ 12%) show normal or oscillatory zoning with gradual variation
423 (Mg# from 81 to 71) without plateaus.

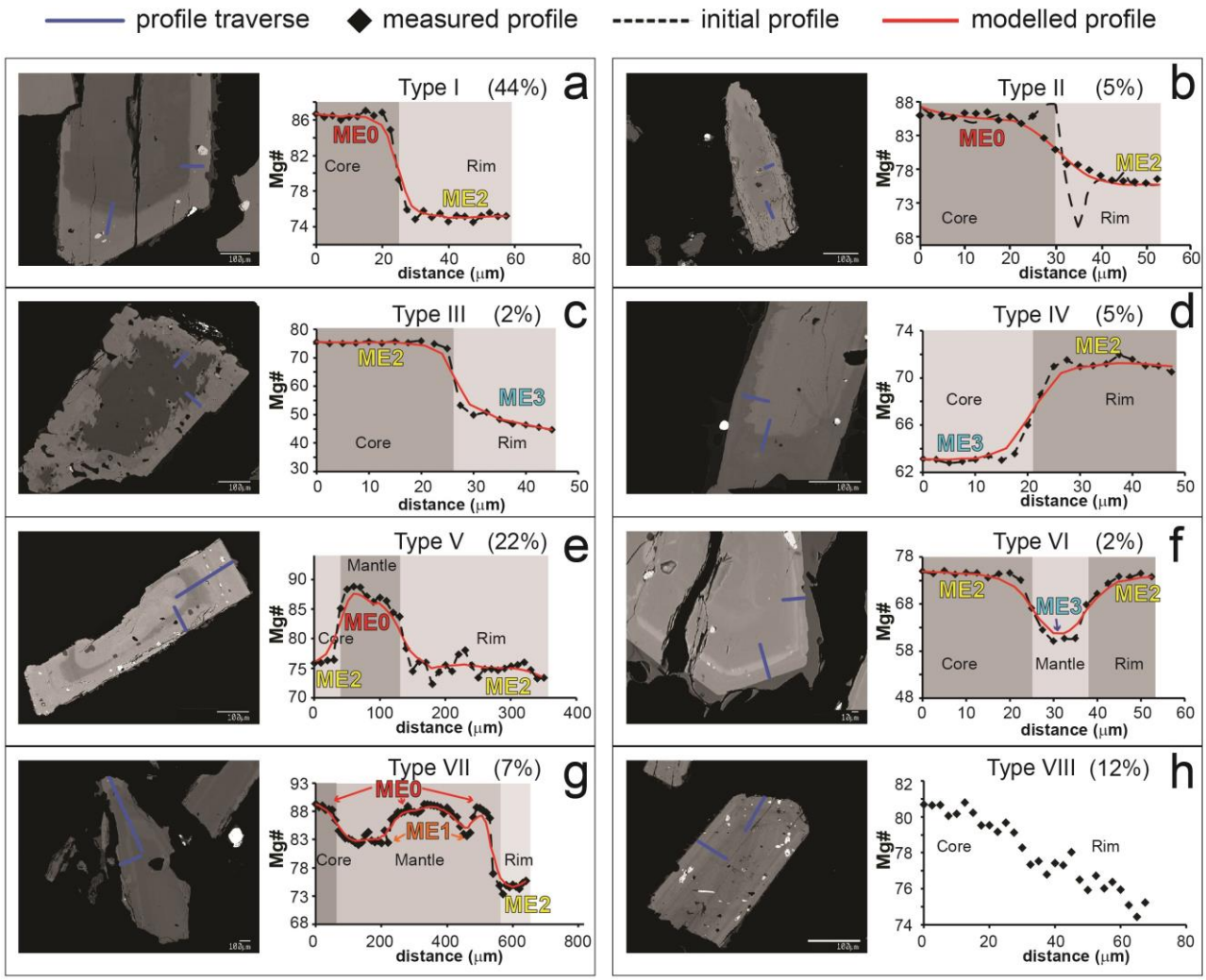

Fig. 5 Types of zonation of the A-MS clinopyroxenes. Black diamonds are measured analysis along the crystal traverses showing concentration profiles from core to rim [Mg# = molar $Mg^{2+}/(Mg^{2+} + Fe_{tot})$]. In the BSE images, the blue lines are the traverses along which the chemical composition has been acquired. Black dashed lines indicate the initial profile shapes: these are different depending on the two methods applied for diffusion modeling and have been inferred through the relationships between Al_2O_3 (wt%) and Mg# in the profiles Red lines indicate modelled profiles. A complete description of the diffusion modeling methods is provided in section 4.6. The numbers in brackets indicate the percentage of zoned clinopyroxenes exhibiting such a pattern.

4.3 Sr isotope composition of whole rocks and minerals

The whole-rock samples from the sub-members A1 and A2 show $^{87}Sr/^{86}Sr$ isotopic ratios = 0.70747. Whole rocks from sub-member B2 have a $^{87}Sr/^{86}Sr$ isotopic ratio = 0.70749, whereas samples from sub- members D2 and E2 show higher $^{87}Sr/^{86}Sr$ isotopic ratios that are 0.70753 and 0.70750, respectively (Fig. 6a). Feldspars from all the A-MS members show a Sr-isotopic signature in the

range 0.70750–0.70748 (Fig. 6b). The Sr-isotopic signature of clinopyroxenes shows a significant range of variation, increasing from 0.70745 in member A1 to 0.70756 in member D2 and then slightly decreasing to 0.70755 in member E2 (Fig. 6c). Only phlogopite crystals from member E2 have been analyzed and they show a $^{87}Sr/^{86}Sr$ value of 0.70753 (Supplementary Material 2). Notably, on average, the Sr isotopic ratios increase with stratigraphic height: this is particularly evident in whole rocks and clinopyroxenes (Fig. 6a, c). The new isotopic data acquired on whole rocks and mineral phases of the analyzed samples are reported in Supplementary Material 2 and are consistent with the range reported in literature (Fig. 6).

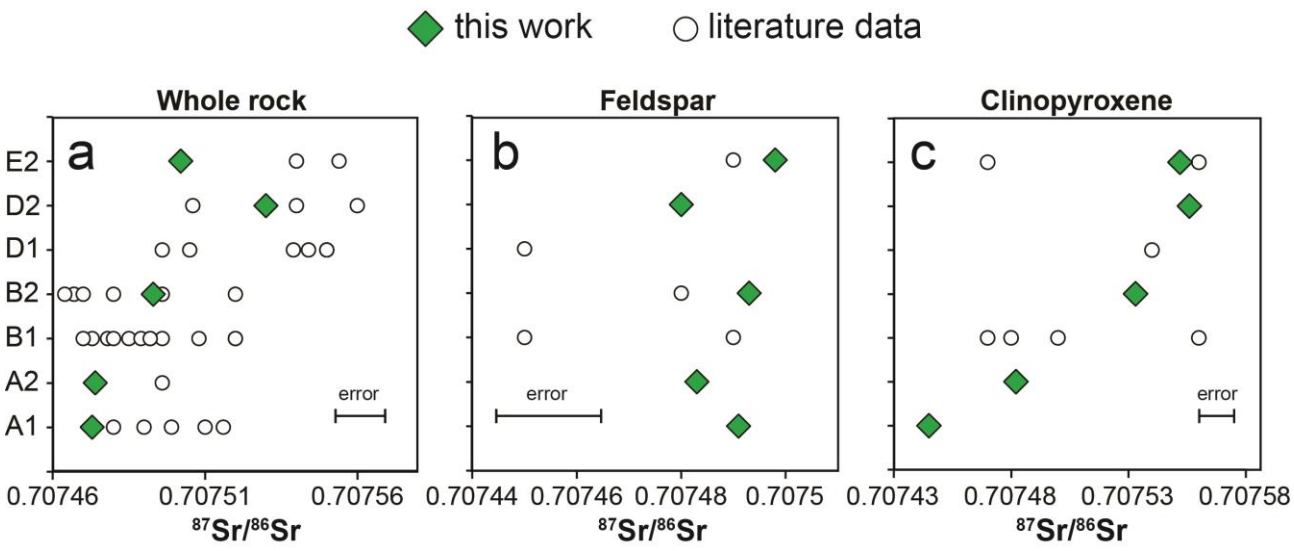

Fig. 6 Stratigraphic height vs Sr-isotopic composition of A-MS whole rocks and minerals. Literature data are from de Vita et al. (1999) and Arienzo et al. (2010).

4.4 P-T conditions of clinopyroxene crystallization

Clinopyroxene-liquid thermometers and barometers specific for alkaline magmas (Masotta et al., 2013) have been used in order to investigate the crystallization conditions of the A-MS clinopyroxenes. However, only few clinopyroxenes have passed the compositional test for equilibrium (Fig. 7a), implying that the majority of the crystals, mostly those belonging to ME0 and ME1, grew in a more mafic melt and were subsequently trapped in the A-MS trachytic magma. Nevertheless, we noted that some of these clinopyroxenes are in equilibrium with whole rocks

and/or melt inclusions representative of poorly evolved trachybasaltic to latitic Campi Flegrei magmas (Beccaluva et al., 1991; Civetta et al., 1991a; D'Antonio et al., 1999; Lustrino et al., 2002; Mastrolorenzo and Pappalardo, 2006; Cannatelli et al., 2007).

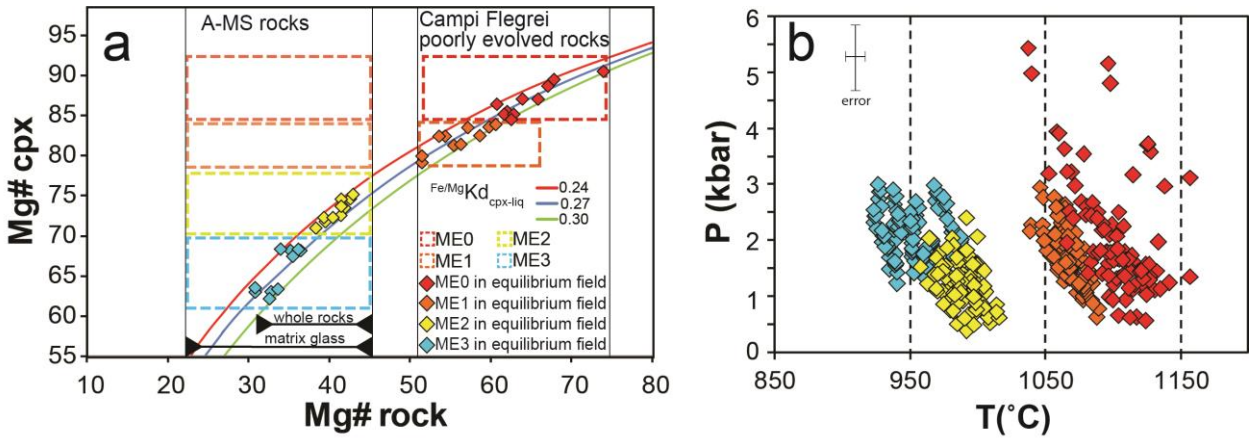

Fig. 7 a) Fe-Mg partitioning between clinopyroxene and host rock ($^{Fe/Mg}Kd_{Cpx\text{-}liq}$ = 0.27±0.03; Grove and Bryan, 1983; Putirka et al., 2003); fields demarcated by colored dotted lines represent the whole set of A-MS clinopyroxenes, belonging to different magmatic environments, compared to host rocks; the transparent colored dotted lines refer to clinopyroxenes with high Mg# (ME0 and ME1) compared to A-MS whole rocks and matrix glass compositions: these clinopyroxenes are out of equilibrium with respect to their host rocks; some of these clinopyroxenes are in equilibrium with more mafic rocks; diamond symbols refers to some clinopyroxenes which passed the compositional test for equilibrium and have been used for geothermobarometry. b) Output pressures and temperatures estimates for the different magmatic environments of the A-MS clinopyroxenes obtained by the clinopyroxene-liquid thermometers (equation Talk2012) and barometers (equation Palk2012) specific for alkaline magmas (Masotta et al., 2013); error bars refer to SEE.

We consider only clinopyroxene crystals in equilibrium with hypothetical melts, i.e. crystals from the ME0 and ME1 in equilibrium with Campi Flegrei poorly evolved volcanic products, and crystals from ME2 and ME3 in equilibrium with A-MS matrix-glass compositions (Fig. 7a). Different ranges of temperature have been obtained for the variable clinopyroxene populations (Fig. 7b; Supplementary Material 3). The most mafic compositions yield the highest temperatures, with averages of 1104±24 °C for ME0 and 1066±11 °C for ME1. Average temperatures for ME2 and ME3 are 990±13 °C and 952±18 °C, respectively. The standard error of estimate (SEE) of the used geothermometer (Masotta et al., 2013) is 18.2°C and hence, in the case of ME1 and ME2, it is

slightly higher than the standard deviation calculated from the output values. The estimated pressure is similar for all the populations ranging between 3.0 and 0.5 kbar, with an average value of ~ 1.7 kbar. Only a few output data show pressures >3 kbar. With the exception of a few clinopyroxenes from ME0 and by considering that the SEE of the geobarometer is 1.15 kbar, the obtained pressure range is the same for the different magmatic environments, which likely indicates that the resolution in pressure is not good enough to discriminate reservoirs at different depths.

4.5 Magmatic environments recorded in A-MS clinopyroxenes

In Fig. 8, the Systems connectivity diagram schematically shows the A-MS clinopyroxene zoning pattern.

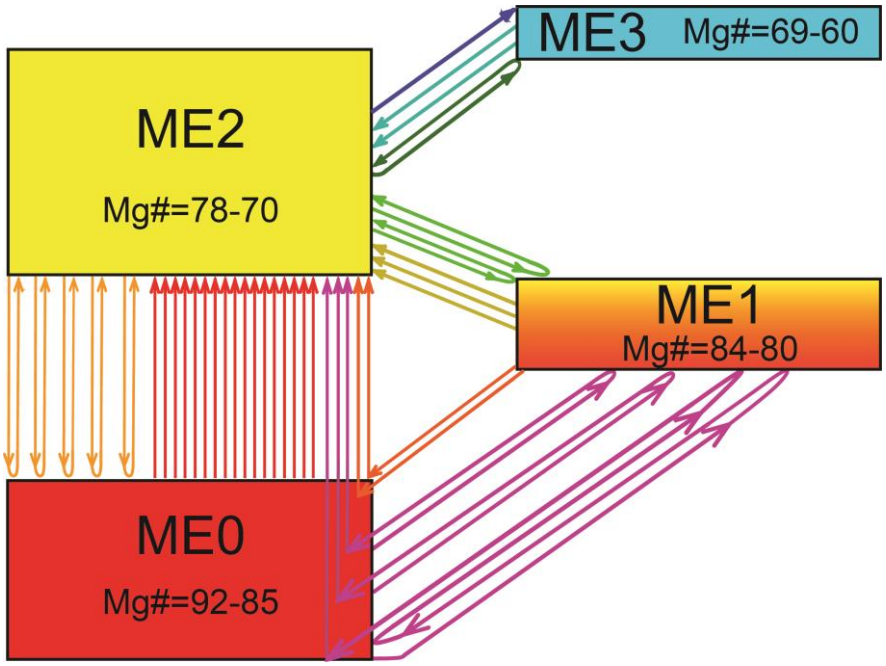

Fig. 8 Systems connectivity diagrams of the zoning patterns of A-MS clinopyroxene crystals. Since each compositional population can be associated to a specific magmatic environment (see section 3.2), the different magmatic environments are characterized by different ranges in the Mg#. Different zoning types are depicted by different connection lines represented by different color (e.g. the orange routes represent clinopyroxene crystals with core formed in ME2, mantle formed in ME0 and the rim formed in ME2). The height of the boxes is proportional to the frequency of occurrence of the magmatic environments. The A-MS clinopyroxene zoning patter is characterized by most of the connection lines linking ME0 and ME2, also passing through ME1, and a few connections linking ME2 and ME3.

Such an analysis reveals that, despite the complex diversity of zoning patterns, certain evolutionary tracks are recurrent in the history recorded by the clinopyroxene populations. It can be noted that there are many connections, depicted as arrows in Fig. 8, between the ME0 and ME2 environments. The connections often pass also through ME1 that represents an environment compositionally intermediate between ME0 and ME2. Finally, there is a much smaller number of connections between ME2 and ME3. Based on the available data, there are no connections between either ME0 or ME1 and ME3; this allows us to divide the evolutionary history of A-MS clinopyroxene phenocrysts into two steps: one involves the interaction among the magmatic environments ME0, ME1 and ME2, the other involves ME2 and ME3. Moreover, as also visible in the frequency histograms (Fig. 3), it is worth noting that both crystal cores with high Mg# (ME0) and crystal cores with low Mg# (ME3) converge toward an intermediate composition (ME2) at the rim. At this point it is necessary to recall that this distinction in different magmatic environments is supported by other compositional variables such as Na_2O, Al_2O_3 and TiO_2 contents, with the exception of the ME1b and ME2b groups of Al_2O_3 and TiO_2 contents that occur in the rim and mantle regions of the zoned clinopyroxenes. These will be discussed in detail in the following section on diffusion modeling.

4.6 Diffusion modeling

Kinetic modeling of the zoning patterns in clinopyroxene, which record fluctuations through the different magmatic environments, can yield information on the timescales over which the processes that created the different types of zoning took place. The well preserved plateaus found in most profiles can be used to infer the initial profile shapes before diffusion occurred. Given the different kinds of zoning profiles, two different methods for modeling have been used here. I. Most of the profiles, characterized by compositional plateaus and sharp gradients show little evidence of diffusive modification of growth zoning. In these cases, it is possible to calculate the relaxation of growth zoning timescales (e.g. see Chakraborty and Ganguly, 1991; Trepmann et al., 2004) to infer

maximum possible durations that the crystals may have spent in a magmatic reservoir at a given temperature without perceptible, within the analytical resolution of this study, diffusive modification of the profiles. II. In a small subset of profiles (e.g. Type II) diffusive gradients are observed and these can be modelled to fit the observed profiles and yield durations of residence of the crystals in a magmatic environment. In both cases, solutions to the diffusion equation

$$\frac{dC}{dt} = \frac{d}{dx}\left(D(t)\frac{d}{dx}\right) \qquad (1)$$

are sought with an appropriate choice of initial and boundary conditions. The equation describes how concentration gradients (i.e., concentration profiles: dC/dx), evolve as a function of time and this aspect is utilized to obtain information on timescales from measured concentration profiles (e.g. Chakraborty et al., 2008). We have carried out the diffusion modeling at temperatures corresponding to that of the ME2 environment (990 °C) because, in most cases, this is the final temperature at which clinopyroxenes grew and resided before eruption, at least for ~ 98% of the zoned crystals, as well as the homogeneous crystals, which make up 85% of the clinopyroxene population. We have used diffusion coefficients calculated using the expression provided by Müller et al. (2013):

$$D^{\mathrm{Fe-Mg}} = 2.77 \pm 4.27 * 10^{-7} \exp\left(\frac{-320.7 \pm \frac{16\mathrm{kJ}}{\mathrm{mol}}}{RT}\right) \mathrm{m}^2/\mathrm{s} \qquad (2)$$

where *R* is the gas constant and *T* is the temperature in Kelvin.

In the method I, the measured profiles are taken as the initial profiles and equation (1) and (2) are used to numerically calculate evolution of the profile shapes as a function of time. The boundary conditions for these calculations may be either constant composition or no flux at the rims of crystals, with little difference in the results. Timescales on which the calculated profiles deviate measurably from the initial profiles are considered to be upper limits of residence times of crystals in a particular magmatic environment. Fig. 5 (except Fig. 5b: Type II) shows examples of different kinds of profiles modeled through method I. The upper limit residence times for different plateau

compositions in the various types of zoning profiles are listed in Table 1. These are found to be < 25 years, with durations < 15 years being the most common.

Table1

Member	cpx n°-traverse n°	Method I	Method II
A1	cpx1-1	14.3	
	cpx1-2	15.5	
	cpx2-1	6.7	
	cpx2-2	6.7	
	cpx3-1		48.2
	cpx3-2		37.8
	cpx5-1		68.2
	cpx5-2		61.0
B1	cpx1-1	8.9	
	cpx1-2	8.9	
	cpx2-1	8.9	
	cpx2-2	7.1	
	cpx4-1		48.3
	cpx4-2		52.6
	cpx5-1	12.7	
	cpx5-2	9.5	
	cpx6-1	4.8	
	cpx6-2	4.8	
	cpx7-1	14.3	
	cpx7-2	4.8	
	cpx8-1	9.5	
	cpx8-2	12.7	
	cpx9-1	20.9	
	cpx9-2	7.6	
	cpx10-1	11.4	
	cpx10-2	8.6	
	cpx11-1		47.2
	cpx11-2		52.5
D1	cpx2-1	14.3	
	cpx2-2	6.8	
	cpx5-1		43.8
	cpx5-2		50.6
	cpx7-1	10.5	
	cpx7-2	11.1	
	cpx8-1	14.3	
	cpx8-2	9.5	
	cpx9-1	6.1	
	cpx9-2	8.6	
	cpx10-1	20.3	
	cpx10-2	6.7	
	cpx11-1	18.0	
	cpx11-2	6.7	
	cpx13-1	24.7	
	cpx13-2	7.9	
	cpx14-1	8.6	
	cpx14-2	5.2	
	cpx18-1	9.4	
	cpx18-2	7.9	
	cpx19-1	12.9	
	cpx19-2	5.3	

Table 1 Timescale (in years) estimates for Agnano-Monte Spina clinopyroxene crystals derived from Fe-Mg diffusion modeling across selected transects, calculated at T = 990 °C. In method I, the measured profile has been used as initial profile and the time term of the equation (1) has been varied until the modeled profile slightly oversteps the initial profile: the maximum diffusive smoothing

557 that a concentration (Mg#) profile has undergone has been modeled, thus yielding maximum times of residence. In method II, the
558 shape of the initial profile has been inferred from the relationship between Al_2O_3 and Mg# (Fig. 8); the residence times have been
559 modeled by obtaining the fit with the measured profile.
560
561 In the method II, on the other hand, it is necessary to define the shapes of the initial profiles and
562 then model their diffusive modification. To do that, element concentrations that are correlated with
563 each other through petrogenetic processes but diffusing at different rates are useful. Here we make
564 use of Mg# and Al_2O_3 concentration in the clinopyroxene crystals, which are anti-correlated with
565 each other (e.g. see Fig. 3) because Mg-content decreases as Al-content increases during fractional
566 crystallization as well as partial melting processes (e.g. Jagoutz et al., 1979). As discussed above
567 (see caption of Fig. 3), there are two groups of compositions, ME1b and ME2b, that deviate from
568 this trend. It is possible to reliably infer the initial profile shapes of crystals which exhibit this
569 characteristic: by plotting Al_2O contents vs Mg# in a profile, it is possible to obtain a linear
570 correlation. Most of crystals show a good correlation, as shown by the fit of the data by a linear
571 trend-line (in Fig. 9a, R^2=0.94). This correlation can be then used to infer the hypothetical initial
572 Mg# profile, plotted in figure 9b. Within the accuracy of the data, it is hardly possible to see the
573 difference between the measured profile and the theoretical profile, in particular, in the region with
574 the sharp compositional gradient. This implies that the Mg# profile was little or even not at all
575 affected by Fe-Mg interdiffusion. For these crystals, it has been possible to estimate a maximum
576 timescale using method I: in this case, since the inferred profile is very similar to the measured
577 profile, the latter has been used as initial profile in the modeling. It is then possible to deduce that
578 where Mg# and Al_2O_3 are correlated according to the overall general trend, the profiles of Mg# and
579 Al_2O_3 track each other completely and the shapes overlap with each other. Conversely, when Al_2O_3
580 content is higher at a given Mg# compared to the value expected from the overall correlation trend,
581 such as for crystals showing ME1b and ME2b trends (Fig. 3e-f), the Al_2O_3 preserves a sharper
582 gradient whereas the Mg# shows more smoothed concentration patterns (e.g. zoning Type II). In

583 this case, the correlation between Mg# and Al_2O_3 content is not good (in Fig. 9c, R^2=0.74),
584 indicating that the original trend was overprinted by Fe-Mg interdiffusion. It is possible to estimate
585 an original trend by taking the Mg# and Al_2O_3 contents of the two plateau regions, which is plotted
586 as blue line in Fig. 9c. This original correlation has been used to estimate a growth zoning of Mg#,
587 which is the initial profile in Fig. 9d. We observe that the Mg# theoretical initial profile noticeably
588 deviates from the measured profile and the strongest difference is in the region with the large
589 compositional gradient of Al_2O_3. An example of such a profile, with the initial and the final
590 modelled profile shapes is shown in Fig. 5b and Fig. 9c-d. This indicates that Mg has diffused to
591 some extent and Al has not and this is consistent with the known experimentally measured diffusion
592 behavior of these elements (Mg vs. Al) in clinopyroxenes (e.g. Fe-Mg: Müller et al., 2013; Al:
593 Sautter et al., 1988). Thus, the shape of the Al_2O_3 profile can be taken as the initial profile shape for
594 Mg# (i.e. as a grown profile) and diffusion modeling may be used to try to reproduce the measured,
595 diffused concentration profile shape of Mg#. We have modelled the system as an infinite diffusion
596 couple, i.e. boundary conditions are $C = C_{initial}$ at $\pm\infty$ (i.e. the two ends of a profile). Two
597 compositional traverses were acquired across each clinopyroxene crystal. If modeling of both
598 profiles did not yield the same time estimates the values were not used because the concentration
599 profiles were considered to be affected by processes other than diffusion or artefacts such as oblique
600 sectioning effects (Costa et al., 2008). On the other hand, the fact that in many cases the same
601 timescales were obtained from profiles that are oriented in mutually perpendicular directions may
602 point to a limited anisotropy of Fe-Mg diffusion in clinopyroxene; that indeed has not been
603 measured experimentally yet.

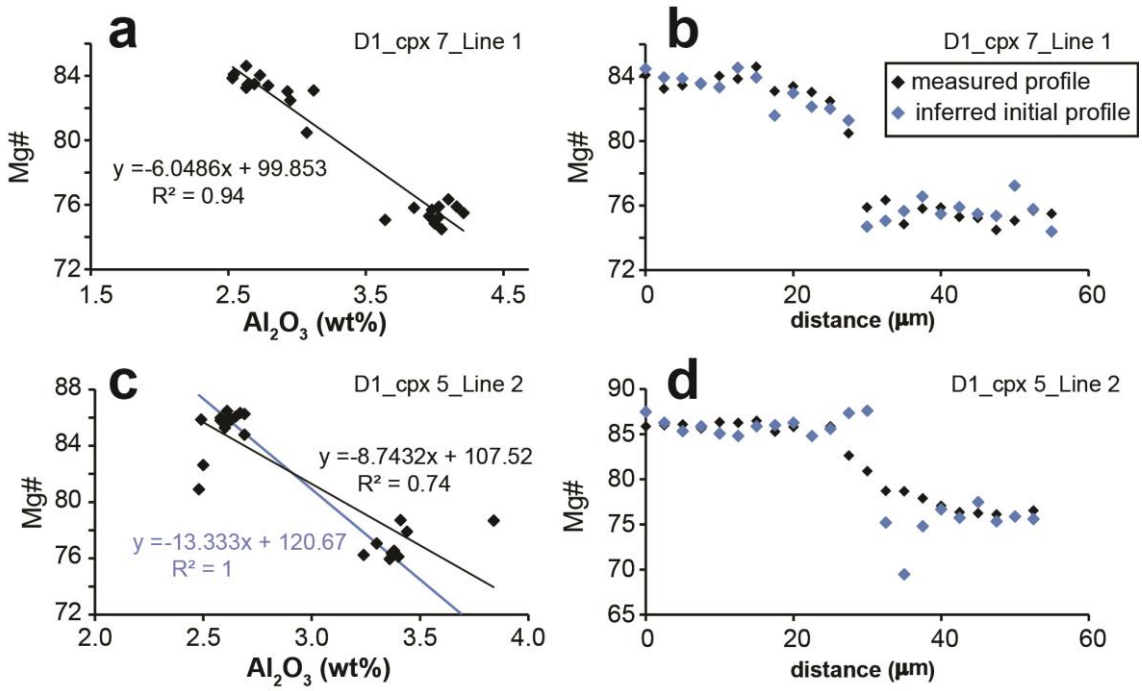

Fig. 9 a,c) Mg# vs Al_2O_3 (wt%) relations of two selected crystal profiles. b,d) measured and inferred initial Mg# profiles. In Fig. 9a, the profile show a good correlation (R^2=0.94; black trend-line) between Mg# and Al_2O_3 (wt%). In Fig. 9b, the inferred initial profile is calculated based on the relations assessed by best fit of the linear trend-line of Fig. 8a. In Fig. 9c, the profile does not show a good correlation (R^2=0.74; black trend-line) between Mg# and Al_2O_3 (wt%). By taking into account the Mg# and Al_2O_3 (wt%) contents of the two plateaus (without the points in the boundary region between the plateaus), a new best fit (R^2=1; blue trend-line) has been estimated. In Fig. 9d, the inferred initial profile is calculated based on the best fit shown by the blue trend-line. Since Mg# And Al_2O_3 are correlated, the inferred profiles (blue diamonds in Fig. 9b,d) can be taken as growth profiles. Such an analysis implies that crystal profiles showing a good match between measured and inferred profiles (e.g. Fig. 9b) have been little, or not at all, affected by diffusion. On the other hand, crystal profiles showing differences between measured and inferred profiles (e.g. Fig. 9d) have been affected by diffusion.

Timescale information has been extracted only from crystals showing concentration profiles suitable for diffusion modeling using one of the two methods described above: for example, crystals with profiles belonging to zoning type VIII (Fig. 5h) have not been used for the modeling. Altogether, we applied diffusion modelling to 25 crystals with 50 measured profiles of different Types (Table 1). All calculated timescales are shown in Fig. 10 where it should be borne in mind that timescales obtained using method I are upper limits of residence times in the magmatic

environment ME2, while those obtained using method II are residence times themselves. As seen in the figure, most crystals were amenable to modeling the relaxation of growth zoning using method I, while 10 profiles from 5 crystals, i.e. 2 profiles in mutually perpendicular directions, were suitable for modeling using method II. All of the profiles modelled using method II yielded timescales that were consistent with each other from the mutually perpendicular profiles. These timescales range between 38 and 68 years. Stratigraphically, two of these crystals come from members A1 and B1 and one from member D1. We discuss the implications of these results for the nature of the plumbing system in the following section.

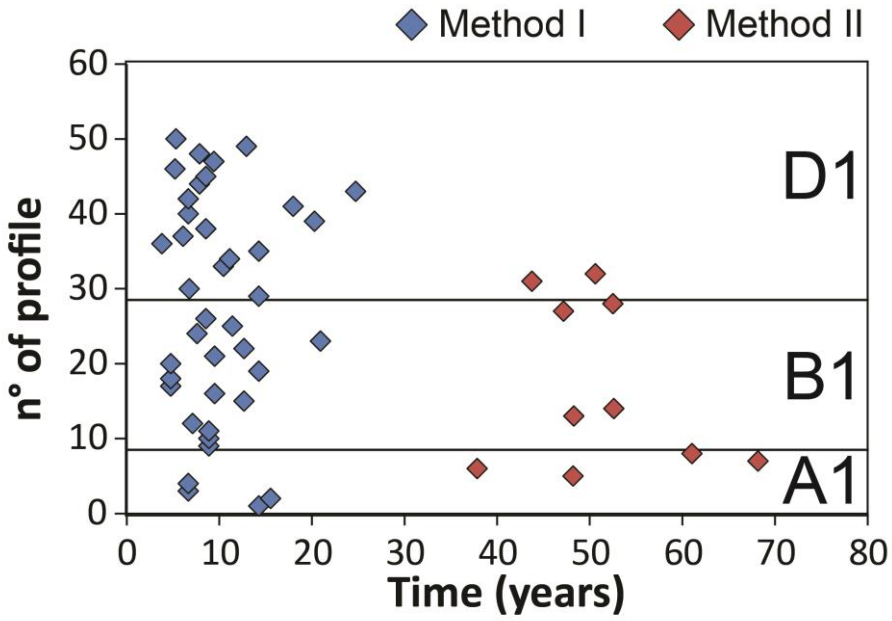

Fig. 10 Output values of times obtained by diffusion modeling on 50 out of 82 analyzed profiles on clinopyroxene crystals. Method I yields the upper limits of residence times of crystals in a magmatic environment; method II yields the residence times of crystals in a magmatic environment.

5 Discussion

5.1 The magmatic plumbing system of Agnano-Monte Spina eruption

Taking into account the composition and temperature, the magmatic environment ME0 can be associated with primitive magmas, especially for the high Mg# (> 91). The ME2 composition (Mg# 78–72) is the most widespread in the volcanic products erupted during all epochs of the Campi

641 Flegrei activity (e.g. de Vita et al., 1999; Munno and Petrosino, 2004; Marianelli et al., 2006; Piochi
642 et al., 2005; Cannatelli et al., 2007; Fedele et al., 2008; Mangiacapra et al., 2008; Arienzo et al.,
643 2010, 2015, 2016; Melluso et al., 2012; Belkin et al., 2016; Forni et al., 2018). This suggests a
644 common magmatic environment for most of the Campi Flegrei clinopyroxenes. Hence, taking into
645 account the estimated T-P, ME2 is ascribable to a crustal reservoir of the Campi Flegrei magmatic
646 system, in which clinopyroxenes with Mg# 78–72 formed. The composition of the ME2 population
647 is the most widespread in the A-MS clinopyroxene crystals, making up 87 % of the homogeneous
648 clinopyroxenes as well as the final, rim compositions of almost all (98 %) zoned crystals (Fig. 3a;
649 Fig. 4). On this basis it is reasonable to interpret the ME2 environment as the physical reservoir in
650 which most of the magmatic interaction(s) took place. In fact, mixing of the ME0 and ME2 melts
651 would produce a magma with intermediate composition, from which clinopyroxenes of composition
652 ME1 (Mg# 84–80) might have grown. The chemical composition of environment ME3 has been
653 found in only 3 out of the total 41 analyzed crystals; being ME3 a different environment, it is
654 characterized by a different set of thermodynamic variables with respect to those of ME2, i.e. it can
655 be characterized by lower temperature (Fig. 7b); since the ME3 composition is more evolved with
656 respect to those of ME2, thus ME3 could represent the most evolved, less-abundant portion of the
657 ME2 magmatic reservoir. Alternatively, the ME3 composition could have been produced by
658 degassing of the ME2 melt, during the stages of magma ascent. Therefore, we can hypothesize that
659 the history recorded in the A-MS clinopyroxene chemical compositions and the behavior of such a
660 plumbing system may be read as illustrated by the schematic diagram shown in Fig. 11: one or more
661 inputs of mafic magma(s) (ME0), originating from partial melting of the mantle, refilled a crustal
662 reservoir already hosting a more evolved resident magma (dominantly ME2, minor ME3), with
663 consequent formation of intermediate compositions (ME1). The isotopic disequilibrium between
664 several A-MS mineral phases and their host rocks (Fig. 5), as already reported in the literature (de
665 Vita et al., 1999; Arienzo et al., 2010), supports such a mixing/mingling process.

666 Since the whole rock and glass composition of A-MS products ranges from trachyte to phonolite,
667 the amount of mafic magma that might have interacted with the evolved resident magma(s) must
668 have been limited. This is in good agreement with what has been already suggested by Arienzo et
669 al. (2010), who modeled the mixing process and proved that less than 10% of a mafic magma with
670 average $^{87}Sr/^{86}Sr \approx 0.70754$ mixed with an evolved one with an average $^{87}Sr/^{86}Sr \approx 0.70749$. This
671 would explain the occurrence of melt inclusions with less differentiated composition in the A-MS
672 clinopyroxenes (Fig. 2a). Such a hypothesis also explains the Sr-isotopic signature of the analyzed
673 A-MS rocks and minerals: both matrix-glass and clinopyroxene crystals from the D-E members,
674 which show a less evolved composition with respect to those from A-B members (Fig. 2a, Fig. 4),
675 are characterized on average by $^{87}Sr/^{86}Sr$ values higher than those of whole rocks and
676 clinopyroxenes from A-B members (Fig. 6). Moreover, the $^{87}Sr/^{86}Sr$ values of feldspars from all the
677 A-MS members are in the range of that of whole rocks from members A-B (Fig. 6a-b); such a Sr-
678 isotopic ratio is the typical Sr-signature of the evolved Campi Flegrei magma component identified
679 by Arienzo et al. (2016). Since this is the most evolved magma component, it can be associated with
680 our ME2 and ME3, while the more mafic magma could be represented by our ME0.
681 The hypothesized recharge scenario (Fig. 11) is also supported by the texture of some crystals,
682 which show resorbed cores (Fig. 5), which is often indicative of disequilibrium due to incorporation
683 within a new host magma (e.g. Ubide et al., 2015, 2019; Astbury et al., 2018; Ubide et Kamber,
684 2018).
685 This kind of mixing behavior is consistent with the nature of the clinopyroxene population as well,
686 where ME0 and ME1, that represent the mafic magma, are statistically far less abundant than
687 clinopyroxenes with ME2 composition.
688 The hypothesized mixing process is also consistent with the observed chemical zoning patterns in
689 the clinopyroxenes. Injection of ME0 mafic magma into the ME2 environment/physical reservoir
690 would produce crystals with cores of ME0 composition (Mg# 92–85) and rims of ME2 composition
691 (Mg# 78–70) and vice versa, as shown by the most common zoning types: Type I and Type V,

692 respectively. Mingling of ME0 and ME2 have probably caused the growth of ME1 composition in
693 the A-MS clinopyroxene, as testified by the somewhat less common Type VII and Type VIII zoning
694 patterns. Oscillations between these compositions (e.g. Type VII) would suggest long lasting
695 connectivity between the reservoirs such that crystals could be transferred from one environment to
696 another, sometimes back and forth. Type III, type IV and type VI zoning pattern (Fig. 5 c, d, f)
697 suggest that crystals can be transferred from ME2 to ME3 environment and vice-versa, i.e. due to
698 partial overturn caused by input of the ME0 melt.
699 Based on the above, we therefore hypothesize that batches of high temperature (~ 1100 °C) mafic
700 magma (ME0) with primitive composition, i.e. very high Mg#, low Ti, Al and Na contents, arrived
701 in a magma reservoir (Fig. 11a) where they partially mixed with a pre-existing more evolved
702 magma (ME2), leading to the formation of intermediate compositions (ME1; Fig. 11b). The mafic
703 input could have caused perturbation in a zoned reservoir and promoted interaction between the
704 chemically different magmatic portions (ME2-ME3; Fig. 11c).
705 Since ME3 has been found only in member B1, it probably represents the most evolved least-
706 abundant portion of the A-MS magmas erupted during the first Plinian phase of the eruption.
707 Furthermore, as a greater number of high Mg# core crystals are present in D1 compared to A1 and
708 B1 members, we hypothesize that the magma which led to the eruption of the second main fallout
709 deposit (D1), may have resided near the floor of the ME2 reservoir and may have been more
710 affected by the ME0 batches of mafic magmas, likely deeper, although good barometric constraints
711 are not available. However, few barometric estimates show pressures >3 kbar (Fig. 7b), implying
712 that some clinopyroxenes from ME0 could have started crystallizing at higher pressures. Moreover,
713 some crystal cores have higher Na_2O and Al_2O_3 contents (Fig. 3b-c), which could reflect
714 crystallization under higher pressure (e.g. Nimis, 1995; Putirka, 2008).These pressure values also
715 agree with estimates obtained from previous studies on the A-MS (Roach, 2005; Arienzo et al.,
716 2010; Iovine et al., 2017a) and the PVD crystallization pressures (Perinelli et al., 2019; Bonechi et
717 al., 2020).

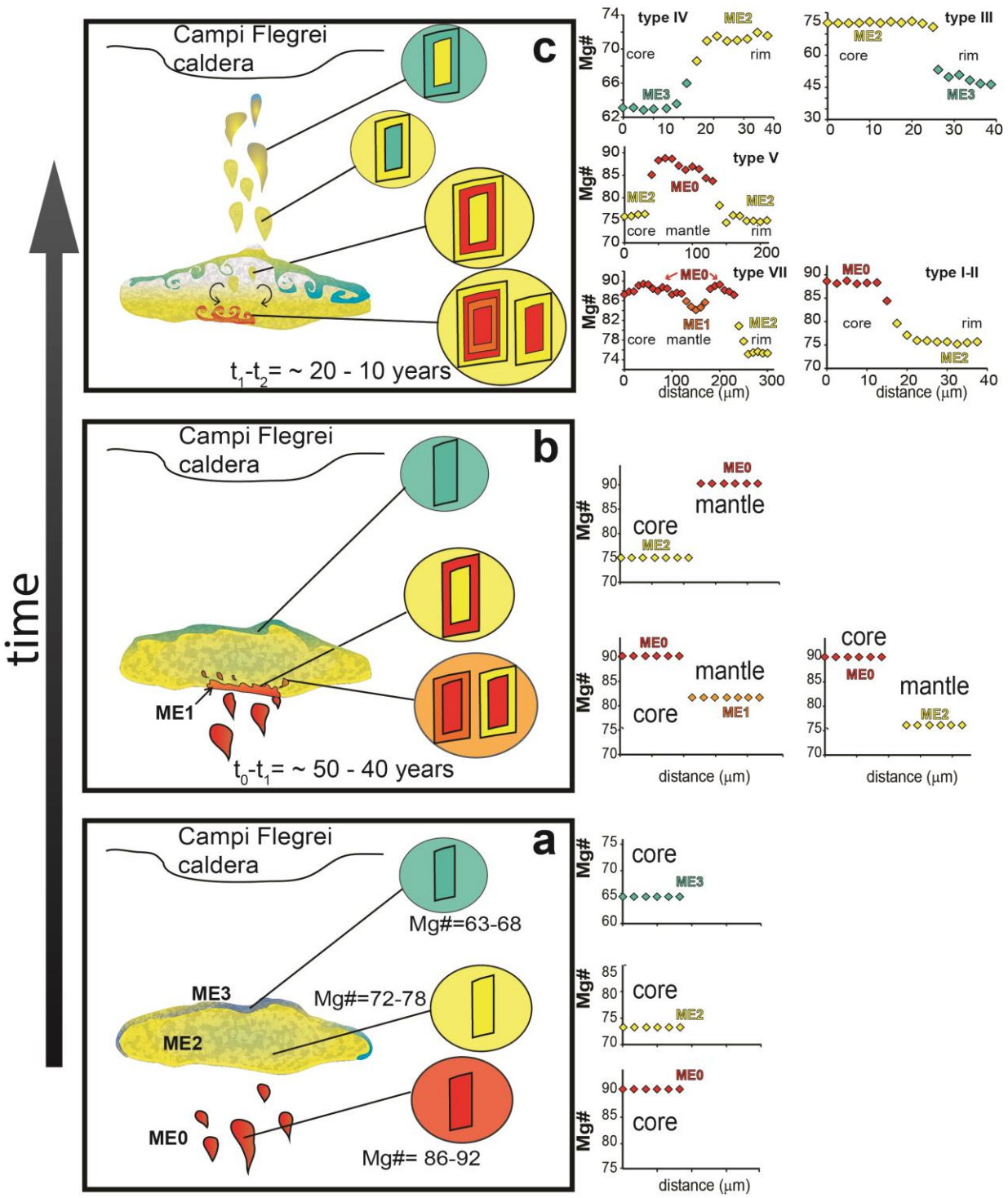

Fig. 11 Schematic sketch illustrating the magmatic processes occurred in the A-MS plumbing system. a) three distinct magmatic environments at a t = 0: one (ME0), in red, in which core of clinopyroxenes with high Mg# (92–85) were formed, is associated with primitive magmas; an environment (ME2), in yellow, ascribable to a crustal reservoir of the Phlegraean magmatic system, in which core of clinopyroxenes with Mg#78–70 were formed and an environment (ME3), in blue, identifiable with a less abundant, most differentiated magma portion of the ME2 reservoir. b) The interaction between ME0 and ME2 explains the normal zoning for clinopyroxenes of ME0 and, conversely, the reverse zoning for clinopyroxenes of ME2, also leading to the formation of intermediate compositions (ME1). c) The interaction between ME2 and ME3 justifies the whole set of observed zoning patterns in the A-MS

clinopyroxene; t_2-t_1 represents the time span of the mixing events recorded by crystals modeled through method II; t_1-t_0 represents the time span of the recharge events possibly due to increase of mafic magma input recorded by crystals modeled through method I; t_0= time of the eruption.

5.2 Timescales of processes in the Agnano-Monte Spina plumbing system

Diffusion modeling of the chemical zoning profiles provides us temporal constraints on pre-eruptive processes. Overall, the plumbing system that led to the A-MS eruption appears to have been active on decadal timescales. Most types of zoning patterns observed in the clinopyroxene crystals, showing little or no evidence of diffusive modification at the spatial resolution at which the compositions were studied in this work, have presumably recorded the latest phases of the pre-eruptive processes. This allows an upper limit to the duration of their residence in the ME2 magmatic reservoir to be placed and it is on the order of 10–15 years for the majority of the crystals. More specific constraints are provided by a small subset (5) of crystals having high Al-Ti compositions, represented by sub-environments ME1b and ME2b, that record diffusive modification. Al- and Ti- contents tend to show disequilibrium distributions due to their slow diffusivity in the crystals as well as in the melts, and such evolutionary trends as those shown by yellow arrows in Fig. 3d-e have been shown experimentally and empirically to be related to such disequilibrium (e.g. due to high cooling rates; Mollo et al., 2010, 2013; Ubide and Kamber, 2018). Crystals recording such disequilibrium between Al and Mg contents can be used for diffusion modeling. These crystals indicate that a timescale of ~ 40–70 years elapsed between the entrapment of the ME0 crystals into the ME2 reservoir and the eruption. These results explain why diffusive modification can be seen in some crystals and not in others even though they are compositionally almost identical: some of these crystals have resided longer in the crustal reservoir (ME2 environment). The rarity of such crystals, and the fact that back-and-forth transmission between ME0 and ME2 is recorded (e.g. Fig. 8), suggest the following scenario: a long lived connectivity existed between the ME0 and ME2 environments over several decades such that crystals could be

752 transferred back and forth. Only a few crystals resided in the ME2 reservoir for several decades.
753 These were erupted when the extent of ME0 magma input considerably increased, as recorded by
754 the major population of zoned crystals, within 10–15 years before the eruption.
755 Fig. 11 also explains the systematics of zoning pattern shown in Fig. 4 and Fig. 8. At the start of the
756 eruption (member A), likely triggered by increased input of mafic magma, crystals from the main
757 ME2 reservoir with cores of ME0 and rims of ME2 are erupted. Subsequently, as the reservoir is
758 gradually emptied, more and more crystals with cores of ME2, mantles of ME0-ME1 and rims of
759 ME2 are erupted (member B). At this stage, increased degassing may have produced more ME3
760 crystals as well. With progressive eruption, magma from the deeper, less evolved reservoir made its
761 way directly to the surface, with an increased contribution of less evolved melts as well as
762 clinopyroxene crystals (member D). In the course of the eruption then the ME2 reservoir was
763 partially or completely emptied, establishing a direct link between the more primitive environment
764 and the eruptive conduit during the later stages of the eruption (i.e. D1).
765
766
767 **5.3 Comparison with results of other timescale calculations for the Campi Flegrei caldera**
768 Although constraints on depths of the magmatic environments that were identified based on the
769 systems analysis of compositional zoning in clinopyroxenes are poor, we can use results from other
770 studies (e.g. Zollo et al., 2008; Arienzo et al., 2010; Pappalardo and Mastrolorenzo, 2012; Arzilli et
771 al., 2016; Di Vito et al., 2016; Zdanowic et al., 2016; Fedi et al., 2018; Voloschina et al., 2018) that
772 used different geological, geochemical or geophysical information to tentatively associate the
773 magmatic environments to reservoirs at different depths. It is possible that the deeper reservoir at
774 >10 km depth inferred in those studies is primarily associated with the less evolved ME0
775 environment while the shallower reservoir at < 8 km is primarily associated with the dominant ME2
776 reservoir. The overall assembly of eruptible magma which fed large eruptions occurs over relatively
777 long timescales (e.g. ~ 6.4 kyr in the case of the Campanian Ignimbrite eruption; Arienzo et al.,

778 2011) but processes within magmatic plumbing systems occur on a hierarchy of shorter timescales.
779 The timescales of different processes that occurred in the plumbing system of Campi Flegrei have
780 been determined using a variety of methods (e.g. Arienzo et al., 2011; Pappalardo and
781 Mastrolorenzo, 2012; Montagna et al., 2015; Perugini et al., 2015; Wu et al., 2015; Arzilli et al.,
782 2016; Di Vito et al., 2016; Iovine et al., 2017; Astbury et al., 2018). Various lines of evidence point
783 to the fact that degassing of rising magma plays an important role in the system (Mastrolorenzo and
784 Pappalardo, 2006; Montagna et al., 2015; Chiodini et al., 2016; Astbury et al., 2018; Forni et al.,
785 2018) and that a short-lived episode of enhanced degassing occurs over hours to days before an
786 eruption (e.g. Arzilli et al., 2016; Astbury et al., 2018; Pappalardo and Mastrolorenzo, 2012;
787 Montagna et al., 2015). Such a transient (and hence less frequently recorded), degassed magmatic
788 environment could be represented by ME3, for example. Note that such degassing promotes
789 crystallinity (e.g. Moretti et al., 2014; Arzilli et al., 2016), which may have produced the ME3
790 composition clinopyroxenes as well as the microlites that record a history of a few hours to days.
791 Comparable or even more rapid timescales have been obtained for magma mingling processes in the
792 Campi Flegrei magmatic system (e.g. tens of minutes; Perugini et al., 2015). As melts move
793 between these reservoirs, they adapt to the local magmatic environment (i.e. new P, T oxygen
794 fugacity, partial pressure of fluids) almost instantaneously. However, the crystal cargo of such melts
795 would require much longer to adapt to the new conditions, and the residence times of crystals of
796 different minerals have been consistently found to be on the order of decades or even longer using a
797 variety of minerals and methods, e.g. < 60 years based on Ba-zoning in sanidine (Iovine et al.,
798 2017); few centuries for the coarsest feldspar crystals based on CSD (Pappalardo and
799 Mastrolorenzo, 2012); few years to decades based on CSD of some microlites (Wu et al., 2015) and
800 zoning in clinopyroxene (this study).
801 These may be considered in the context of the plumbing system connectivity and timescales
802 inferred above to develop an integrated picture. Taken together, this information would be
803 consistent with a system where a long-lived magma reservoir at depths of >10 km containing a

804 shoshonitic-latitic magma, corresponding to ME0 of this study, is connected to a shallower (< 8 km)
805 reservoir containing a more evolved magma (e.g. trachyte), corresponding to ME2 of this study,
806 over decadal, or even century, timescales. Entry of the more mafic magma in the more evolved
807 reservoir/mush zone could lead to melting/assimilation and mixing, leading to the formation of a
808 reservoir such as ME1 (Fig. 11). Melts transported from one environment to another mingle rapidly
809 on timescales of minutes (Perugini et al., 2015) while their crystal cargoes retain their identities in
810 the form of compositional zoning. Progressive degassing, whose rate increases a few hours to days
811 before eruption, may lead to the formation of a transient environment ME3 (Fig. 11). Such a
812 scenario could be consistent, for example, with the record of unrest from 1251 AD – 1538 AD
813 before the 1538 AD eruption at Campi Flegrei (Di Vito et al., 2016). Before that eruption, the
814 system evolved over ~ 300 years and major changes occurred a couple of years before the eruption.
815

816 ## 6 Conclusions

817 In this work, the complex zoning patterns shown by clinopyroxene crystals from the A-MS eruption
818 have been characterized. Despite the complex sequential zoning testified by the wide chemical
819 variation and the great variability of zoning types, some transitions inside the zoning pattern are
820 prevalent suggesting a common late evolutionary history. A population-based approach allows us to
821 identify several magmatic environments in which clinopyroxenes sequentially grew. Quantification
822 of connectivity and their frequencies allow us to infer the pattern of magma movement among the
823 different magmatic environments. The timescales of such movement have been constrained by
824 diffusion modeling.
825 The textural features and the chemical composition of the A-MS clinopyroxenes record the
826 existence of at least two main, likely physically separated, magmatic environments that make up the
827 A-MS plumbing system: the first of these (ME0), identified in clinopyroxene crystals with very
828 high Mg# (>91), is representative of mafic magma that presumably directly originated from partial
829 melting of the local mantle source; the second, dominant magmatic environment is represented by

clinopyroxene crystals showing more evolved compositions (ME2: Mg# = 78–70) associated with trachytic and phonolitic magmas that were likely stationed in a shallower crustal reservoir. Mingling of magma from these two environments could have produced an intermediate environment (ME1; Mg#= 84–80). These magmatic environments were connected with each other with transfer of magma between them over decadal, and perhaps even centennial, timescales. More evolved environments (e.g. ME3: Mg#= 69–60) could have appeared as a result of degassing-induced crystallization shortly (e.g. days to hours) before eruption.

The proposed scenario provides guidance for evaluating future volcanic hazards. Our results suggest that mafic recharge of an evolved shallow reservoir can last for decades. During the latest phase, enhanced input of mafic magma could have destabilized the magmatic system and, combined with the associated degassing, could have favored the trigger of the eruption. In other words, input of mafic magma by itself does not trigger eruptions; eruptions are triggered only when a threshold is exceeded such that degassing and related events are set in motion. This study highlights the complex relationships between events of magma recharge/mixing and onset of the eruption. This knowledge, when integrated with information provided by other case-studies worldwide to build a behavioral model of similar active volcanoes, is useful for risk assessment.

Acknowledgments

The method for the evaluation of the effective occurrence of diffusion has been developed by Dr. Ralf Dohmen. The authors are grateful to Dr. Manuela Nazzari (INGV-Roma1) for her availability and help in the acquisition of microanalytical data. The authors gratefully acknowledge Hélène Balcone-Boissard, Teresa Ubide and an anonymous reviewer, as well as the Executive Editor of Geochimica et Cosmochimica Acta, who provided constructive suggestions and comments that substantially improved the manuscript. Aitor Cambeses acknowledges the research grant provided by the Alexander von Humboldt Foundation for a post-doctoral fellowship at Bochum. The INGV-OV laboratories have been financially supported by the EPOS Research Infrastructure through the

contribution of the Italian Ministry of University and Research (MUR). This work has been partially developed during the "Timescales of magmatic processes", a project involving collaboration between INGV (Istituto Nazionale di Geofisica e Vulcanologia), the Department of Earth, Environment and Resources Sciences of the University of Naples Federico II and the Institute of Geology, Mineralogy und Geophysics of the Ruhr-Universität (Bochum, Germany).

Funding: This work was supported by the Research Grants - Short-Term Grants, 2019 (57442045) scholarship provided by the DAAD (Deutscher Akademischer Austauschdienst) organization.

References

Acocella V., Salvini F., Funiciello R., and Faccenna C. (1999) The role of transfer structures on volcanic activity at Campi Flegrei (southern Italy). J. Volcanol. Geotherm. Res. 91, 123 – 139.

Acocella V. and Funiciello R. (2006) Transverse systems along the extensional Tyrrhenian margin of central Italy and their influence on volcanism. Tectonics. 25, 1-24. TC2003. doi:10.1029/2005TC001845

Alves A., Janasi V.D., Simonetti A. and Heaman L. (2009) Microgranitic enclaves as products of self-mixing events: a study of open-systemprocesses in the Mauà granite, São Paulo, Brazil, based on in situ isotopic and trace elements in plagioclase. J Petrol. 50, 2221-2247. doi:10.1093/petrology/egp074.

Arienzo I., Civetta L., Heumann A., Wörner G. and Orsi G. (2009) Isotopic evidence for open system processes within the Campanian Ignimbrite magma chamber. Bull. Volcanol. 71, 285–300.

878 Arienzo I. Moretti R. Civetta L. Orsi G. and Papale P. (2010) The feeding system of Agnano-
879 Monte Spina eruption (Campi Flegrei, Italy): dragging the past into the present
880 activity and future scenarios. Chem. Geol. 270, 135–147
881 Arienzo I., Neumann A., Wörner G., Civetta L. and Orsi G. (2011) Processes and timescales of
882 magma evolution prior to the Campanian ignimbrite eruption (Campi Flegrei, Italy).
883 Earth Planet. Sci. Lett. 306 (3–4), 217–228.
884 Arienzo I., Carandente A., Di Renzo V., Belviso P., Civetta L., D'Antonio M. and Orsi G.,
885 (2013) Sr and Nd isotope analysis at the Radiogenic Isotope Laboratory of the
886 Istituto Nazionale di Geofisica e Vulcanologia Sezione di Napoli - Osservatorio
887 Vesuviano. Rapporti Tecnici INGV. 260, 1–18. (available online at
888 http://istituto.ingv.it/lingv/produzionescientifica/rapporti-tecnici-
889 ingv/archivio/rapporti-tecnici-2013/).
890 Arienzo I., D'Antonio M., Di Renzo V., Tonarini S., Minolfi G., Orsi G., Carandente A., Belviso
891 P. and Civetta L. (2015) Isotopic microanalysis sheds light on the magmatic
892 endmembers feeding volcanic eruptions: the Astroni 6 case study (Campi Flegrei
893 Italy). J. Volcanol. Geotherm. Res. 304, 24–37.
894 Arienzo I., Mazzeo FC., Moretti R., Cavallo A. and D'Antonio M. (2016) Open-system magma
895 evolution and fluid transfer at Campi Flegrei caldera (Southern Italy) during the past
896 5 ka as revealed by geochemical and isotopic data. The example of the Nisida
897 eruption. Chem. Geol. 427, 109–124.
898 Arzilli F., Piochi M., Mormone A., Agostini C. and Carroll M.R. (2016) Constraining pre-
899 eruptive magma conditions and unrest timescales during the Monte Nuovo eruption
900 (1538 AD; Campi Flegrei Southern Italy): integrating textural and CSD results from
901 experimental and natural trachy-phonolites. Bull. Volcanol. 78 doi:101007/s00445-
902 016-1062-z

903 Astbury R.L., Petrelli M., Ubide T., Stock M.J., Arienzo I., D'Antonio M. and Perugini D. (2018)
904 Tracking plumbing system dynamics at the Campi Flegrei caldera Italy: high-
905 resolution trace element mapping of the Astroni crystal cargo. Lithos. 318–319, 464–
906 477.
907 Beccaluva L., Di Girolamo P. and Serri G., (1991) Petrogenesis and tectonic setting of the
908 Roman volcanic province Italy. Lithos. 26, 191–221. doi:101016/0024-
909 4937(91)90029-K
910 Belkin H.E., Rolandi G., Jackson J.C., Cannatelli C., Doherty A.L., Petrosino P. and De Vivo B.
911 (2016) Mineralogy and geochemistry of the older (> 40ka) ignimbrites on the
912 Campanian Plain, southern Italy. J. Volcanol. Geotherm. Res. 323, 1-18.
913 Bevilacqua A., Isaia R., Neri A., Vitale S., Aspinall W.P., Bisson M., Flandoli F., Baxter P.J.,
914 Bertagnini A., Esposti Ongaro T., Iannuzzi E., Pistolesi M. and Rosi M. (2015)
915 Quantifying volcanic hazard at Campi Flegrei caldera (Italy) with uncertainty
916 assessment: I Vent opening maps. J. Geophys. Res. 120, 2309– 2329.
917 doi:101002/2014JB011775
918 Bevilacqua A., Flandoli F., Neri A., Isaia R. and Vitale S. (2016) Temporal models for the
919 episodic volcanism of Campi Flegrei caldera (Italy) with uncertainty quantification.
920 J. Geophys. Res.. 121, 7821–7845. doi:101002/2016JB013171
921 Bevilacqua A., Neri A., Bisson M., Esposti Ongaro T., Flandoli F., Isaia R., Rosi M. and Vitale
922 S., (2017) The effects of vent location, event scale and time forecasts on pyroclastic
923 density current hazard maps at Campi Flegrei caldera (Italy). Front. Earth Sci. 5:72.
924 doi:103389/feart201700072
925 Blundy J. and Cashman K. (2008) Petrologic reconstruction of magmatic system variables and
926 processes. Rev. Mineral. Geochem. 69, 179–239. https://doiorg/102138/rmg2008696

927 Bonechi B., Perinelli C. and Gaeta M., (2020) Clinopyroxene growth rates at high-pressure:
928 Constraints on magma recharge of the deep reservoir of the Campi Flegrei Volcanic
929 District (south Italy). Bull. Volcanol. 82, 5. doi:10.1007/s00445-019-1342-5
930 Brocchini D., Principe C., Castratori D., Laurenzi M.A. and Gorla L. (2001) Quaternary
931 evolution of the southern sector of the Campanian Plain and early Somma-Vesuvius
932 activity: insights from Trecase 1 well. Mineral. Petrol. 73, 67–91.
933 Cannatelli C., Lima A., Bodnar R.J., De Vivo B., Webster J.D. and Fedele L. (2007).
934 Geochemistry of melt inclusions from the Fondo Riccio and Minopoli 1 eruptions at
935 Campi Flegrei (Italy). Chem. Geol. 237 (3–4), 418–432.
936 Capuano P., Russo G., Civetta L., Orsi G., D'Antonio M. and Moretti R. (2013) The active
937 portion of the Campi Flegrei caldera structure imaged by 3-D inversion of gravity
938 data. Geochem. Geophys. 14, 4681–4697. doi:101002/ggge20276
939 Cashman K.V and Giordano G. (2014) Calderas and magma reservoirs. J. Volcanol. Geotherm.
940 Res. 288, 28–45.
941 Chakraborty S. and Ganguly J. (1992) Cation diffusion in aluminosilicate garnets: experimental
942 determination in spessartine-almandine diffusion couples, evaluation of effective
943 binary diffusion coefficients, and applications. Contrib. Mineral. Petrol. 111, 74–86.
944 Chakraborty S. (2008) Diffusion in silicates: a tool to track timescales of processes comes of age
945 Ann. Rev. Earth Planet. Sci. 36, 153–190.
946 Chamberlain K.J., Morgan D.J. and Wilson C.J.N. (2014) Timescales of mixing and mobilisation
947 in the Bishop Tuff magma body: perspectives from diffusion chronometry.
948 Contrib. Mineral. Petrol. 167, 1034.
949 Chiodini G., Pappalardo L., Aiuppa A. and Caliro S. (2015) The geological CO_2 degassing
950 history of a long-lived caldera. Geology. 43, 767-770. doi:10.1130/G369051.
951 Chowdhury P. and Chakraborty S. (2019) Slow Cooling at Higher Temperatures Recorded
952 within High-P Mafic Granulites from the Southern Granulite Terrain, India:

953 Implications for the Presence and Style of Plate Tectonics near the Archean–
954 Proterozoic Boundary. J. Petrol. 60-3, 441–486, doi:10.1093/petrology/egz001
955 Civetta L., Carluccio E., Innocenti F., Sbrana A. and Taddeucci G. (1991a) Magma chamber
956 evolution at Phlegrean Fields during the last 10 ka, in the light of trace elements and
957 isotope composition. Eur. J. Mineral. 3, 415-428.
958 Cooper K.M. (2019) Time scales and temperatures of crystal storage in magma reservoirs:
959 implications for magma reservoir dynamics. Philos. Trans. Roy. Soc. 377:
960 20180009. doi:101098/rsta20180009
961 Costa F. and Chakraborty S. (2004) Decadal time gaps between mafic intrusion and silicic
962 eruption obtained from chemical zoning patterns in olivine. Earth Planet. Sci. Lett.
963 227, 517–530.
964 Costa F. Dohmen R. and Chakraborty S. (2008) Time scales of magmatic processes from
965 modeling the zoning patterns of crystals. Rev. Mineral. Geochem. 69, 545–594.
966 Crank J. (1975) The Mathematics of Diffusion, 2nd edition, 414 p. Oxford Science Publication,
967 Oxford.
968 D'Antonio M., Civetta L., Orsi G., Pappalardo L., Piochi M., Carandente A., de Vita S., Di Vito
969 M.A. and Isaia R. (1999) The present state of the magmatic system of the Campi
970 Flegrei caldera based on a reconstruction of its behavior in the past 12 ka. J.
971 Volcanol. Geotherm. Res. 91, 247–268. doi:101016/S0377-0273(99)00038-4
972 D'Antonio M., Tonarini S., Arienzo I., Civetta L. and Di Renzo V. (2007) Components and
973 processes in the magma genesis of the Phlegrean Volcanic District, southern Italy.
974 Geol. Soc. Am. 418, 203–220.
975 D'Antonio M. (2011) Lithology of the basement underlying the Campi Flegrei caldera:
976 volcanological and petrological constraints. J. Volcanol. Geotherm. Res. 200, 91–
977 98.

978 Deino A., Orsi G., de Vita S. and Piochi M. (2004) The age of the Neapolitan Yellow Tuff
979 caldera-forming eruption (Campi Flegrei caldera Italy) assessed by $^{40}Ar/^{39}Ar$ dating
980 method. J. Volcanol. Geotherm. Res. 133, 157–170.
981 Del Gaudio C, Aquino I., Ricciardi G.P., Ricco C. and Scandone R. (2010) Unrest episodes at
982 Campi Flegrei: A reconstruction of vertical ground movements during 1905–2009. J.
983 Volcanol. Geotherm. Res. 195, 48–56.
984 Dellino P., Isaia R., La Volpe L. and Orsi G. (2001) Statistical analysis of textural data from
985 complex pyroclastic sequences: implications for fragmentation processes of the
986 Agnano-Monte Spina Tephra (4.1 ka), Phlegraean Fields, southern Italy. Bull.
987 Volcanol. 63, 443–461. doi:101007/s004450100163
988 Dellino P., Isaia R., La Volpe L. and Orsi G. (2004a) Interaction between particles transported by
989 fallout and surge in the deposits of the Agnano–Monte Spina eruption (Campi
990 Flegrei Southern Italy). J. Volcanol. Geotherm. Res. 133, 193–210.
991 doi:101016/S0377-0273(03)00398-6
992 de Vita S., Orsi G., Civetta L., Carandente A., D'Antonio M., Deino A., di Cesare T., Di Vito
993 M.A., Fisher R.V., Isaia R., Marotta E., Necco A., Ort M., Pappalardo L., Piochi M.
994 and Southon J. (1999) The Agnano – Monte Spina eruption (4100 years BP) in the
995 restless Campi Flegrei caldera (Italy). J. Volcanol. Geotherm. Res. 91, 269–301.
996 Dimanov A. and Sautter V. (2000) "Average" interdiffusion of (Fe,Mn)–Mg in natural diopside.
997 Eur. J. Mineral. . 12, 749–760.
998 Di Renzo V., Arienzo I., Civetta L., D'Antonio M., Tonarini S., Di Vito M.A. and Orsi G. (2011)
999 The magmatic feeding system of the Campi Flegrei caldera: architecture and
1000 temporal evolution. Chem. Geol. 281, 227–241.
1001 Di Vito M.A., Isaia R., Orsi G., Southon J., de Vita S., D'antonio M., Pappalardo L. and Piochi
1002 M. (1999) Volcanism and deformation in the past 12 ka at the Campi Flegrei caldera
1003 (Italy). J. Volcanol. Geotherm. Res. 91, 221–246.

1004 Di Vito M.A., Acocella V., Aiello G., Barra D., Battaglia M., Carandente A., Del Gaudio C., de
1005 Vita S., Ricciardi G.P., Ricco C., Scandone R. and Terrasi F. (2016) Magma transfer
1006 at Campi Flegrei caldera (Italy) before the 1538 AD eruption. Sci. Rep. 6, 32245.
1007 Fedele L., Scarpati C., Lanphere M., Melluso L., Morra V., Perrotta A. and Ricci G. (2008) The
1008 Breccia Museo formation, Campi Flegrei southern Italy: geochronology,
1009 chemostratigraphy and relationship with the Campanian Ignimbrite eruption. Bull
1010 Volcanol. 70, 1189–1219.
1011 Fedi M., Cella F., D'Antonio M., Florio G., Paoletti V. and Morra V. (2018) Gravity modeling
1012 finds a large magma body in the deep crust below the Gulf of Naples, Italy. Sci. Rep.
1013 8, 8229. doi:10.1038/s41598-018-26346-z
1014 Forni F., Degruyter W., Bachmann O., De Astis G. and Mollo S. (2018) Long-term magmatic
1015 evolution reveals the beginning of a new caldera cycle at Campi Flegrei. Sci. Adv. 4.
1016 eaat9401. doi: 10.1126/sciadv.aat9401
1017 Gebauer S., Schmitt A.K., Pappalardo L., Stockli D.F. and Lovera O.M. (2014) Crystallization
1018 and eruption ages of Breccia Museo (Campi Flegrei caldera, Italy) plutonic clasts
1019 and their relation to the Campanian Ignimbrite. Contrib. Mineral. Petrol.
1020 doi:10.1007/s00410-013-0953- 7.
1021 Giaccio B., Hajdas I., Isaia R., Deino A. and Nomade S. (2017) High-precision ^{14}C and $^{40}Ar/^{39}Ar$
1022 dating of the Campanian Ignimbrite (Y-5) reconciles the time-scales of climatic-
1023 cultural processes at 40 ka. Sci. Rep. 7:45940. doi: 101038/srep45940
1024 Goldstein S.L, Deines P., Oelkers E.H, Rudnick R.L. and Walter L.M. (2003) Standards for
1025 publication of isotope ratio and chemical data in Chemical Geology. Chem. Geol.
1026 202, 1-4.
1027 Grove T.L. and Bryan W.B. (1983) Fractionation of pyroxene-phyric MORB at low pressure:
1028 and experimental study. Contrib. Mineral. Petrol. 84, 293-209.

1029 Guidoboni E. and Ciuccarelli C. (2011) The Campi Flegrei caldera: historical revision and new
1030 data on seismic crises, bradyseisms, the Monte Nuovo eruption and ensuing
1031 earthquakes (twelfth century 1582 ad). Bull. Volcanol. 73, 655–677.
1032 Humphreys M.C.S., Blundy J.D. and Sparks R.S.J. (2006) Magma evolution and open-system
1033 processes at Shiveluch volcano: insights from phenocryst zoning. J. Petrol. 47,
1034 2303–2334.
1035 Iovine R.S, Fedele L., Mazzeo F.C., Arienzo I., Cavallo A., Wörner G., Orsi G., Civetta L. and
1036 D'Antonio M. (2017a) Timescales of magmatic processes occurred prior to the ~4.7
1037 ka Agnano-Monte Spina eruption (Campi Flegrei caldera Southern Italy) based on
1038 diffusion chronometry on sanidine phenocrysts. Bull. Volcanol. 79,18.
1039 doi:101007/s00445-017-1101-4
1040 Isaia R., D'Antonio M., Dell'Erba F., Di Vito M. and Orsi G. (2004) The Astroni volcano: the
1041 only example of closely spaced eruptions in the same vent area during the recent
1042 history of Campi Flegrei caldera (Italy). J. Volcanol. Geotherm. Res. 133, 171–192.
1043 doi:10.1016/S0377-0273(03)00397-4
1044 Isaia R., Marianelli P. and Sbrana A. (2009) Caldera unrest prior to intense volcanism in Campi
1045 Flegrei (Italy) at 4.0 ka B.P.: implications for caldera dynamics and future eruptive
1046 scenarios. Geophys. Res. Lett. 36:L21303. doi:10.1029/2009GL040513
1047 Jagoutz E., Palme H., Baddenhausen H., Blum K., Cendales M., Dreibus G., Spettel B., Lorentz
1048 V. and Wllnke H., (1979) The abundances of major, minor and trace elements in the
1049 Earth's mantle as derived from primitive ultramafic nodules. Proceedings of the 10th
1050 Lunar and Planetary Science Conference. Geochim. Cosmochim. Acta. Supp. I. 11,
1051 2031-2050.
1052 Jarosewich E., Nelen J.A. and Norberg J.A. (1980) Reference samples for electron microprobe
1053 analysis. Geostandards Newsletter. 4, 43-47. https://doi.org/10.1111/j.1751-
1054 908X.1980.tb00273.x

1055 Kahl M., Chakraborty S., Costa F. and Pompilio M. (2011) Dynamic plumbing system beneath
1056 volcanoes revealed by kinetic modeling and the connection to monitoring data: an
1057 example from Mt Etna. Earth Planet. Sci. Lett. 308, 11–22.
1058 Kahl M., Chakraborty S., Costa F., Pompilio M., Liuzzo M. and Viccaro M. (2013)
1059 Compositionally zoned crystals and realtime degassing data reveal changes in
1060 magma transfer dynamics during the 2006 summit eruptive episodes of Mt. Etna.
1061 Bull. Volcanol. 75, 692. doi:10.1007/s00445-013-0692-7
1062 Kahl M., Chakraborty S., Pompolio M. and Costa F. (2015) Constraints on the nature and
1063 evolution of the magma plumbing system of Mt Etna volcano (1991–2008) from a
1064 combined thermodynamic and kinetic modeling of the compositional record of
1065 minerals. J. Petrol. 56, 2025–2068.
1066 Kahl M., Viccaro M., Ubide T., Morgan D.J. and Dingwell D.B. (2017) A branched magma
1067 feeder system during the 1669 eruption of Mt Etna: evidence from a time-integrated
1068 study of zoned olivine phenocryst populations. J. Petrol. 58, 443–472.
1069 Liedl A., Buono G., Lanzafame G., Dabagov S.B., Della Ventura G., Hampai D., Mancini L.,
1070 Marcelli A. and Pappalardo L. (2019) 3D imaging textural characterization of
1071 pyroclastic products from the 1538 AD Monte Nuovo eruption (Campi Flegrei,
1072 Italy). Lithos. 340–34.: 316-331. doi:10.1016/j.lithos.2019.05.010.
1073 Lustrino M., Marturano A., Morra V. and Ricci G. (2002) Volcanological and geochemical
1074 features of young pyroclstic levels (b12 ka) in the urban area of Naples (S Italy).
1075 Period. di Mineral. 71(3), 241–253.
1076 Mangiacapra A., Moretti R., Rutherford M., Civetta L., Orsi G. and Papale P. (2008) The deep
1077 magmatic system of the Campi Flegrei caldera (Italy). Geophys. Res. Lett. 35,
1078 L21304. doi:101029/2008GL035550

1079 Mangler M.F., Petrone C.M., Hill S., Delgado-Granados H. and Prytulak J. (2020) A pyroxenic
1080 view on magma hybridization and crystallization at Popocatepetl Volcano, Mexico.
1081 Front. Earth Sci. 8, 362. doi:10.3389/feart.2020.00362
1082 Marianelli P., Sbrana A. and Proto M. (2006) Magma chamber of the Campi Flegrei
1083 supervolcano at the time of eruption of the Campanian Ignimbrite. Geology. 34(11),
1084 937– 940. doi: 10.1130/G22807A.1
1085 Masotta M., Mollo S., Freda C., Gaeta M. and Moore G. (2013) Clinopyroxene–liquid
1086 thermometers and barometers specificto alkaline differentiated magmas. Contrib.
1087 Mineral. Petrol. 166, 1545–1561. doi:101007/s00410-013-0927-9
1088 Mastrolorenzo G. and Pappalardo L. (2006) Magma degassing and crystallization processes
1089 during eruptions of high-risk Neapolitan volcanoes. Evidence of common
1090 equilibrium rising processes in alkaline magmas. Earth Planet. Sci. Lett. 250, 164–
1091 181.
1092 Mastrolorenzo G., Palladino D.M., Pappalardo L. and Rossano S. (2017) Probabilistic-Numerical
1093 assessment of pyroclastic current hazard at Campi Flegrei and Naples city: Multi-
1094 VEI scenarios as a tool for “full-scale” risk management. PLoS One.
1095 doi.org/10.1371/journal.pone.0185756
1096 Mazzeo F.C., D'Antonio M., Arienzo I., Aulinas M., Di Renzo V. and Gimeno D. (2014)
1097 Subduction-related enrichment of the Neapolitan volcanoes (Southern Italy) mantle
1098 source: new constraints on the characteristics of the slab-derived components. Chem.
1099 Geol. 386, 165-183.
1100 Mele D., Dioguardi F., Dellino P., Isaia R., Sulpizio R. and Braia G. (2015) Hazard of
1101 pyroclastic density currents at the Campi Flegrei Caldera (Southern Italy) as deduced
1102 from the combined use of facies architecture physical modelingand statistics of the
1103 impact parameters. J. Volcanol. Geotherm. Res. 299, 35–53.
1104 doi:101016/jjvolgeores201504002

Melluso L., de'Gennaro R., Fedele L., Franciosi L. and Morra V. (2012) Evidence of crystallization in residual, Cl–F-rich, agpaitic, trachyphonolitic magmas and primitive Mg-rich basalt–trachyphonolite interaction, in the lava domes of the Phlegrean Fields (Italy). Geol. Mag. 149, 532–550.

Mollo S., Del Gaudio P., Ventura G., Iezzi G. and Scarlato P, (2010) Dependence of clinopyroxene composition on cooling rate in basaltic magmas: implications for thermobarometry. Lithos. 118, 302–312.

Mollo S., Putirka K., Misiti V., Soligo M. and Scarlato P. (2013) A new test for equilibrium based on clinopyroxene-melt pairs: clues on the solidification temperatures of Etnean alkaline melts at post-eruptive conditions. Chem. Geol. 352, 92–100. https ://doi.org/10.1016/j.chemg eo.2013.05.026.

Montagna C.P., Papale P. and Longo A. (2015) Timescales of mingling in shallow magmatic reservoirs. Geol. Soc. Spec. Publ. 422, 131-140. doi:10.1144/SP422.6.

Morabito S., Petrosino P., Milia A., Sprovieri M. and Tamburrino S. (2014) A multidisciplinary approach for reconstructing the stratigraphic framework of the last 40 ka in a bathyal area of the eastern Tyrrhenian Sea. Glob. Planet. Change. 123, 121-138.

Moretti R., Arienzo I., Orsi G., Civetta L. and D'Antonio M. (2013) The deep plumbing system of Ischia: a physico-chemical window on the fluid-saturated and CO_2-sustained Neapolitan volcanism (southern Italy). J. Petrol. 54, 951-984.

Moretti R., Arienzo I., Civetta L., Orsi G. and Papale P. (2013) Multiple magma degassing sources at an explosive volcano. Earth Planet. Sci. Lett. 367, 95-104. doi:10.1016/j.epsl.2013.02.013; ISSN: 0012-821X

Moretti R., Troise C., Sarno F. and De Natale G. (2018) Caldera unrest driven by CO2-induced drying of the deep hydrothermal system. Sci. Rep. 8 (1), 8309.

Moretti R., Arienzo I., Di Renzo V., Orsi G., Arzilli F., Brune F., D'Antonio M., Mancini L. and Deloule E. (2019) Volatile segregation and generation of highly vesiculated

explosive magmas by volatile-melt fining processes: The case of the Campanian Ignimbrite eruption. Chem. Geol. 503, 1-14.

Morgan D.J., Blake S., Rogers N.W., De Vivo B., Rolandi G., Macdonald R. and Hawkesworth J. (2004) Timescales of crystal residence and magma chamber volume from modelingof diffusion profiles in phenocrysts: Vesuvius 1944. Earth Planet. Sci. Lett. 222, 933–946.

Müller T., Dohmen R., Becker H.W., ter Heege J. and Chakraborty S. (2013) Fe–Mg interdiffusion rates in clinopyroxene: experimental data and implications for Fe–Mg exchange geothermometers. Contrib. Mineral. Petrol. 166,1563–1576.

Munno R. and Petrosino P. (2004) New constraints on the occurrence of Y-3 upper Pleistocene tephra marker layer in the tyrrhenian sea. Il Quaternario, Italian Journal of Quaternary Sciences. 17, 11-20

Nimis P. (1995) A clinopyroxene geobarometer for basaltic systems based on crystal-structure modeling. Contrib. Mineral. Petrol. 121, 115-125.

Orsi G., de Vita S. and Di Vito M.A. (1996) The restless, resurgent Campi Flegrei nested caldera (Italy): constraints on its evolution and configuration. J. Volcanol. Geotherm. Res. 74, 179-214.

Orsi G., de Vita S., Di Vito M., Isaia R., Nave R. and Heiken G. (2003) Facing volcanic and related hazards in the Neapolitan Area. In: Heiken, G., Fakundiny, R. & Sutter, J. (eds). Earth Science in the Cities: a Reader. Washington, DC. AGU, 121-170.

Orsi G., Di Vito M.A. and Isaia R. (2004) Volcanic hazard assessment at the restless Campi Flegrei caldera. Bull. Volcanol. 66, 514–530.

Orsi G., Di Vito M.A., Selva J. and Marzocchi W. (2009) Long-term forecast of eruption style and size at Campi Flegrei caldera (Italy). Earth Planet. Sci. Lett.. 287, 265–276.

Pappalardo L., Civetta L., D'Antonio M., Deino A., Di Vito M., Orsi G., Carandente A., de Vita S., Isaia R. and Piochi M. (1999) Chemical and Sr- isotopical evolution of the

1157 Phlegrean magmatic system before the Campanian Ignimbrite and the Neapolitan
1158 Yellow Tuff eruptions. J. Volcanol. Geotherm. Res. 91, 141-166.
1159 Pappalardo L., Piochi M., D'Antonio M., Civetta L. and Petrini R. (2002) Evidence for
1160 multistage magmatic evolution during the past 60 kyr at Campi Flegrei (Italy)
1161 deduced from Sr, Nd and Pb isotope data. J. Petrol. 43, 1415-1434.
1162 Pappalardo L., Ottolini L. and Mastrolorenzo G. (2008) The Campanian Ignimbrite (Southern
1163 Italy) geochemical zoning, insight on the generation of a super-eruption from
1164 catastrophic differentiation and fast withdrawal. Contrib. Mineral. Petrol. 156, 1–26.
1165 Pappalardo L. and Mastrolorenzo G. (2012) Rapid differentiation in a sill-like magma reservoir:
1166 a case study from the campi flegrei caldera. Sci. Rep. 2:712. doi:101038/srep00712
1167 Pappalardo L. and Buono G. (2021) Insights into processes and timescales of magma storage and
1168 ascent from textural and geochemical investigations, in: Masotta, M., Beier, C.,
1169 Mollo, S. (Eds.), Crustal Magmatic System Evolution. AGU (American Geophysical
1170 Union) Monograph. 213-235. https://doi.org/10.1002/9781119564485.ch10.
1171 Perinelli C., Gaeta M., Bonechi B., Granati S.F., Freda C., D'Antonio M., Stagno V., Sicola S.
1172 and Romano C. (2019) Effect of water on the phase relations of primitive K-basalts:
1173 Implications for high-pressure differentiation in the Phlegraean Volcanic District
1174 magmatic system. Lithos .342, 530–541.
1175 Perugini D., De Campos C.P., Petrelli M. and Dingwell D.B. (2015) Concentration variance
1176 decay during magma mixing: a volcanic chronometer, Sci. Rep 5, 14225.
1177 doi:101038/srep14225
1178 Petrone C., Bugatti G., Braschi E. and Tommasini S.. (2016) Pre-eruptive magmatic processes
1179 re-timed using a non-isothermal approach to magma chamber dynamics. Nature
1180 Communication. 7, 12946. doi:10.1038/ncomms12946
1181 Piochi M., Bruno P.P. and De Astis G. (2005) Relative roles of rifting tectonics and magma
1182 ascent processes: inferences from geophysical, structural, volcanological, and

1183 geochemical data for the Neapolitan volcanic region (southern Italy). Geochem.
1184 Geophys. 6, Q07005 doi:10,1029/2004GC000885
1185 Putirka K., Ryerson F.J. and Mikaelian H. (2003) New igneous thermobarometers for mafic and
1186 evolved lava compositions, based on clinopyroxene+liquid equilibria. Am. Min. 88,
1187 1542–1554.
1188 Putirka K.D. (2008) Thermometers and barometers for volcanic systems. Rev. Mineral.
1189 Geochem. 69, 61–120.
1190 Roach A.L. (2005) The Evolution of Silicic Magmatism in the Post-Caldera Volcanism of the
1191 Phlegrean Fields, Italy. PhD thesis. Brown University, Providence, USA.
1192 Romano C., Vona A., Campagnola S., Giordano G., Arienzo I. and Isaia R. (2020) Modeling
1193 and physico-chemical constraints to the 4.5 ka Agnano-Monte Spina Plinian eruption
1194 (Campi Flegrei, Italy). Chem. Geol. 532. 119301.
1195 Saunders K., Blundy J., Dohmen R. and Cashman K. (2012) Linking petrology and seismology
1196 at an active volcano. Science. 336, 1023–1027.
1197 Sautter V., Jaoul O. and Abel F. (1988) Aluminum diffusion in diopside using the ^{27}Al (p, γ) ^{28}Si
1198 nuclear reaction: preliminary results. Earth Planet. Sci. Lett. 89, 109-114.
1199 Scarpati C., Perrotta A., Lepore S. and Calvert A. (2013) Eruptive history of Neapolitan
1200 Volcanoes: Constrains from ^{40}Ar-^{39}Ar dating. Geol. Mag. 150(3), 412–425.
1201 Selva J., Orsi G., Di Vito M.A., Marzocchi W. and Sandri L. (2012) Probability hazard map for
1202 future vent opening at the Campi Flegrei caldera (Italy), Bull Volcanol. 74, 497–510.
1203 Smith V.C., Isaia R. and Pearce N.J.G. (2011) Tephrostratigraphy and glass compositions of
1204 post-15 ka Campi Flegrei eruptions: implications for eruption history and
1205 chronostratigraphic markers. Quat. Sci. Rev. 30, 3638–3660.
1206 doi:101016/jquascirev201107012.
1207 Solaro C., Balcone-Boissard H., Morgan D.J., Boudon G., Martel C. and Ostorero L. (2020) A
1208 system dynamics approach to understanding the deep magma plumbing system

beneath Dominica (Lesser Antilles). Front. Earth Sci. 8:574032. doi: 10.3389/feart.2020.574032

Sparks R.S.J. and Cashman K.V. (2017) Dynamic magma systems: implications for forecasting volcanic activity. Elements. 13, 35–40. doi: 10.2113/gselements.13.1.35.

Tonarini S., Leeman W.P., Civetta L., D'Antonio M., Ferrara G. and Necco A. (2004) B/Nb and $\delta^{11}B$ systematics in the Phlegrean Volcanic District, Italy. J. Volcanol. Geotherm. Res. 133, 123–139.

Trepmann C.A., Stöckhert B. and Chakraborty S. (2004) Oligocene trondhjemitic dikes in the Austroalpine basement of the Pfunderer Berge Südtirol – level of emplacement and metamorphic overprint. Eur. J. Mineral. 16, 641–659. doi:101127/0935-1221/2004/0016-0641

Turner S. and Costa F. (2007) Measuring timescales of magmatic evolution. Elements. 3, 267-272.

Ubide T., McKenna C.A., Chew D.M. and Kamber B.S. (2015) High-resolution LA-ICP-MS trace element mapping of igneous minerals: in search of magma histories. Chem. Geol. 409, 157–168. doi:101016/jchemgeo201505020

Ubide T. and Kamber B. (2018) Volcanic crystals as time capsules of eruption history. Nat. Commun. 9, 326–326. doi:101038/s41467-017-02274-w.

Ubide T., Mollo S., Zhao J.X., Nazzari M. and Scarlato P. (2019) Sector zoned clinopyroxene as a recorder of magma history, eruption triggers, and ascent rates. eochim. Cosmochim. Acta. 251, 265–283. doi:101016/jgca201902021.

Voloschina M., Pistolesi M., Bertagnini A., Métrich N., Pompilio M, Di Roberto A., Di Salvo S., Francalanci L., Isaia R., Cioni R. and Romano C. (2018) Magmatic reactivation of the Campi Flegrei volcanic system: insights from the Baia–Fondi di Baia eruption. Bull. Volcanol. 80, 75. doi:10.1007/s00445-018-1247-8

Wu Wan N., Schmitt Axel K. and Pappalardo L., (2015) U-Th baddeleyite geochronology and its significance to date the emplacement of silica undersaturated magmas. Am. Mineral. 100, 2082–2090.

Zdanowicz G., Boudon G., Balcone-Boissard H., Cioni R., Mundula F., Orsi G., and Civetta L. (2016) The sub-Plinian Greenish Pumice eruption (19,065±105 yr cal BP) of Mount Somma – Vesuvius. Geochemical and textural constrains., EGU General Assembly 2016, 17 April–22 Apr 2016, EGU2016-6940, 2016

Zellmer G.F., Blake S., Vance D., Hawkesworth C. and Turner S., (1999) Plagioclase residence times at two island arc volcanoes (Kameni Islands, Santorini and Soufriere St Vincent) determined by Sr diffusion systematic. Contrib. Mineral. Petrol. 136, 345–357.

Zellmer G.F., Sparks R.S.J, Hawkesworth C. and Wiedenbeck M. (2003) Magma emplacement and remobilization timescales beneath Montserrat: insights from Sr and Ba zonation in plagioclase phenocrysts. J. Petrol. 44, 1413-1431.

Zollo A., Maercklin N., Vassallo M., Dello Iacono D., Virieux J. and Gasparini P. (2008) Seismic reflections reveal a massive melt layer feeding Campi Flegrei caldera. Geophys. Res. Lett. 35, L12306. doi:10.1029/2008GL034242

Figures

Fig. 1 a) Geological and structural sketch map of the Southern Campania Plain (modified after Orsi et al., 2003). b) Areal distribution of the A-MS volcanic deposits (redrawn after de Vita et al., 1999. c) Detail of the Agnano-San Vito area (modified after Iovine et al., 2017a) d) Schematic stratigraphic column of the A-MS erupted products, subdivided into various members (modified after Iovine et al., 2017a).; in brackets we reported the number of samples collected from each sub-member.

Fig. 2 a) Glass compositions of A-MS products plotted in the Total Alkali vs. Silica diagram; melt inclusion data are from Arienzo et al. (2010); whole rock and matrix-glass compositions are from de Vita et al. (1999). b) Di-Hd-En-Fs classification diagram of clinopyroxenes found in A1, B1 and D1 members of the A-MS deposits; literature data refer to clinopyroxene from A-MS products (de Vita et al., 1999; Arienzo et al., 2010); mantle refers to the zones/sectors of the crystals between the core and the most external rim.

Fig. 3 a) Mg#, b) Na_2O and c) Al_2O_3 frequency histograms of core, mantle and rim of the zoned A-MS clinopyroxenes. These allow different populations to be identified. d) Al_2O_3 vs Mg# and e) TiO_2 vs Mg# variation diagrams of the analyzed zoned A-MS clinopyroxenes showing a wide compositional range and different populations and sub-populations. Note that all clinopyroxenes of different compositions lie on a trend defined by the orange arrow, with the exception of the ME1b and ME2b trends, which are shown in yellow. The significance of these trends is discussed in section 4.6.

Fig. 4 The colored table reports, for each sub-member, the frequency of occurrence of a compositional population in a zoning sector (core, mantle or rim) in a total of 36 (out of 41) analyzed clinopyroxene crystals of the A-MS deposit; c=core; m=mantle; r=rim. Percentages have been calculated considering clinopyroxenes with plateaus (36 out of 41). Percentage of compositional populations occurring in the homogeneous clinopyroxene crystals is also reported. % tot.in rows at the bottom express the abundance of a compositional population in all the analyzed crystals (36 for the zoned and 46 for the unzoned crystals, respectively).

Fig. 5 Types of zonation of the A-MS clinopyroxenes. Black diamonds are measured analysis along the crystal traverses showing concentration profiles from core to rim [Mg# = molar $Mg^{2+}/(Mg^{2+}+Fe_{tot})$]. In the BSE images, the blue lines are the traverses along which the chemical composition has been acquired. Black dashed lines indicate the initial profile shapes: these are different depending on the two methods applied for diffusion modeling and have been inferred through the relationships between Al_2O_3 (wt%) and Mg# in the profiles Red lines indicate modelled profiles. A complete description of the diffusion modeling methods is provided in section 4.6. The numbers in brackets indicate the percentage of zoned clinopyroxenes exhibiting such a pattern.

Fig. 6 Stratigraphic height vs Sr-isotopic composition of A-MS whole rocks and minerals. Literature data are from de Vita et al. (1999) and Arienzo et al. (2010).

Fig. 7 a) Fe-Mg partitioning between clinopyroxene and host rock ($^{Fe/Mg}Kd_{Cpx\text{-}liq}$ = 0.27±0.03; Grove and Bryan, 1983; Putirka et al., 2003); fields demarcated by colored dotted lines represent the whole set of A-MS clinopyroxenes, belonging to different magmatic environments, compared to host rocks; the transparent colored dotted lines refer to clinopyroxenes with high Mg# (ME0 and ME1) compared to A-MS whole rocks and matrix glass compositions: these clinopyroxenes are out of equilibrium with respect to their host rocks; some of these clinopyroxenes are in equilibrium with more mafic rocks; diamond symbols refers to some clinopyroxenes which passed the compositional test for equilibrium and have been used for geothermobarometry. b) Output pressures and temperatures estimates for the different magmatic environments of the A-MS clinopyroxenes obtained by the clinopyroxene-liquid thermometers (equation Talk2012) and barometers (equation Palk2012) specific for alkaline magmas (Masotta et al., 2013); error bars refer to SEE.

Fig. 8 Systems connectivity diagrams of the zoning patterns of A-MS clinopyroxene crystals. Since each compositional population can be associated to a specific magmatic environment (see section 3.2), the different magmatic environments are characterized by different ranges in the Mg#. Different zoning types are depicted by different connection lines represented by different color (e.g. the orange routes represent clinopyroxene crystals with core formed in ME2, mantle formed in ME0 and the rim formed in ME2). The height of the boxes is proportional to the frequency of occurrence of the magmatic environments. The A-MS clinopyroxene zoning patter is characterized by most of the connection lines linking ME0 and ME2, also passing through ME1, and a few connections linking ME2 and ME3.

Fig. 9 a,c) Mg# vs Al_2O_3 (wt%) relations of two selected crystal profiles. b,d) measured and inferred initial Mg# profiles. In Fig. 9a, the profile show a good correlation (R^2=0.94; black trend-line) between Mg# and Al_2O_3 (wt%). In Fig. 9b, the inferred initial profile is calculated based on the relations assessed by best fit of the linear trend-line of Fig. 8a. In Fig. 9c, the profile does not show a good correlation (R^2=0.74; black trend-line) between Mg# and Al_2O_3 (wt%). By taking into account the Mg# and Al_2O_3 (wt%) contents of the two plateaus (without the points in the boundary region between the plateaus), a new best fit (R^2=1; blue trend-line) has been estimated. In Fig. 9d, the inferred initial profile is calculated based on the best fit shown by the blue trend-line. Since Mg# And Al_2O_3 are correlated, the inferred profiles (blue diamonds in Fig. 9b,d) can be taken as growth profiles. Such an analysis implies that crystal profiles showing a good match between measured and inferred profiles (e.g. Fig. 9b) have been little, or not at all, affected by diffusion. On the other hand, crystal profiles showing differences between measured and inferred profiles (e.g. Fig. 9d) have been affected by diffusion.

Fig. 10 Output values of times obtained by diffusion modeling on 50 out of 82 analyzed profiles on clinopyroxene crystals. Method I yields the upper limits of residence times of crystals in a magmatic environment; method II yields the residence times of crystals in a magmatic environment.

Fig. 11 Schematic sketch illustrating the magmatic processes occurred in the A-MS plumbing system. a) three distinct magmatic environments at a t = 0: one (ME0), in red, in which core of clinopyroxenes with high Mg# (92–85) were formed, is associated with primitive magmas; an environment (ME2), in yellow, ascribable to a crustal reservoir of the Phlegraean magmatic system, in which core of clinopyroxenes with Mg#78–70 were formed and an environment (ME3), in blue, identifiable with a less abundant, most differentiated magma portion of the ME2 reservoir. b) The interaction between ME0 and ME2 explains the normal zoning for clinopyroxenes of ME0 and, conversely, the reverse zoning for clinopyroxenes of ME2, also leading to the formation of intermediate compositions (ME1). c) The interaction between ME2 and ME3 justifies the whole set of observed zoning patterns in the A-MS clinopyroxene; t_2-t_1 represents the time span of the mixing events recorded by crystals modeled through method II; t_1-t_0 represents the time span of the recharge events possibly due to increase of mafic magma input recorded by crystals modeled through method I; t_0= time of the eruption.

Fig. 1 in Supplementary Material 1 - Photomicrographs and BSE images of A-MS rocks showing the main textural and mineralogical features. a) microphotograph of a A-MS pumice from B1 sub-member showing a sanidine phenocryst; b) microphotograph showing a plagioclase and clinopyroxene aggregate in a pumice clast from the A1 sub-member; c) microphotograph showing phlogopite crystals in a pumice clast from the B2 sub-member; d) microphotograph showing clinopyroxene and opaque oxide crystals in a pumice clast from the A2 sub-member; e) microphotograph showing apatite crystals in the matrix-glass and in clinopyroxene of a pumice

clast from the D2 sub-member; f) BSE image of a pumiceous clast from D1 sub-member showing the network of vesicles. Abbreviations: cpx = clinopyroxene; pl = plagioclase; san =sanidine; phl = phlogopite; ap = apatite; ox = opaque oxide

Fig. 2 in Supplementary Material 1 Matrix-glass major and minor element variation diagrams of A-MS rocks; literature data on A-MS matrix-glasses and whole rocks composition are from de Vita et al. (1999).

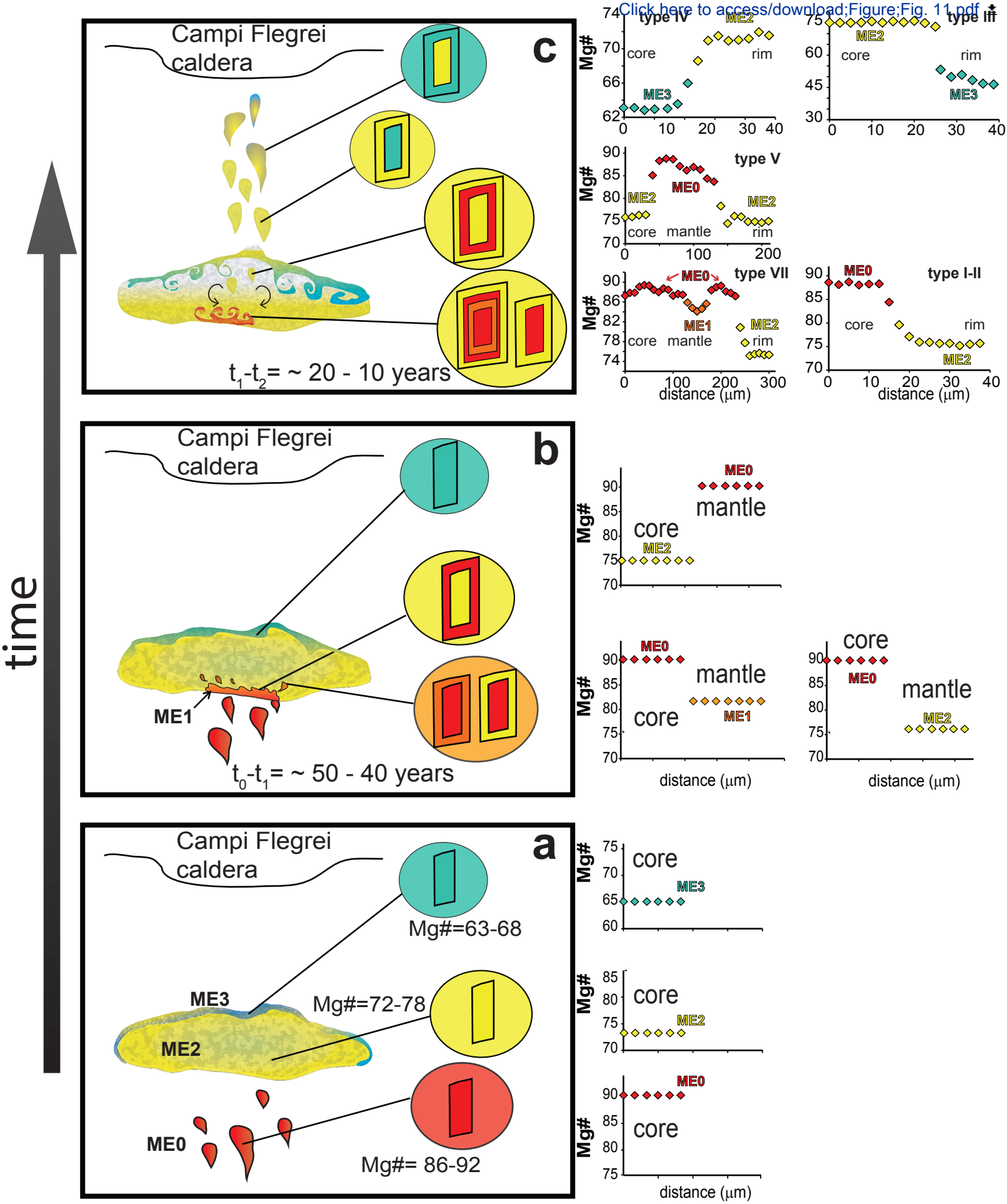

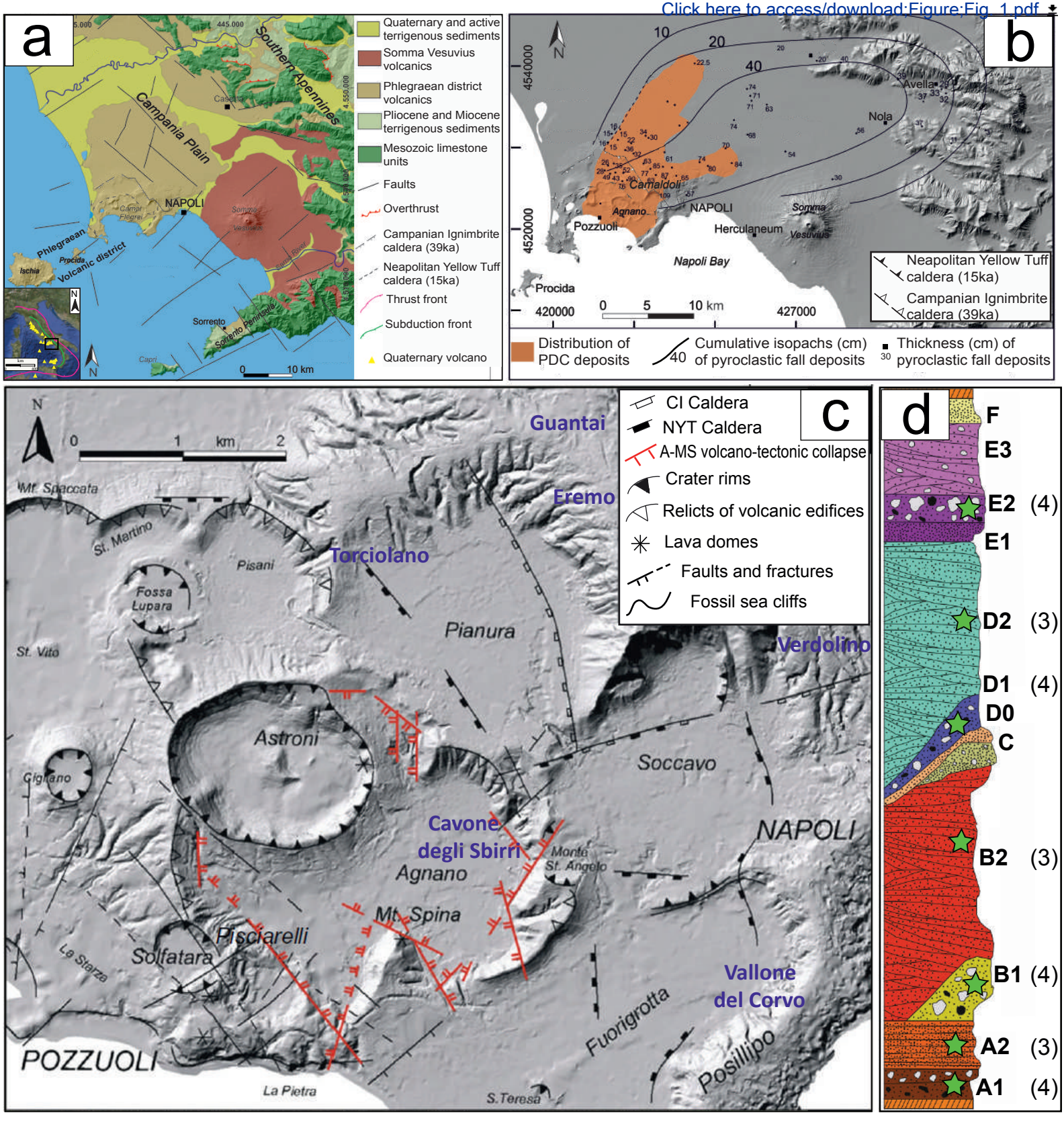

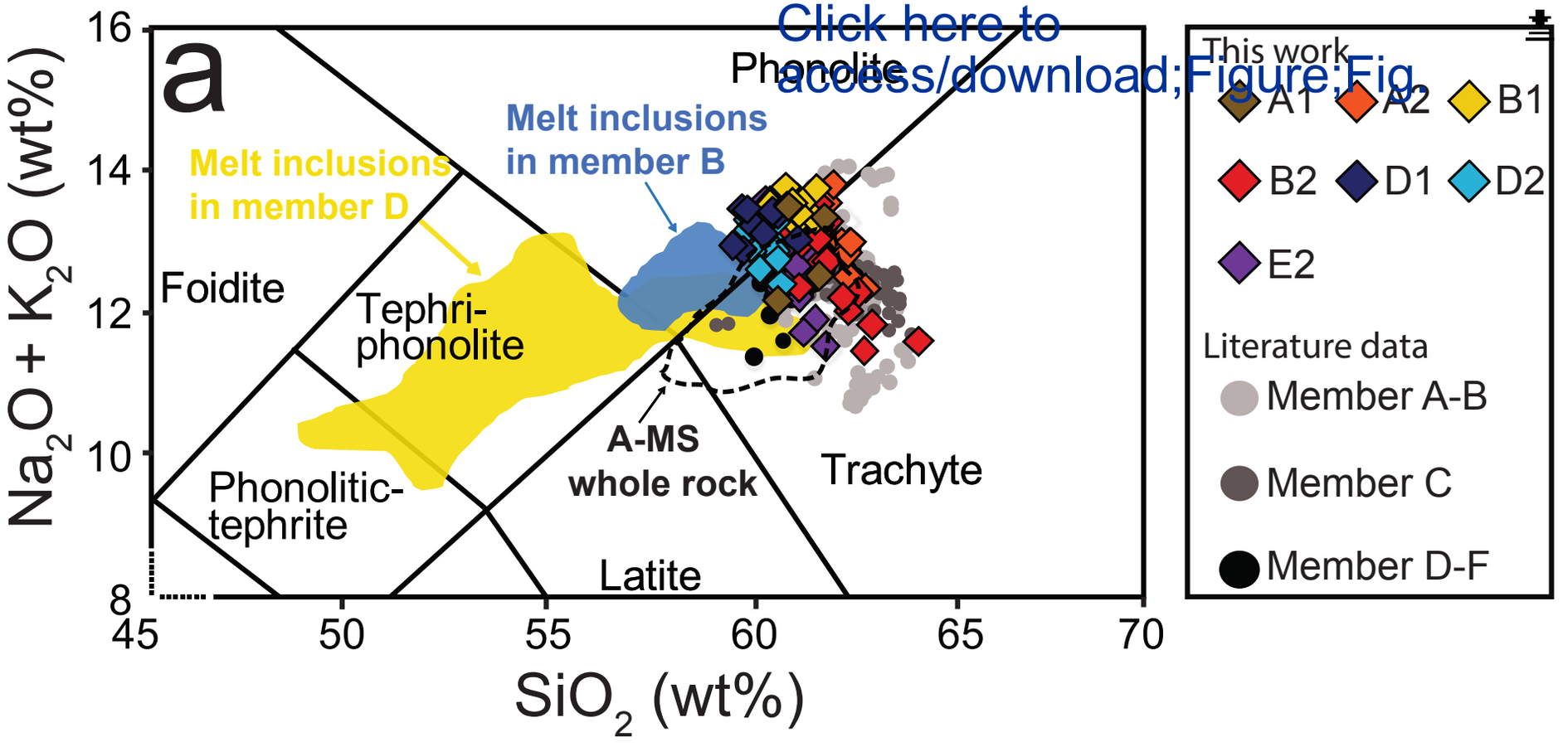

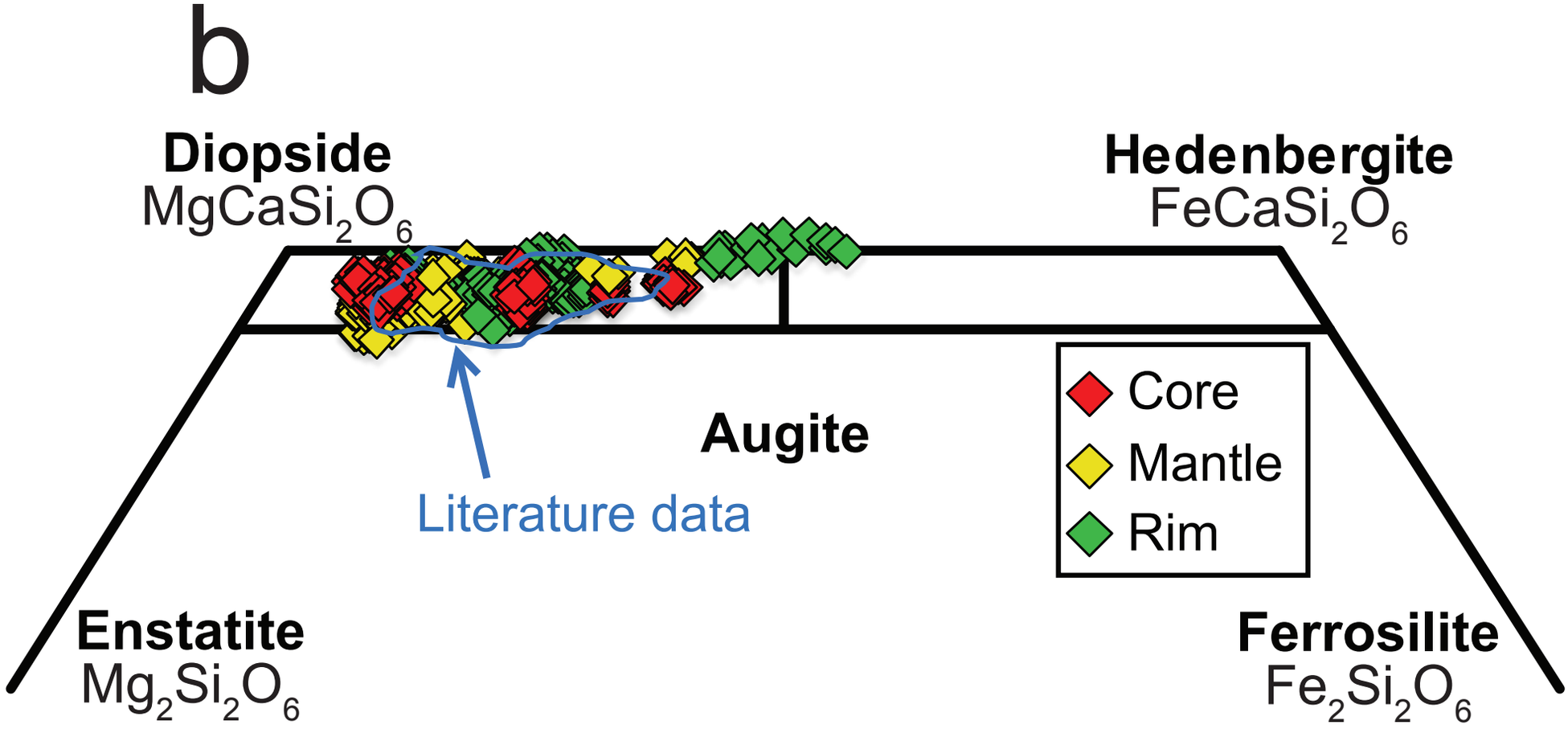

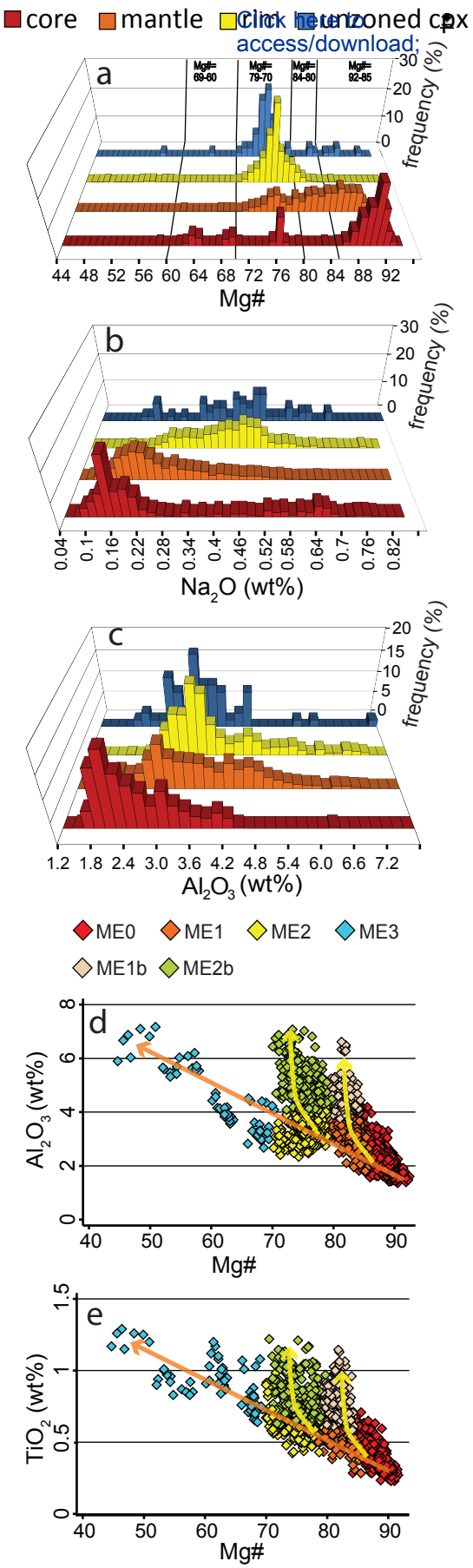

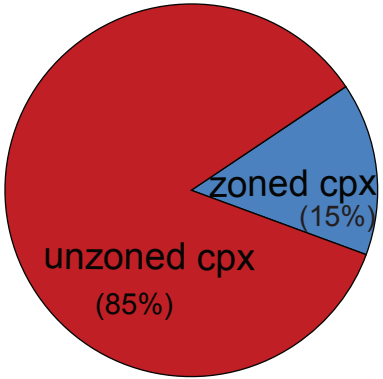

	Population Member	ME0 Mg#=92-85			ME1 Mg#=84-80			ME2 Mg#=78-70			ME3 Mg#= 69-60		ME3 Mg#= 55-45
		c	m	r	c	m	r	c	m	r	c	m	r
zoned crystals	D1	20%	12%		9%	17%		9%		39%			
zoned crystals	B1	11%	7%		2%			12%		27%	5%	2%	2%
zoned crystals	A1	14%	7%			7%				14%			
zoned crystals	% tot. in 36 analyzed crystals	70%			34%			100%			9%		
unzoned crystals	% tot. in 46 analyzed crystals	4%			4%			87%			4%		

profile traverse ◆ measured profile ------- initial profile ——— modelled profile

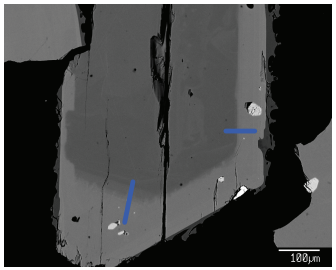

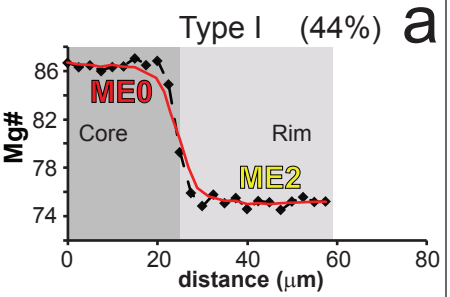

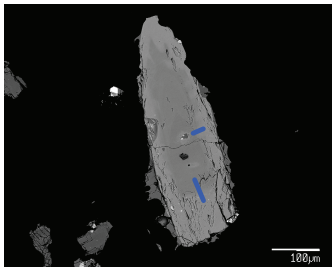

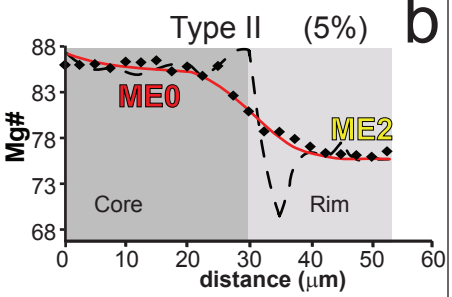

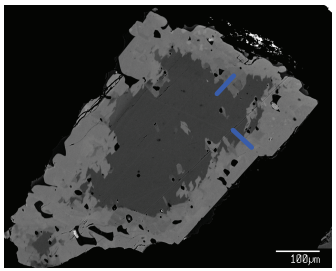

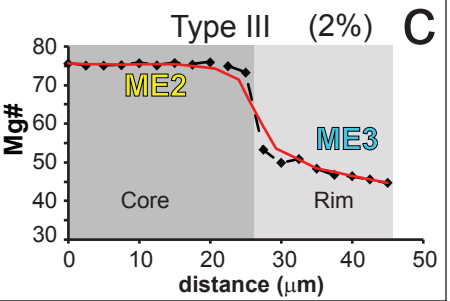

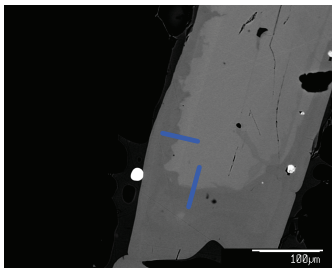

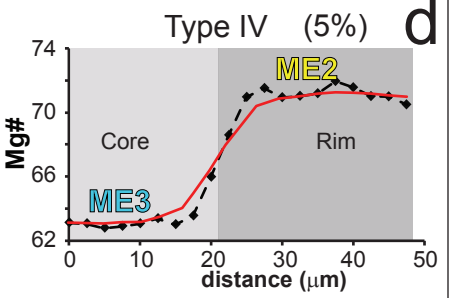

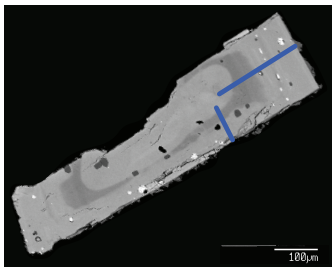

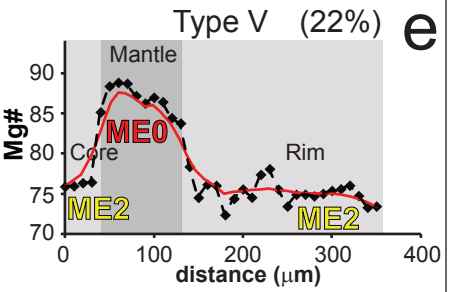

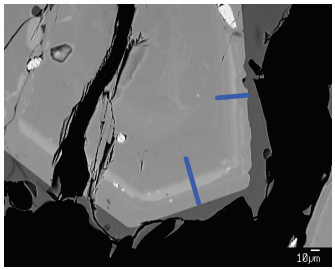

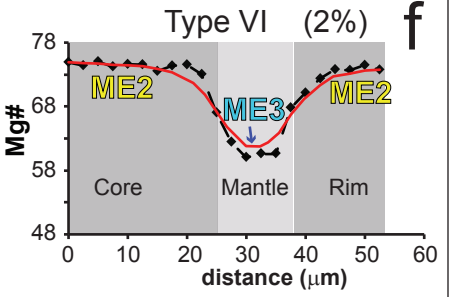

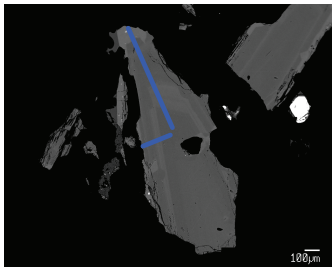

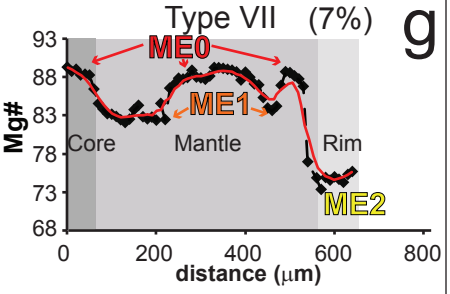

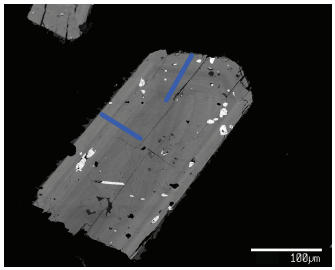

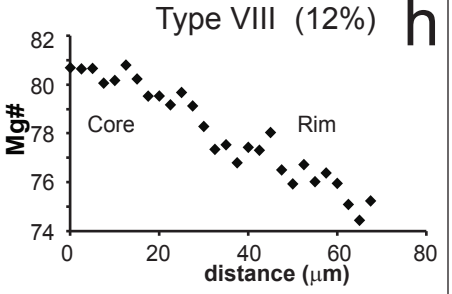

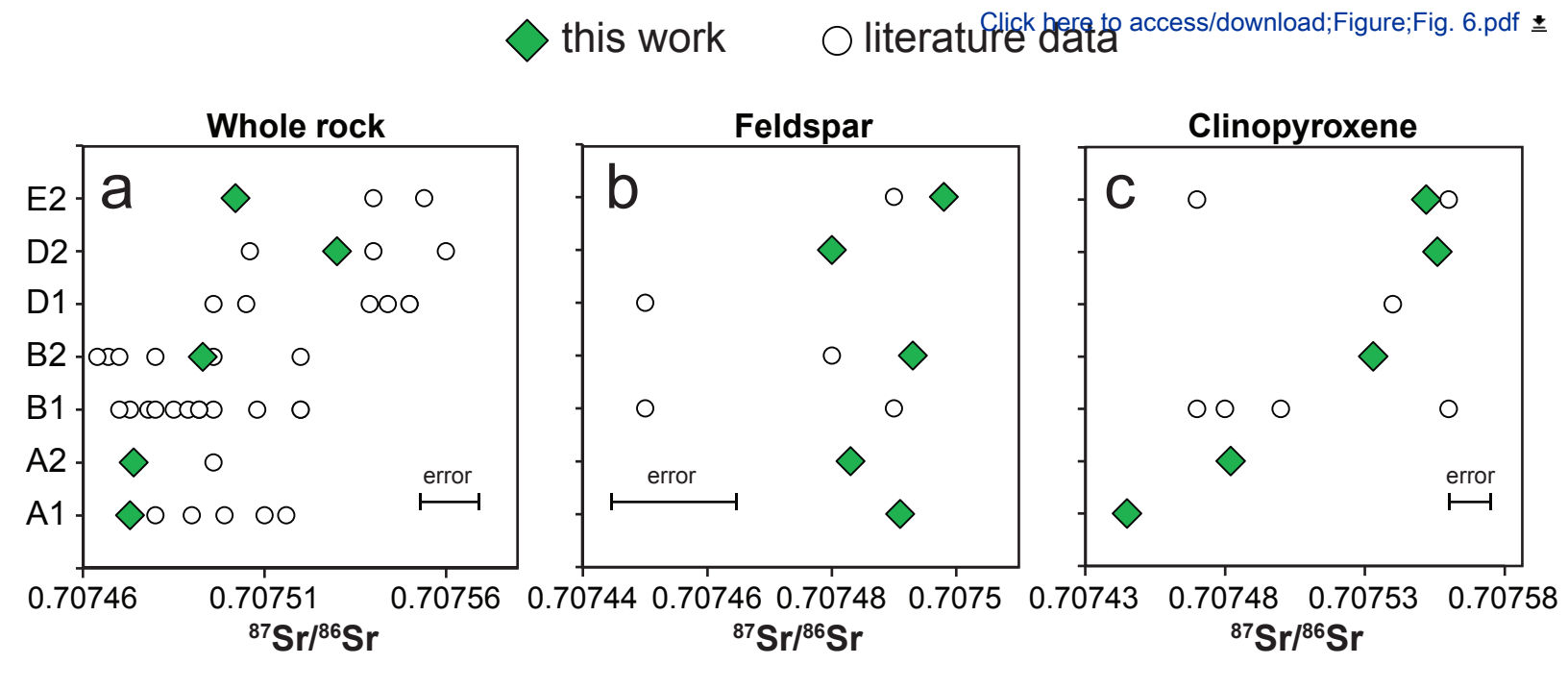

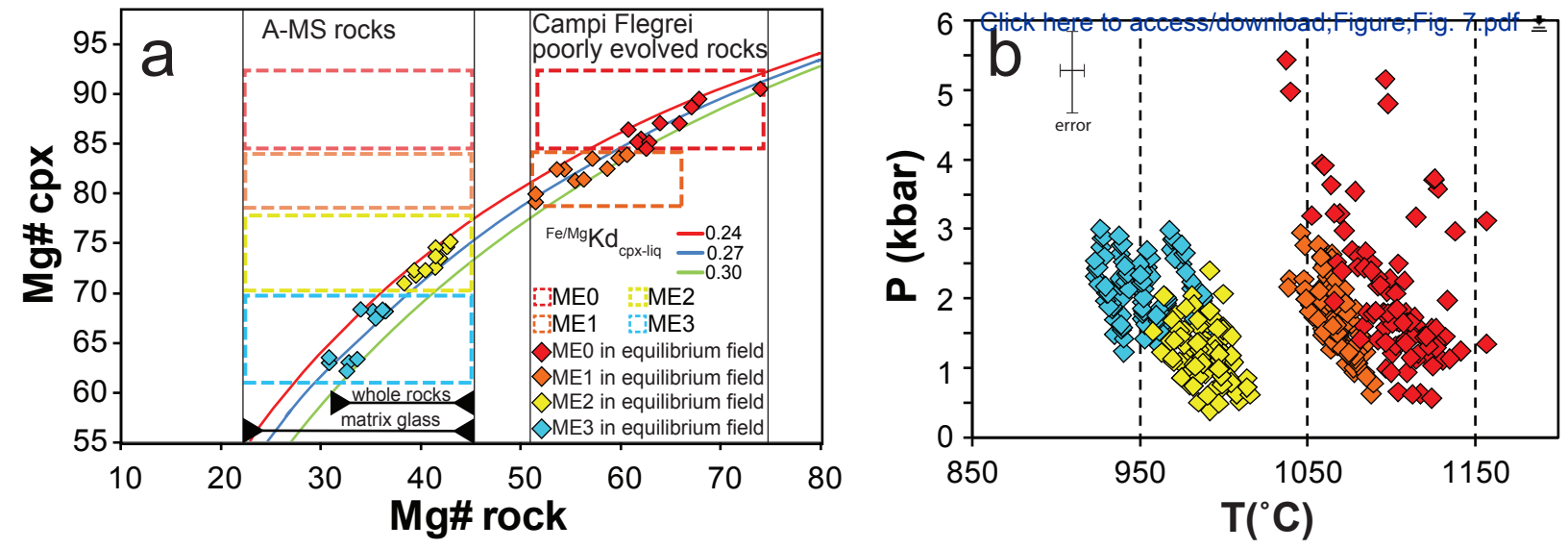

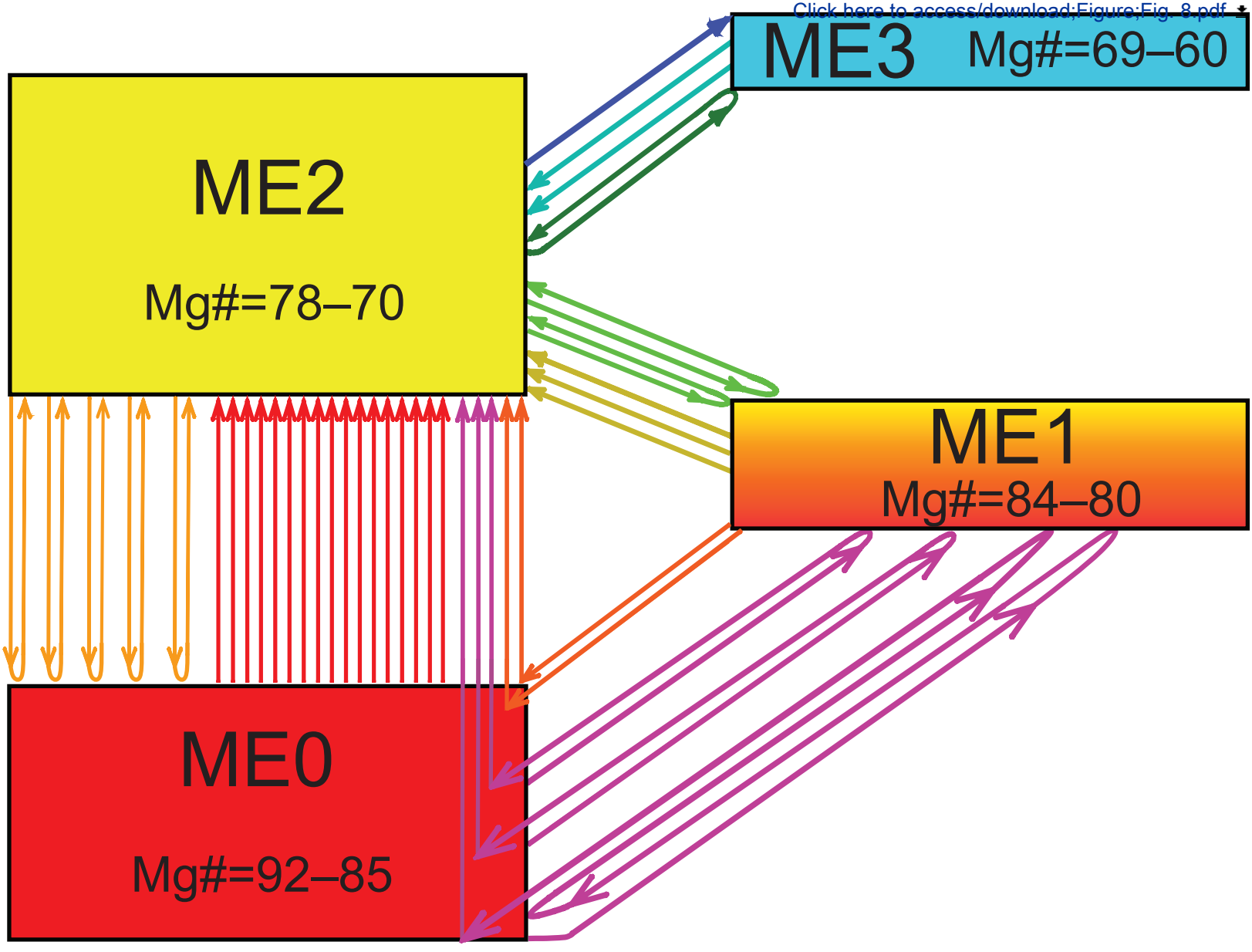

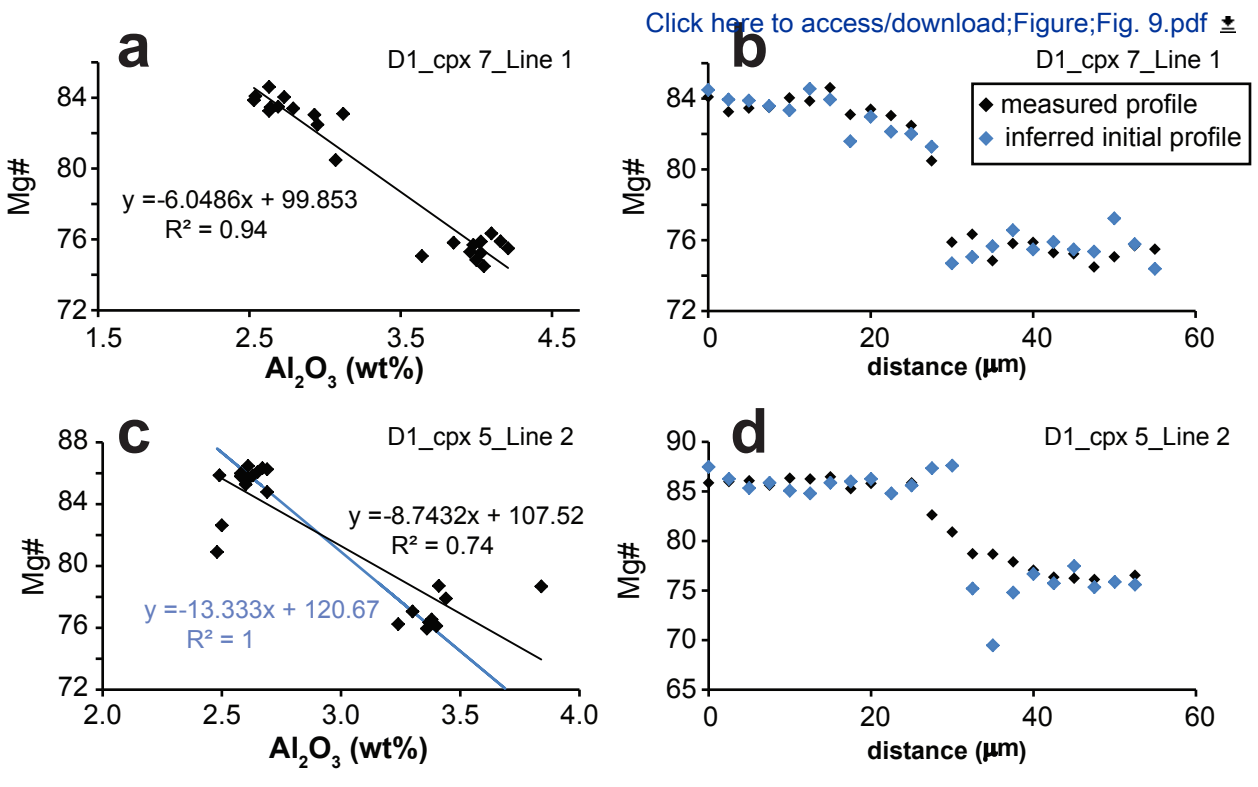

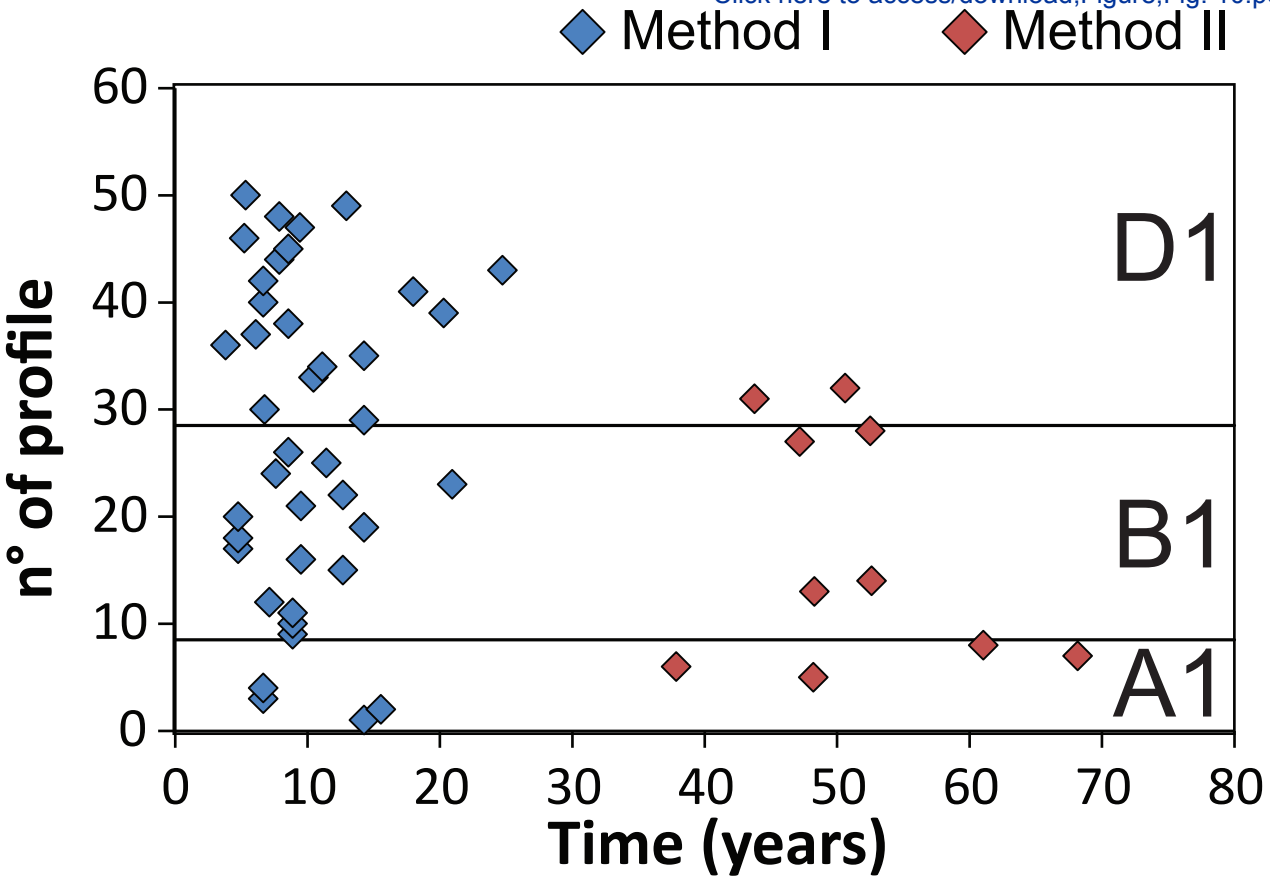

Research data

Click here to access/download

Supplementary Material

Research data.zip

Declaration of interests

☒ The authors declare that they have no known competing financial interests or personal relationships that could have appeared to influence the work reported in this paper.

☐The authors declare the following financial interests/personal relationships which may be considered as potential competing interests:
